Technische Universität Ilmenau
Institut für Physik
Experimentalphysik I / Oberflächenphysik

Intercalation of Graphene: Inelastic Excitations, Bilayer Growth, and Superstructures

Dissertation

zur Erlangung des akademischen Grades

Doctor rerum naturalium

der Mathematisch-Naturwissenschaftlichen Fakultät

der Technischen Universität Ilmenau

Verfasst von:
Johannes Halle
geboren am 26.10.1990
in Erlabrunn

Eingereicht am: 08.03.2019
Tag der wissenschaftlichen Aussprache: 16.04.2019

1. Gutachter: Prof. Dr. Jörg Kröger
2. Gutachter: Prof. Dr. Mads Brandbyge
3. Gutachter: Prof. Dr. Stefan Krischok

urn:nbn:de:gbv:ilm1-2019000115

Abstract

In this thesis graphene is intercalated with various metals to engineer its electronic and structural properties. Furthermore, intercalation is utilized in the development of a novel preparation method for bilayer graphene. Scanning tunneling microscopy and spectroscopy enables the characterization of inelastic excitations and intercalant superstructures at the nanoscale.

The first chapter of this work presents a comprehensive study of inelastic tunneling into graphene on metal surfaces. The intercalation of graphene on Ir(111) with Cs and Li gives rise to pronounced signatures of graphene phonon excitations in tunneling spectra, while Ni-intercalated graphene does not yield detectable inelastic features. Moreover, the phonon signal strength can be tuned by the alkali metal coverage and the junction conductance. Transport calculations based on an innovative three-terminal setup provide general insight into the relations between the graphene–electrode coupling and the observation of spectroscopic fingerprints of graphene phonons. Similar phonon signatures are obtained from monolayer and bilayer graphene on Ru(0001). Their signal intensity depends on the high-symmetry site of the moiré pattern, which may hint at a spatial variation of the electron-phonon coupling.

In the second part of this thesis the development of a growth method for graphene bilayers based on sequential chemical vapor deposition (CVD) is portrayed. On Pt(111) a first monolayer of graphene is prepared via the thermal decomposition of ethylene in a CVD process. Deposition of additional Pt then reactivates the sample surface for the growth of the second graphene sheet. Subsequent intercalation of the added Pt layer beneath the buried graphene produces bilayer graphene on Pt(111). The analysis of the observed moiré patterns evidences the successful double layer growth and unveils the impact of the twist angles at graphene–substrate and graphene–graphene interfaces on the origin of the observed moiré.

The thesis is concluded by an exploratory study of the impact of graphene on intercalant superstructures, which is mediated by its influence on the interlayer and intralayer interactions at the surface. The examples of Pt intercalation under graphene on Pt(111), and the intercalation of Cs and Li under graphene on Ru(0001) are investigated. On graphene-covered Pt(111) the inserted Pt produces a substrate reconstruction. Due to the presence of graphene, this superstructure is qualitatively different from those of a class of related reconstructions induced by the deposition of metals on Pt(111) and, specifically, by the homoepitaxy of Pt. Moreover, the successful cointercalation of graphene on Ru(0001) with Cs and Li is demonstrated. The alkali metals form separate phases with superlattices that are oriented at the graphene lattice rather than the Ru substrate.

Zusammenfassung

Die vorliegende Arbeit nutzt die Interkalation von Graphen mit verschiedenen Metallen zum einen zur Anpassung der elektronischen und strukturellen Eigenschaften von Graphen und zum anderen für die Entwicklung einer neuartigen Präparationsmethode für Graphen-Bilagen. Mithilfe eines Rastertunnelmikroskops (STM) werden außerdem inelastische Anregungen im Graphen sowie die durch Interkalation erzeugten Überstrukturen untersucht.

Der erste Teil der Dissertation stellt eine umfassende Studie zum inelastischen Tunneln in Graphen auf Metalloberflächen vor. Die Interkalation von Graphen auf Ir(111) mit Cs und Li bewirkt deutliche Signaturen von Phononenanregungen in den inelastischen Tunnelspektren. Im Gegensatz dazu erzeugt die Interkalation mit Ni keine erkennbaren inelastischen Anregungen beim Tunneln. Die Stärke der Phononensignale kann durch die Bedeckung der Alkalimetalle sowie durch die Veränderung des Spitze–Probe-Abstandes beeinflusst werden. Mithilfe von Transportrechnungen anhand eines innovativen Drei-Elektroden-Setups wird der Zusammenhang zwischen der Kopplung von Graphen zu den angrenzenden Elektroden und der Beobachtung der Graphen-Phononen in den Spektren analysiert. Weiterhin finden sich in Tunnelspektren von Graphen-Mono- und Bilagen auf Ru(0001) ähnliche Phononensignaturen. Deren Intensität hängt von der jeweiligen Hochsymmetrieregion der Moiréstruktur ab, was möglicherweise auf lokale Unterschiede in der Elektron-Phonon-Kopplung hinweist.

Im zweiten Teil der Arbeit wird die Entwicklung einer Präparationsmethode für Graphen-Bilagen auf Basis einer sequenziellen chemischen Gasphasenabscheidung (CVD) vorgestellt. In diesem Verfahren wird zunächst eine Monolage Graphen auf Pt(111) durch die thermische Aufspaltung von Ethen in einem CVD-Prozess erzeugt. Anschließend wird zusätzliches Pt auf die mit Graphen bedeckte Probenoberfläche aufgedampft. Hierdurch wird diese für einen weiteren CVD-Schritt reaktiviert, in welchem die zweite Lage Graphen gewachsen wird. Die nachfolgende Interkalation der abgeschiedenen Pt-Schicht unter die vergrabene Graphenlage erzeugt schließlich die Graphen-Bilagen auf Pt(111). Eine Analyse der nun beobachteten Moirémuster bestätigt die erfolgreiche Präparation von Graphen-Doppellagen und deckt den Einfluss der Graphen–Substrat- und Graphen–Graphen-Verdrehwinkel auf das Erscheinungsbild der beobachtbaren Moiréstrukturen auf.

Den Abschluss dieser Dissertation bildet eine explorative Studie der Wirkung von Graphen auf die Überstrukturen von Interkalanten. Diese Wirkung wird durch den Einfluss der Graphen-Deckschicht auf das Zusammenspiel von Wechselwirkungen zwischen und innerhalb der oberflächennahen Atomlagen vermittelt. Exemplarisch werden zum einen die Pt-Interkalation von Graphen auf Pt(111) und zum anderen die Interkalation von Cs und Li unter Graphen auf Ru(0001) untersucht. Bei graphenbedecktem Pt(111) ruft das eingefügte Pt eine Rekonstruktion der Substratoberfläche hervor. Aufgrund des Einflusses von Graphen unterscheidet sich deren Struktur qualtitativ von denen einer Klasse verwandter Rekonstruktionen, die durch das Aufbringen von Metallen auf Pt(111) und insbesondere durch die Homoepitaxie von

Pt hervorgerufen werden. Darüber hinaus wird die erfolgreiche Kointerkalation von Graphen auf Ru(0001) mit Cs und Li präsentiert. Die Alkalimetalle bilden separate Phasen mit Übergittern, die sich jeweils am Graphengitter statt an dem des Ru-Substrates ausrichten.

Contents

List of Abbreviations

arb. u.	arbitrary units
BLG	bilayer graphene
BZ	Brillouin zone
CVD	chemical vapor deposition
DFT	density functional theory
DOS	density of states
EBE	electron beam evaporator
EELS	electron energy loss spectroscopy
GGI	graphene–graphene interface
GSI	graphene–substrate interface
hBN	hexagonal boron nitride
IET	inelastic electron tunneling
IETS	inelastic electron tunneling spectroscopy
LDOS	local density of states
ML	monolayer(s)
MLG	monolayer graphene
NEGF	nonequilibrum Green function
PBC	periodic boundary conditions
STM	scanning tunneling microscope
STS	scanning tunneling spectroscopy
TA	transversal acoustic phonon mode
TLG	trilayer graphene
TPG	temperature programmed growth
ZA	acoustic out-of-plane phonon mode
ZO	optical out-of-plane phonon mode

1 Introduction

The “miracle material” graphene – a single sheet of carbon in honeycomb structure – earned its name due to its phenomenal properties that are superior to those of conventional materials in various fields.[1, 2] Exceptionally high electron mobility, thermal conductivity, and mechanical strength are only some of the features that are combined by graphene and have sparked hopes and dreams of a beginning “graphene age”. Its unique band structure is characterized by linearly dispersing π/π -bands in the proximity of the Fermi energy, which entail exciting physical phenomena like the relativistic behavior of charge carriers or the anomalous quantum Hall effect, [3, 4] making it an interesting platform for fundamental research as well.

Since most of the supreme properties of graphene have been demonstrated only under laboratory conditions so far, [1, 5] the eventual application in devices requires suitable methods for the production of extended graphene sheets of high structural quality. One of the most promising approaches in this regard is the epitaxial growth of graphene.[2, 6, 7] However, the various available substrate all have their pros and cons. For example, the hybridization between graphene and transition metal substrates ranges from very weak in the case of Pt(111) to very strong in the case of Ni(111) or Ru(0001).[6, 8] While weakly coupled graphene on Pt(111) preserves many of its ideal characteristics, often multiple rotational domains occur.[6, 9] On Ru(0001) on the other hand, graphene is strongly bound, exhibits a highly corrugated moiré pattern, and its band structure is altered significantly.[6, 10, 11] However, graphene grown on Ru(0001) offers the benefit of being rotationally well-aligned, yielding virtually only one orientation.[6] The desire to combine advantages of different substrates or to add other materials in order to tune the properties of epitaxial graphene calls for adequate preparation techniques.

A powerful method to modify the graphene–substrate interaction as well as the properties of graphene itself is the insertion of materials at the graphene–substrate interface. This so-called intercalation has long been known from the fabrication of graphite intercalated compounds.[12] Its application to graphene is typically performed by the deposition of the intercalant on top of the graphene sheet followed by an annealing step that activates the diffusion of the added material through specific entry points to the interface.[13–15] Examples of important achievements enabled by intercalation are the formation of local p-n junctions [16] and the opening of a band gap in graphene, [17, 18] which is a prerequisite for any future application in transistors. Furthermore, depending on substrate and intercalant, the graphene–substrate interaction has reportedly been weakened or strengthened.[19–21] Throughout this work, intercalation is applied for different purposes, once again proving its versatility.

The observation of giant phonon signatures in scanning tunneling spectroscopy on epitaxial graphene on SiC [22] has triggered numerous investigations over the past decade to explore phonon-mediated tunneling into graphene. In comparison to vibrational signatures of molecules, the differential conductance increase due to these phonons was up to three orders of magnitude larger.[23–25] While graphene on semiconducting or insulating substrates like SiC, [22] SiO_2, [24, 26] and hBN on SiO_2 [27, 28] has been demonstrated to exhibit similarly large phonon signals, studies of graphene-covered metal substrates are still scarce. Only recently have two reports presented phonon signatures from graphene on Pt(111) [29] and Ir(111).[25] In both these cases, the inelastic excitations have been observed only on delaminated graphene structures but vanished on the flat graphene sheet. The apparent impact of the graphene–substrate hybridization on the phonon signatures has been mentioned in some studies, [25, 29, 30] but a comprehensive understanding of the interplay of the coupling between substrate, graphene, and tip of the scanning tunneling microscope (STM) has not been achieved yet. The first part of this thesis explores that issue by means of inelastic electron tunneling spectroscopy (IETS) with the STM.

Furthermore, the currently immense attention towards multilayered homostructures or heterostructures of two-dimensional materials [2, 31] has motivated the extension of this investigation to bilayer graphene (BLG) on Ru(0001). In comparison to its electronic structure, the vibrational properties of BLG have been hardly explored so far. Only few theoretical [32, 33] and experimental works, mostly using Raman spectroscopy [34–37] have been conducted. In particular spatially resolved probes of BLG phonon excitations are rare. One previous IETS study of BLG on Ru(0001) has reported a spatial variation of the phonon signal intensity at different high-symmetry regions of the moiré pattern, [38] and inelastic atom scattering at BLG on Ru(0001) has revealed a localized vibrational mode in so-called graphene nanodomes.[39] On Ir(111) phonon excitations have been observed in IETS only from bilayer but not from monolayer graphene domains.[40]

The first set of experiments presented in this thesis are, therefore, devoted to the following open questions:

> What role do the graphene–substrate and the graphene–tip coupling play in inelastic tunneling into graphene?
>
> How do the phonon signatures depend on the probing position in the BLG/Ru(0001) moiré pattern?
>
> Is there a general description that explains the observation of phonon signals in IETS from both, quasi-freestanding and strongly hybridized graphene?

To this end, graphene samples on Ir(111) and Ru(0001) substrates are prepared. The intercalation of graphene on Ir(111) with Cs, Li, and Ni produces different all-metal systems with varying graphene–substrate interaction. Additionally, the intercalant coverage represents a further experimental control parameter. The impact of the graphene–tip coupling is investigated in contact experiments. Monolayer graphene on Ru(0001) provides a platform to explore potential phonon excitations in the strong hybridization limit. Local probes with the STM tip shed light on the impact of (i) the spatial variation of the graphene-substrate coupling in monolayer graphene and (ii) the graphene–graphene coupling in bilayer graphene on the phonon signal intensity. State-of-the-art transport calculations accompany the experiments for additional insight into the phonon-mediated tunneling processes.

The second chapter of the thesis describes the development of a growth method for BLG on Pt(111). As mentioned above, scalable preparation methods for graphene are necessary to enable its application in industry and devices. The established chemical vapor deposition (CVD) of hydrocarbons on transition metals [41] has great potential in this regard as it is simple, reliable, and inexpensive. Due to its self-limiting nature, it provides precise thickness control to one monolayer of graphene but lacks the option of multilayer growth. The open questions addressed in the second half of this work are, therefore:

> Is it possible to utilize CVD for the preparation of bilayer graphene?
>
> How can the self-limitation in the CVD growth process be circumvented?

The basic idea to tackle this challenge is the reactivation of the graphene-covered sample surface for a second CVD cycle by the deposition of additional substrate material. After the second layer growth, the added metal should intercalate below the bottom graphene sheet upon annealing and, thus, produce bilayer graphene. The selected candidate substrates are the (111) surfaces of Ir and Pt, which both interact only weakly with graphene.[6, 8]

The third part of this work presents the investigation of intercalation-induced superstructures that are affected by the presence of graphene. Ordered arrangements of adsorbates, moiré patterns of layered systems, and substrate reconstructions are only few prominent examples of the ubiquitous superstructures at surfaces. Their appearance is determined by the subtle interplay of adsorbate–adsorbate and adsorbate–substrate interactions or, analogously, intralayer and interlayer interactions.[42, 43] As intercalants experience not only the interaction with the substrate and each other but also with the graphene cover layer, existing superstructures may be altered and new ones stabilized. STM characterization allows the direct observation of such patterns and has been successfully applied in various intercalated systems.[44] In this chapter, two specific metal-intercalated graphene samples are investigated: (i) Pt under graphene on Pt(111) and (ii) Cs and Li under graphene on Ru(0001). Additionally, the cointercalation of graphene on Ru(0001) with Cs and Li is attempted. The main questions addressed here are:

> What is the structure of the intercalant materials in the respective graphene/metal samples?
>
> How does the presence of graphene affect the formation of these superstructures?

The outline of the thesis is summarized below:

Chapter 2 briefly describes relevant experimental techniques, samples, and the analysis of the obtained data.

Chapter 3 presents the IETS investigations of (i) graphene on Ir(111) intercalated with Cs, Li, Ni along with the results of the transport calculations, and (ii) monolayer and bilayer graphene on Ru(0001).

Chapter 4 elaborates on the successful development of a preparation method for bilayer graphene on Pt(111) and the analysis of the resulting moiré patterns.

Chapter 5 presents the STM characterization of intercalation-induced superstructures of Pt under graphene on Pt(111), and Cs and Li under graphene on Ru(0001).

2 Experiment and Methods

In the experiments presented in this thesis, a low-temperature scanning tunneling microscope (STM) was employed to investigate pristine and intercalated graphene on different metal substrates. The STM is a powerful tool for the characterization of structural, dynamical and electronic properties of surfaces. Its high spatial resolution based on the quantum-mechanical tunneling effect enables precise examinations at the atomic scale.

This chapter provides fundamental theoretical and practical background of the STM as well as related information on spectroscopic techniques, the experimental setup, and prepared samples. It is concluded by a section about modeling and analysis of the ubiquitous moiré patterns generated by graphene overlayers. All descriptions are focused on the topics of this thesis.

2.1 Scanning Tunneling Microscopy

2.1.1 Working Principle

The basic setup of a STM is illustrated in Fig. 2.1. It consists of two electrodes – an atomically sharp metal tip and an electrically conducting sample – separated by a potential barrier. When a bias voltage (V) is applied across this junction, electrons tunnel from one electrode to another generating an electric current (I) that is typically in the pA to μA range. Topographic mapping is performed either in constant current or in constant height mode. When operating in constant current mode, the feedback loop constantly adjusts the tunneling current to a set value. By moving the STM tip laterally across the sample while recording the vertical tip displacement a topographic representation $z(x, y)$ of the surface is obtained. Alternatively, in constant height mode variations of the current $I(x, y)$ are recorded while scanning the surface at constant tip-sample separation.

The tunneling current can be expressed as

$$I = \frac{4\pi e}{\hbar} \int_{-\infty}^{\infty} \rho_s(\varepsilon)\rho_t(\varepsilon - eV)|M_{ts}|^2 \left[f(\varepsilon - eV) - f(\varepsilon)\right] d\varepsilon \tag{2.1}$$

in the Transfer Hamiltonian approach.[45, 46] Here, e is the elementary charge, $\hbar$ the reduced Planck constant, ρ_s and ρ_t the local density of states (LDOS) of sample and tip, respectively, M_{ts} the tunneling matrix element, [45] and $f(\varepsilon)$ the Fermi distribution, which includes the influence of the temperature on the tunneling process. $|M_{ts}|^2$ describes the tunneling probability and may be approximated as transmission coefficient T with

$$|M_{ts}|^2 \approx T(\varepsilon, V, z) = \exp\left[-2z\sqrt{\frac{2m}{\hbar^2}\left(\frac{\Phi_t + \Phi_s}{2} + \frac{eV}{2} - \varepsilon\right)}\right] \tag{2.2}$$

in the Wentzel-Kramers-Brillouin approximation [47, 48] for a simple trapezoidal tunneling barrier [Fig. 2.1(b)]. Here, z is the tip-sample distance, m the free electron mass, Φ_t and Φ_s the work functions of tip and sample, respectively. The exponential

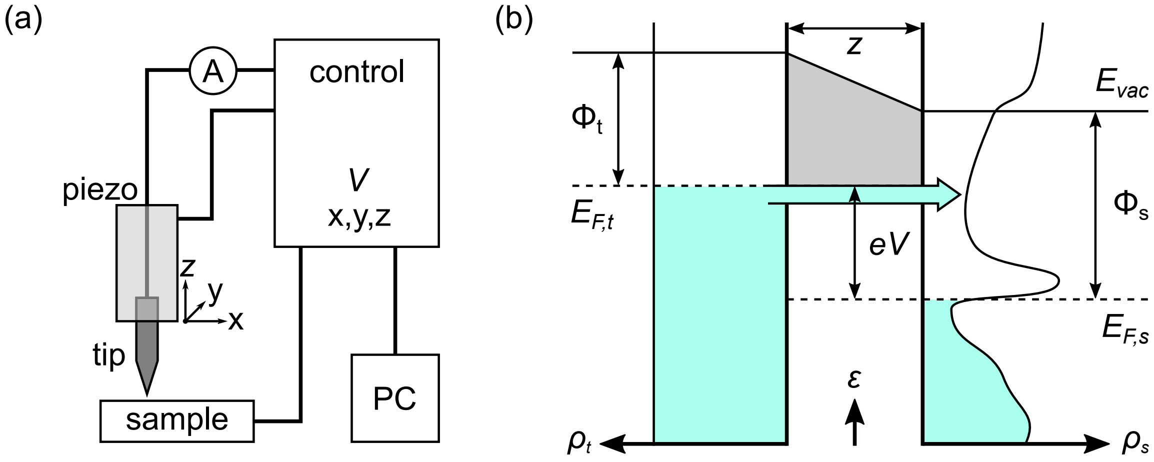

Figure 2.1: (a) Schematic diagram of the STM. A sharp metal tip is brought near the conducting sample. The control unit applies a bias voltage V to the junction and moves the tip via piezo actuators. The tunneling current is measured by a transimpedance amplifier and input into the control unit. A feedback loop enables scanning with constant current by adjusting the tip-sample distance. (b) Sketch of the elastic tunneling through a trapezoid vacuum barrier of width z. The barrier height is defined by the work functions (Φ_t and Φ_s) and the Fermi energies ($E_{F,t}$ and $E_{F,s}$) of tip (t) and sample (s). E_{vac} denotes the vacuum energy. The Fermi energies are shifted by eV due to the applied bias, which leads to a net current of electrons tunneling from occupied tip states into unoccupied sample states or vice versa, depending on the polarity. The local densities of states (ρ_t and ρ_s) of tip and sample influence the tunneling current.

dependence of the transmission factor on z is responsible for the high sensitivity of the tunneling current to smallest distance variations, which enables a precise measurement of the atomic topography with the STM. It should be noted, however, that the local densities of states of tip and sample as well as the applied bias affect the tunneling current (Eq. 2.1).

Scanning tunneling spectroscopy (STS) takes advantage of that and accesses electronic properties of the sample by performing tunneling bias sweeps. For small bias ($eV \quad \Phi_t, \Phi_s$), the energy-dependence of T (Eq. 2.2) can be neglected. Furthermore, at very low temperatures the Fermi distribution becomes a step function. With these considerations and under the additional assumptions of a constant DOS of the tip, ρ_t, around the Fermi level and a constant tip–sample separation, z_0, the differential conductance can be approximated as

$$\frac{\mathrm{d}I}{\mathrm{d}V} \quad \rho_t(0)\rho_s(eV)\exp\left[-2z_0\sqrt{\frac{2m}{\hbar^2}\left(\frac{\Phi_t+\Phi_s}{2}\right)}\right]. \tag{2.3}$$

Thus, the $\mathrm{d}I/\mathrm{d}V$ signal recorded in bias sweeps at constant height is proportional to the LDOS of the sample at eV.

In the experiment, tips are often made of or terminated with noble metals and calibrated at well-known electronic features like surface resonances to ensure the absence of tip LDOS features in the spectra. In constant height spectroscopy the feedback loop is deactivated during the voltage sweep to keep the tip–sample distance at z_0. The $\mathrm{d}I/\mathrm{d}V$ is typically obtained using a lock-in amplifier. It adds a periodic modulation to the applied tunneling bias. The current response of the junction is then multiplied with a reference signal at the first or a higher harmonic of the modulation frequency. The DC component of the resulting signal is extracted and output. It is proportional to the $\mathrm{d}I/\mathrm{d}V$ at the first harmonic, or proportional to the $\mathrm{d}^2I/\mathrm{d}V^2$ at the second harmonic. The latter plays an important role for inelastic electron tunneling spectroscopy (IETS), a technique described in the next section.

2.1.2 Inelastic Electron Tunneling Spectroscopy (IETS)

In the elastic tunneling process illustrated in Fig. 2.1(b) electrons tunnel only at constant energy. However, there is a second pathway available, where electrons may excite, e.g., phonons, molecular vibrations, spin flips, and plasmons with the energy $\hbar\omega$. This process may happen for both polarities of the bias. Figure 2.2(a) illustrates such an inelastic electron tunneling (IET) process. For $|eV| \quad \hbar\omega$ the energy of the tunneling electron is sufficient to perform the corresponding inelastic excitation, which has two effects on the tunneling current.[49–51] On the one hand, the emission of an excitation quantum opens an additional tunneling pathway and is accompanied by an increase in the conductance [blue arrows in Fig. 2.2(a)]. On the other hand, re-absorption of the excitation quantum leads tunneling electrons to final states at the initial energy [orange arrows in Fig. 2.2(a)]. Therefore, this process interferes with the purely elastic tunneling process. It has been shown that this interference causes a decrease in the differential conductance and alterations of the spectroscopic line shape.[49, 50, 52] The overall appearance of inelastic excitations in IETS thus depends on the contributions of both these processes. However, the spectra presented in this thesis (chapter 3) all indicate a clearly dominating contribution of the first effect. The increase in the conductance can be recognized by step-like features in the $\mathrm{d}I/\mathrm{d}V$ or as point-symmetric dip–peak pair at $V = \hbar\omega/e$ in $\mathrm{d}^2I/\mathrm{d}V^2$ spectra [Fig. 2.2(b)].

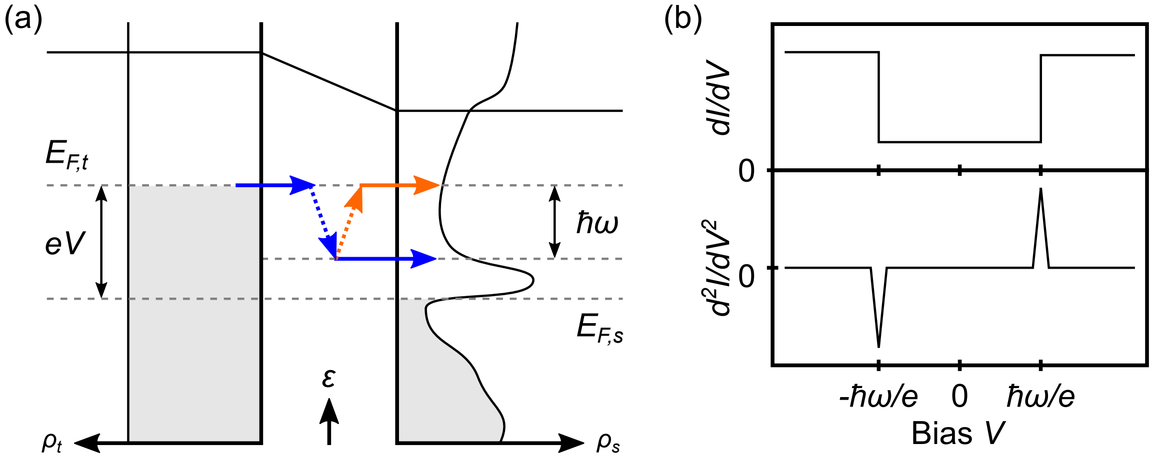

Figure 2.2: (a) Sketch of the inelastic electron tunneling process. At sufficiently high bias voltage the tunneling electron may excite, e.g., a phonon (energy $\hbar\omega$) and enter finite states at lower energy (blue pathway). Alternatively, the energy quantum may be reabsorbed (orange pathway) and interfere with the elastic tunneling channel. (b) Exemplary schematic diagrams of $\mathrm{d}I/\mathrm{d}V$ and $\mathrm{d}^2I/\mathrm{d}V^2$ spectra in the presence of inelastic tunneling. The additional tunneling channel for $|V|$ $\hbar\omega/e$ increases the differential conductance (upper panel) and causes symmetric step-like features. Accordingly, the IET spectra (lower panel) exhibits a point-symmetric dip–peak pair at the threshold bias.

Predictions of the intensity and line shape of vibrational signatures in IET spectra are not straightforward and usually require advanced computational methods.[53, 54] Although some propensity rules based on vibrational and electronic characteristics of specific molecular junctions have been found, [50, 55, 56] there are no general rigorous selection rules in IETS.[57] Therefore, IETS is a great alternative to optical vibrational spectroscopy techniques such as infrared or Raman spectroscopy. Due to its high spatial resolution, it is especially well-suited for the chemical identification of molecules at ultra-low concentrations.[58] Other cutting-edge investigations address, e.g., chemical bonding, heat generation and dissipation at the molecular scale, charging phenomena in molecules, and current-induced reactions.[54, 57]

2.2 Experimental Setup and Preparation

2.2.1 Setup

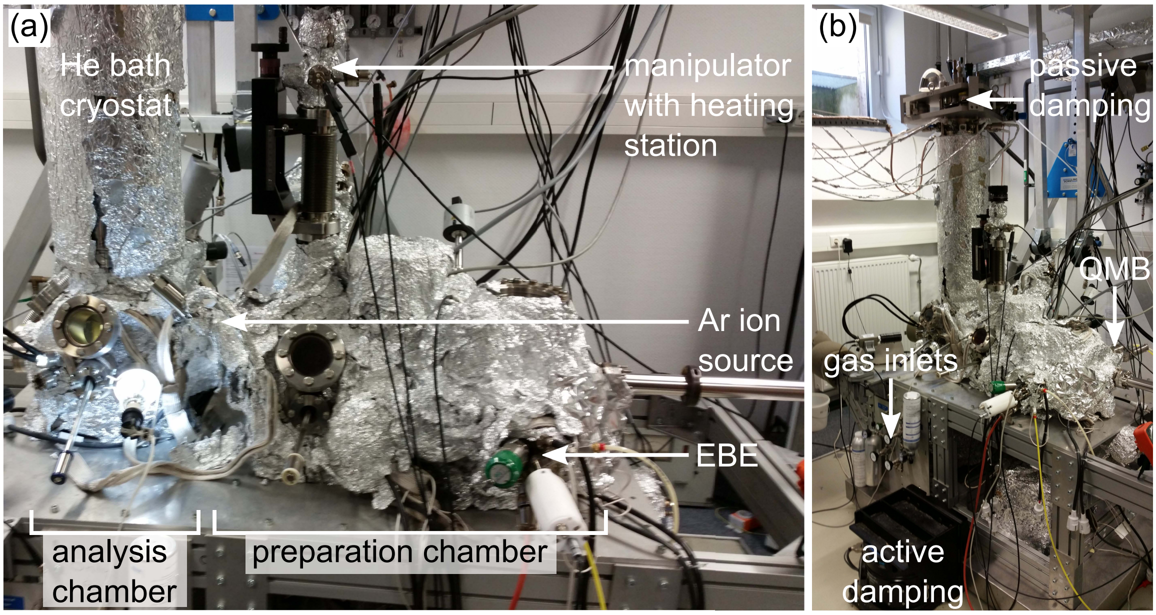

Figure 2.3: Photographies of the experimental setup with labeled parts and devices. (a) Front view showing the two main chambers. EBE: electron beam evaporator (b) Side view. QMB: quartz microbalance

All presented experiments have been carried out with a home-built low-temperature STM operated under ultra-high vacuum (pressure $\lesssim 10^{-8}$ Pa) at 5 K. The experimental setup is shown in Fig. 2.3. It consists of two vacuum chambers – the analysis chamber with the STM and a He bath cryostat, and the preparation chamber with an Ar ion source, a heating station, gas inlets, electron beam evaporators (EBE), a quartz microbalance (QMB), and alkali metal evaporators equipped with commercial dispensers for Cs and Li. A load lock chamber (located at the back of the setup) with a separate turbomolecular pump allows the transfer of samples and smaller devices into the preparation chamber without venting. The whole system is supported by an active damping system and built on a separate foundation isolated from the rest of the building. Additional passive air dampers decouple the inner cryostat with the attached STM from the chambers. The turbomolecular pumps are turned off during the measurements, while the pressure is sustained by ion pumps.

The STM body is described elsewhere in detail.[59] All STM images were recorded in the constant-current mode with the bias voltage applied to the sample. Tips were either fabricated by electrochemical etching of W wire or by cutting Au wire. The tips were cleaned in-situ by annealing and field-emission, and subsequently trained by controlled contact with a Au(100) surface until stable imaging with high resolution was achieved.

2.2.2 Sample Preparation

	Ar^+ ion energy	annealing & O_2 exposure	graphene CVD by C_2H_4 exposure	intercalation & post-annealing
Ir(111)	1.5 kV	1600 K O_2: 1300 K, 10^{-5} Pa	1500 K, 10^{-4} Pa	Cs (660 K) Li (570 K) Ni (660 K)
Ru(0001)	1.5 kV	O_2: 1300 K, 10^{-5} Pa	1600 K, 10^{-4} Pa	Cs (660 K) Li (570 K)
Pt(111)	1.2 kV	1200 K O_2: 1200 K, 10^{-5} Pa	1200 K, 5 10^{-4} Pa	Pt (1200 K)

Table 2.1: Preparation parameters. Given pressures are total pressures during the respective gas exposure. Post-annealing temperatures are denoted in brackets next to the intercalant.

The preparation of the investigated graphene samples comprised three main steps, namely the preparation of a clean metal surface, the growth of graphene, and its intercalation with metals. Clean metal surfaces were prepared by cycles of Ar^+ ion bombardment and annealing. Subsequently, the samples were exposed to oxygen to remove residual carbon segregated from the bulk. The Ru(0001) surface was always heated in O_2 atmosphere. All oxygen cycles were concluded by a flash annealing. Graphene was grown by an established chemical vapor deposition (CVD) method.[60] The hot metal surface is exposed to ethylene (C_2H_4), which initiates a self-limiting catalytic surface reaction producing epitaxial graphene. On Ru(0001) bilayer graphene (BLG) is obtained by additional carbon segregation to the surface during an extended cool-down phase after the monolayer graphene (MLG) growth.[60] Intercalants were evaporated from commercial dispensers (Cs, Li) or from a hot filament (Ni, Pt) and deposited onto graphene at room temperature. Post-annealing was performed to facilitate the intercalation process and remove the adatom phase. Table 2.1 summarizes the important parameters of the sample preparation.

2.2.3 Calibration

Since piezoelectric actuators may depolarize over time and their material properties depend on the temperature, the piezo constants need to be determined before each experiment. This calibration has been performed on the reconstructed Au(100) surface (Fig. 2.4), where characteristic parallel ridges occur with a lateral period of 14.4 Å, [61, 62] and verified at the graphene lattice constant (2.46 Å) on the prepared samples.

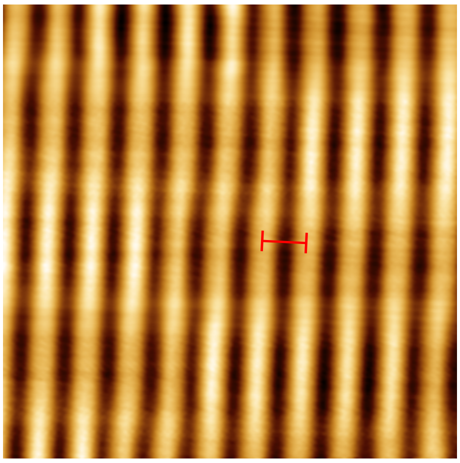

Figure 2.4: Constant-current STM image of the reconstructed Au(100) surface (bias voltage $V = 300\,\mathrm{mV}$, tunneling current $I = 100\,\mathrm{pA}$, $15 \times 15\,\mathrm{nm}^2$). The distance (red line) between the protruding ridges is 14.4 Å.[61, 62]

2.2.4 Analysis Software

STM topographic data was analyzed and post-processed with WSxM.[63] Conversion and analysis of $\mathrm{d}I/\mathrm{d}V$ and $\mathrm{d}^2I/\mathrm{d}V^2$ spectra was performed in MATLAB.

2.3 Graphene Samples

2.3.1 Graphene

Graphene is a single layer of sp^2 hybridized carbon atoms arranged in a honeycomb lattice. Its unit cell contains two carbon atoms (A, B) that form two triangular sublattices. Every atom of one sublattice is connected to neighboring atoms of the other sublattice by strong in-plane σ-bonds [Fig. 2.5(a)]. The p-orbitals are oriented perpendicular to the lattice plane and form an extended delocalized π-system. Besides a remarkable mechanical stability, [65] this network creates a unique electronic band

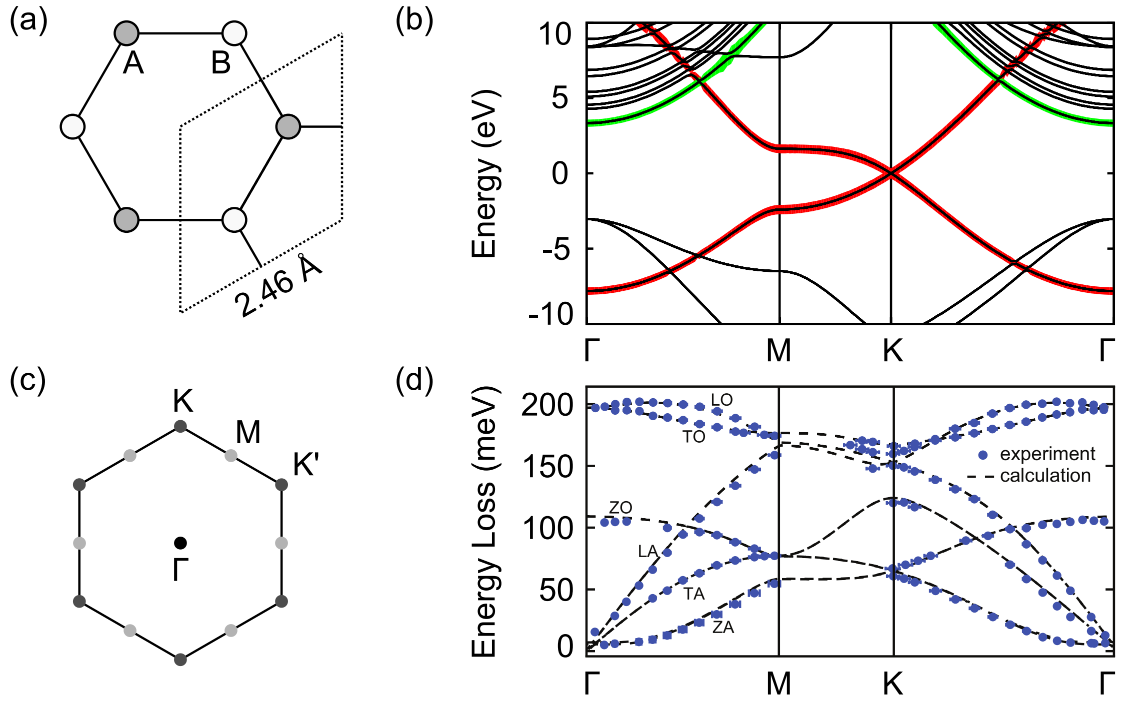

Figure 2.5: Properties of graphene. (a) Primitive unit cell of graphene (dotted) with the two triangular sublattices A, B of the honeycomb lattice. (b) Electronic band structure of graphene. The so-called Dirac cone is situated at the crossing point of the linear dispersing π-bands (red) at K/K . The first unoccupied σ-band of graphene (green) plays an important role in the inelastic electron tunneling into graphene (section 3.1).[24] (c) First Brillouin zone of graphene with labeled high symmetry points. (d) Calculated phonon dispersion of graphene together with experimental data obtained with EELS. Branches are characterized by longitudinal (L), transversal (T), and out-of-plane (Z) displacement, and by optical (O) or acoustic (A) character.

Reprinted with permission from T. O. Wehling et al., Phonon-mediated tunneling into graphene. Phys. Rev. Lett., 101: 216803, 2008. Copyright (2008) by the American Physical Society.[30]

Reprinted with permission from M. Endlich et al., Screening of electron-phonon coupling in graphene on Ir(111). Phys. Rev. B, 88: 205403, 2013. Copyright (2013) by the American Physical Society.[64]

structure [Fig. 2.5(b)]. In the proximity of the K/K points of the Brillouin zone (BZ) [Fig. 2.5(c)] the π-bands disperse linearly, following the Dirac-Weyl description of massless fermions, [66] and cross at K/K at the Fermi energy. These characteristic features are referred to as Dirac cones and give rise to a variety of astonishing characteristics and effects, [67] such as the anomalous quantum Hall effect [3, 4] and the ballistic transport of charge carriers at room temperature.[68]

As will be presented in section 3.1 the coupling between the Dirac electrons and graphene phonons yields a sizable increase in the differential conductance when inelastic tunneling occurs. Figure 2.5(d) shows the calculated phonon dispersion of pristine graphene together with electron energy loss spectroscopy (EELS) data of weakly-coupled MLG/Ir(111).[64] In this thesis, the optical and acoustic out-of-plane phonons (ZO and ZA branches) as well as the transverse acoustic mode (TA) are examined with IETS. They exhibit a flat dispersion in the proximity of the M point, which entails a comparably large phonon DOS, making them particularly relevant for inelastic electron transport. When pristine graphene is placed on metal substrates, its phonon dispersion is altered. Well-known effects are the emergence of additional Kohn anomalies due to electron-phonon coupling, [69] but also the weakening [64] or complete suppression [70] of existing Kohn anomalies. Other examples include the lifting of the ZA/ZO degeneracy at K/K [70] and the emergence of phonon replica bands due to moiré patterns.[71] Most of these changes in the phonon dispersion are governed by the graphene–substrate hybridization, by screening effects, [64] or by the reduced symmetry of graphene on a metal surface.[70, 72]

2.3.2 Metal Substrates

All three substrates used in this work – Ir(111), Ru(0001), and Pt(111) – are transition metals with partly filled d-orbitals. Besides Ru being a hcp crystal, while Ir and Pt arrange in fcc structure, the main difference between these substrates is their binding strength with graphene along with accompanying effects on topography, electronic band structure, and phonon dispersion. Table 2.2 summarizes important topographic and electronic characteristics of the three graphene/substrate systems to provide a basis for understanding the experimental data presented in the following chapters. Ir(111) and Pt(111) interact only weakly with graphene. In both cases a marginal p-doping occurs [Table 2.2]. For Ru(0001) on the other hand, the coupling to graphene is strongly site-dependent.[10, 80] In regions of the moiré pattern, where carbon hexagons are centered above substrate hollow sites, the Ru 4d-bands hybridize

	Ir(111)	Ru(0001)	Pt(111)
lattice constant	2.715 Å	2.706 Å	2.775 Å
interaction	weak	strong	very weak
moiré corrugation	0.3 Å [73, 74]	0.82 Å [11]	0.53 Å [75]
binding distance	3.77 Å [73]	2.0 Å [76]	3.3 Å [77, 78]
shift of Dirac cone	+0.1 eV [79]	+0.3 eV [11]	+0.3 eV [78]

Table 2.2: Comparison of the three prepared graphene/substrate systems: substrate lattice constant, graphene-substrate interaction strength, geometric MLG moiré corrugation, minimum binding distance between graphene and substrate in the moiré unit cell, shift of the Dirac cone. *For Ru(0001) the given value corresponds to the on-top sites of the moiré pattern. Elsewhere the strong hybridization of the π-bands disrupts the Dirac cone.

strongly with the graphene π-bands. This gives rise to a band gap of $\approx 2\,\text{eV}$ at K/K and a downshift of the π-bands to higher binding energies. In the on-top sites of the moiré pattern, where carbon hexagons are centered above Ru atoms, the graphene is well decoupled and the Dirac cone intact.[10, 11]

All three substrates have advantages and disadvantages regarding research and potential applications of graphene. Ir(111) offers the growth of a single orientational domain of weakly-coupled graphene but lacks convenient growth methods for graphene multilayers. These can be prepared readily on Ru(0001) at the price of a strongly hybridized bottom graphene layer. In this work, a CVD-based preparation method for well decoupled bilayer graphene on Pt(111) is presented (chapter 4).

2.4 Analysis of Moiré Patterns

Reproduced in part with permission from
Phys. Chem. Chem. Phys., 21: 3140-3144, 2019.
Copyright 2019 Royal Society of Chemistry.

Moiré patterns are spatial beating patterns generated by the superposition of two or more lattices of different orientations or different spatial periods. They often occur when graphene overlayers are supported by a substrate or by other layered materials [Fig. 2.6(a)]. Inside the moiré unit cell, there are regions of distinct local stacking, e.g., carbon hexagons sitting on top of substrate atoms or in hcp or fcc hollow sites of fcc(111) surfaces. These different sites of the moiré pattern induce a periodic modification of the graphene–substrate interaction. The corrugation observed on a moiré pattern increases with the interlayer coupling [8, 40] and the induced superstructure impacts the electronic [79] and vibrational properties [71] of graphene. Typical spatial periods of graphene moiré patterns are on the scale of few nm. In combination with measured orientations of the moiré and the topmost surface layer, they provide information about the atomic layers beneath the observable graphene sheet. Moreover, even small changes in the stacking of the contributing lattices are magnified in the moiré pattern, which makes it a valuable indicator for disturbances like strain, defects, and domain walls.[81, 82]

2.4.1 Monolayer Graphene

The reciprocal lattice vectors of substrate[a] $\mathbf{k}_{\mathrm{sub}}$, graphene $\mathbf{k}_{\mathrm{C}}$, and moiré pattern $\mathbf{k}_{\mathrm{m}}$ form a triangle following the relation [83, 84]

$$\mathbf{k}_{\mathrm{m}} = \mathbf{k}_{\mathrm{C}} - \mathbf{k}_{\mathrm{sub}} \tag{2.4}$$

as shown in Fig. 2.6(b). Their magnitudes $k = |\mathbf{k}|$ are defined as $k_{\mathrm{sub}} = 1/a_{\mathrm{sub}}$, $k_{\mathrm{C}} = 1/a_{\mathrm{C}}$, $k_{\mathrm{m}} = 1/a_{\mathrm{m}}$ with the spatial periods $a_{\mathrm{sub}}, a_{\mathrm{C}}, a_{\mathrm{m}}$ of substrate, graphene, and moiré, respectively. The three angles of the triangle are the twist angle $\theta = \angle(\mathbf{k}_{\mathrm{C}}, \mathbf{k}_{\mathrm{sub}})$ between graphene and substrate, the angle between moiré and substrate $\sigma = \angle(\mathbf{k}_{\mathrm{m}}, \mathbf{k}_{\mathrm{sub}})$, and between moiré and graphene $\quad = \angle(\mathbf{k}_{\mathrm{m}}, \mathbf{k}_{\mathrm{C}})$. All of them are defined as the smallest angles enclosed by the respective lattice orientations and, due to the hexagonal symmetry of the contributing lattices, limited to the interval $[-30°, 30°]$.

From this triangle, the lattice constants and orientations of the moiré and its contributing lattices can be analyzed or predicted. Strain may be included explicitly through a scaling factor for the respective lattice constant. For MLG, the expected evolution of a_{m} with the twist angle θ is useful for comparison with experimental data and is readily derived by applying the law of cosines, which yields

$$a_{\mathrm{m}} = \left(\quad \overline{\frac{1}{a_{\mathrm{C}}^2} + \frac{1}{a_{\mathrm{sub}}^2} - \frac{2\cos\theta}{a_{\mathrm{C}} \quad a_{\mathrm{sub}}}} \right)^{-1} . \tag{2.5}$$

---

[a] Only substrates with surface layers of hexagonal symmetry are considered and relevant for the presented experiments.

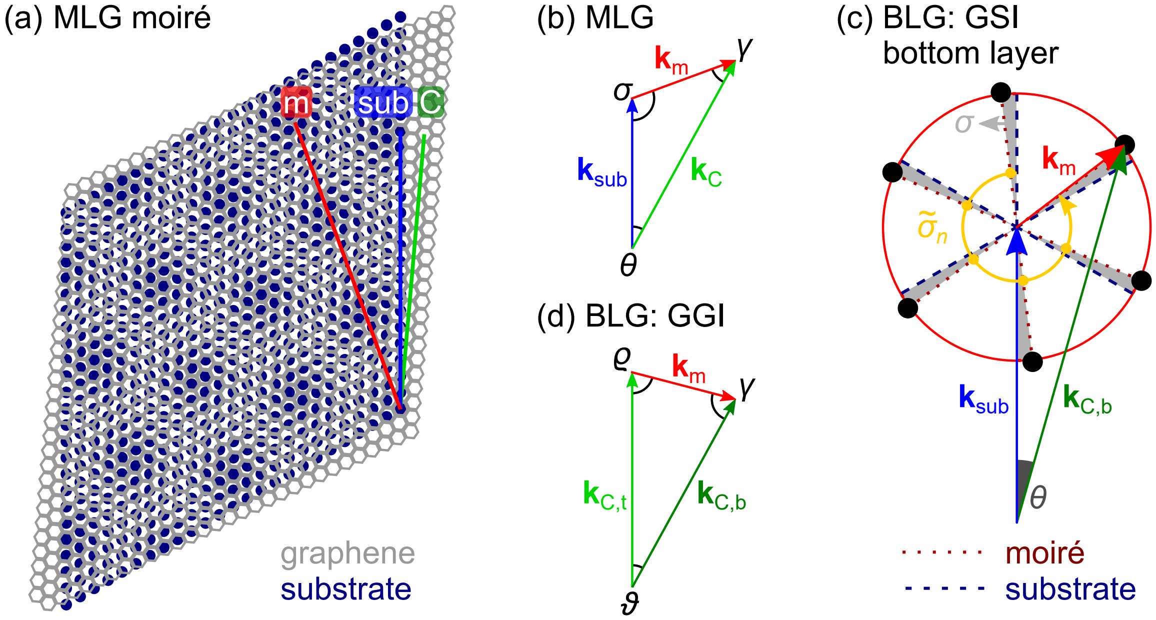

Figure 2.6: Illustration of the moiré analysis. (a) Example of a moiré pattern generated by MLG on a substrate. The varying contrast is due to regions of locally different stacking. Orientations are labeled m, sub, C for moiré, substrate, and graphene, respectively. (b) MLG: Triangle formed by the three lattice vectors with defined angles. (c) BLG: Characterization of the bottom graphene layer based on the moiré caused by the graphene–substrate interface (GSI) and, therefore, without contribution of the top graphene layer. Lattice constant $a_\mathrm{C,b}$ and twist angle θ are determined based on given a_m, σ, and a_sub. Six moiré orientations defined by $\tilde{\sigma}_\mathrm{n}$ are experimentally indistinguishable due to the hexagonal symmetry of the contributing lattices. Symmetry axes of moiré and graphene are indicated by dashed lines. Out of the six possible constellations (black dots), the scenario yielding the smallest strain in graphene is considered most plausible. (d) BLG: Triangle of lattice vectors for a moiré pattern caused by the graphene–graphene interface (GGI) of twisted BLG. Indices t and b denote top and bottom graphene layer, respectively.

2.4.2 Bilayer Graphene: Characterization of the Bottom Layer

For a moiré pattern observed on BLG, there are two possible origins.[b] It can either be caused by (i) the graphene–substrate or (ii) the graphene–graphene interface. Both cases have been reported [40, 85, 86] and need to be considered. In the following, it is shown how for both scenarios the lattice constant $a_\mathrm{C,b}$ and the respective twist angle of the "hidden" bottom graphene layer can be obtained. For the analysis of the various MLG and BLG moiré patterns that occurred in the presented experiments, the described algorithms have been implemented in MATLAB scripts.

---

[b] More complex situations like moiré patterns caused by other moiré patterns are not considered here.

(i) Graphene Substrate Interface (GSI)

In this case, the unknown parameters are $a_{\mathrm{C,b}}$ and the twist angle θ between bottom graphene layer and substrate. Experimentally determined values for a_{m} and σ are available.[c] The substrate lattice constant is assumed fixed to the literature value or measured independently. Due to the hexagonal symmetry of the contributing layers, there are six moiré orientations that are indistinguishable in the experiment but can be defined by virtual moiré angles $\tilde{\sigma}_{\mathrm{n}}$ [Fig. 2.6(c)] with $\tilde{\sigma}_{\mathrm{n}} = \sigma + n\ 60^\circ$ $(n = 1, 2, ..., 5)$. Each $\tilde{\sigma}_{\mathrm{n}}$ corresponds to a different solution $(a_{\mathrm{C,b}},\ \theta)$, where

$$a_{\mathrm{C,b}} = \left(\overline{\frac{1}{a_{\mathrm{sub}}^2} + \frac{1}{a_{\mathrm{m}}^2} + \frac{2\cos\tilde{\sigma}_{\mathrm{n}}}{a_{\mathrm{sub}}\ \ a_{\mathrm{m}}}} \right)^{-1}. \tag{2.6}$$

The solution with minimal strain $a_{\mathrm{C,b}}$ in the graphene is considered most plausible and the corresponding twist angle θ is determined by

$$\sin\theta\ \ = \frac{a_{\mathrm{C,b}}}{a_{\mathrm{m}}} \sin\tilde{\sigma}_{\mathrm{n}}. \tag{2.7}$$

It should be noted that the presented path is not the only option to determine characteristics of the bottom graphene layer. Instead of basing the calculations on the angle σ, one could perform a very similar analysis with the measured as starting point – or even with both, leaving the substrate lattice constant variable, too [see Figs. 2.6(b,c)]. However, the differences between these methods are marginal for sufficiently precise measurements of the angles and the moiré spatial period.

(ii) Graphene Graphene Interface (GGI)

For the comparison to experimental data, the spatial period of moiré patterns generated by two twisted graphene layers (twist angle) can be calculated analogously to Eq.2.5

$$a_{\mathrm{m}} = \sqrt{\frac{1}{a_{\mathrm{C,b}}^2} + \frac{1}{a_{\mathrm{C,t}}^2} - \frac{2\cos}{a_{\mathrm{C,b}}\ \ a_{\mathrm{C,t}}}}^{\,-1} \tag{2.8}$$

with $a_{\mathrm{C,t}}$ denoting the lattice constant of the top graphene layer.

The bottom graphene layer can be characterized using a similar algorithm as described in the previous section. Here, instead of the substrate, the top graphene layer takes the role of the fixed reference lattice with known spatial period $a_{\mathrm{C,t}}$ and orienta-

---

[c] The substrate orientation can be determined from edge dislocations or step edges.

tion.[d] The experimentally determined angle between moiré lattice and top graphene orientation is $\quad = \angle(\mathbf{k}_{\mathrm{m}}, \mathbf{k}_{\mathrm{C,t}})$. The triangle of lattice vectors containing all relevant quantities is shown in Fig. 2.6(d). Again, six solutions defined by virtual moiré angles $\tilde{}_{\mathrm{n}}$ are possible for $a_{\mathrm{C,b}}$

$$a_{\mathrm{C,b}} = \quad \sqrt{\frac{1}{a_{\mathrm{C,t}}^2} + \frac{1}{a_{\mathrm{m}}^2} + \frac{2\cos\tilde{}_{\mathrm{n}}}{a_{\mathrm{C,t}}\quad a_{\mathrm{m}}}}^{\quad -1}. \tag{2.9}$$

The twist angle between the two layers is given by the solution $a_{\mathrm{C,b}}$ corresponding to the lowest strain. Following Eq. 2.7 yields

$$\sin \quad = \frac{a_{\mathrm{C,b}}}{a_{\mathrm{m}}} \sin\tilde{}_{\mathrm{n}}. \tag{2.10}$$

---

[d] Throughout this work, atomic resolution on BLG has been achieved much more easily than on MLG. Its lattice constant agrees extremely well with the literature value indicating the absence of strain.

3 Understanding and Engineering Inelastic Excitations in Graphene

The invention of the STM in the early 1980s [87, 88] has added new value to inelastic electron tunneling spectroscopy (IETS), which was originally developed 1966 in metal-insulator-metal junctions.[89] Inelastic signals have since been spatially resolved at the nanoscale, e.g., on single molecules. IETS spatial mapping [51] yields insight in molecule configuration and adsorption geometry, and contributes to the understanding of fundamental mechanisms in inelastic electron tunneling. While differential conductance increases induced by molecular vibrational quanta are typically in the range of only few percent, [23] recent IETS studies of graphene have revealed huge vibrational signals leading to changes in the $\mathrm{d}I/\mathrm{d}V$ by more than 100 %.[22, 24, 26–28] However, at present the occurrence of graphene phonon signals in IETS is far from being understood. This chapter presents two experiments that contribute to a progress in this regard. In the first experiment intercalation is applied as a tool to study inelastic excitations in graphene on Ir(111) using varying types and coverages of intercalants. In combination with accompanying transport calculations these experiments give a general insight into the inelastic tunneling into graphene and the impact of certain interface properties. In the second section, spatially resolved IETS on monolayer and bilayer graphene on Ru(0001) is performed. The obtained data hint at a spatial variation of the electron-phonon coupling in the moiré unit cell and provide a basis for further experiments and calculations.

3.1 Phonon-Mediated Tunneling into Intercalated Graphene on Metal Surfaces

Reproduced in part with permission from
Nano Lett., 18(9): 5697–5701, 2018.
Copyright 2018 American Chemical Society.
Theoretical support was provided by Mads Brandbyge from the Technical University of Denmark, Department of Micro- and Nanotechnology.

Metal-intercalated graphene on Ir(111) exhibits clear phonon signatures in IETS with strengths that depend on the intercalant. Extraordinarily strong graphene phonon signals are observed for Cs intercalation. Li intercalation likewise induces clearly discriminable phonon signatures, albeit less pronounced than observed for Cs. The signal can be finely tuned by the alkali metal coverage and gradually disappears upon increasing the junction conductance from tunneling to contact ranges. In contrast to Cs and Li, for Ni-intercalated graphene the phonon signals stay below the detection limit in all transport ranges. Going beyond the conventional two-terminal approach, transport calculations provide a comprehensive understanding of the subtle interplay between the graphene–electrode coupling and the observation of graphene phonon spectroscopic signatures.

3.1.1 Introduction

Inelastic electron tunneling spectroscopy with a STM has so far been used to explore phonons of graphene on semiconducting or nearly insulating substrates including SiC, [22] SiO_2, [24, 26] and SiO_2 covered with hexagonal boron-nitride.[27, 28] However, only recently have first reports of IETS phonon signals from graphene on metals been published. They examined delaminated graphene nanostructures on Pt(111) [29] and Ir(111).[25] All these reports convey the general impression that nearly free graphene, *i. e.*, a weak graphene–substrate hybridization, favors the conservation of the genuine graphene electronic structure and the concomitant phonon-mediated tunneling.[22, 24–29] Yet in some tunneling spectroscopy studies of exfoliated graphene on SiO_2 phonon signatures were not observed.[90, 91] To date, experiments and simulations have solely considered the weak hybridization limit. Moreover, the coupling between graphene and adjacent electrodes has not been modeled explicitly. Therefore, the relation between the signal strength of graphene phonon signatures in IETS and the graphene–electrode coupling has remained elusive.

This section presents a combination of IETS experiments and transport calculations, which unambiguously unveils the intimate relation between the covalent graphene–electrode coupling and the IETS signal strength of graphene phonons. In contrast to previous work, [22, 24–29, 40] graphene-covered Ir(111) intercalated by Cs, Li, or Ni represents an all-metal complex in which the graphene–substrate interaction is tailored by the chemical nature and the amount of the intercalant. Transport calculations based on density functional theory (DFT) using a multi-electrode setup enable the analysis of the branching of the electron current from the STM tip into graphene and the substrate. The DFT findings are translated into a simplified two-level model that provides an intuitive understanding of the relation between the graphene–electrode hybridization and the effective phonon excitation.

3.1.2 Experimental Details

Sample preparation and STM measurements were performed as described in chapter 2. Only for the data presented in Fig. 3.2(b) was Li evaporated onto the hot sample at a temperature of 630 K. The Li coverage was then progressively increased by deposition of additional Li. Tips were fabricated from chemically etched W wire coated in situ with Au. Intercalant coverages Θ were determined by measuring the fraction of covered surface area in STM images and multiplying it with the fraction of carbon rings occupied with intercalant atoms. Based on the known atomic arrangement of the intercalated species, this fraction is 33 % for $(\sqrt{3} \times \sqrt{3})\,\mathrm{R}30^\circ$ Li [92] and 50 % for (2×2) Cs.[15] The highest coverage of the Li-intercalated sample was estimated from the evaporation time and rate based on a calibration at lower coverage data.

3.1.3 Results and Discussion

Topography

Intercalation of monolayer graphene (MLG) on Ir(111) with Cs [Fig. 3.1(a)], Li [Fig. 3.1(b)], and Ni [Fig. 3.1(c)] leads to the formation of intercalant islands of monatomic height beneath the graphene sheet. With respect to the honeycomb lattice of graphene, Cs intercalates with (2×2) and Li with $(\sqrt{3}\times\sqrt{3})$ R30° superstructure.[15, 92] For Ni intercalation, previous experiments indicated a pseudomorphic growth on Ir(111).[20] Due to the varying hybridization of the intercalant layers with graphene, the corrugation of the moiré pattern changes on the intercalated islands compared

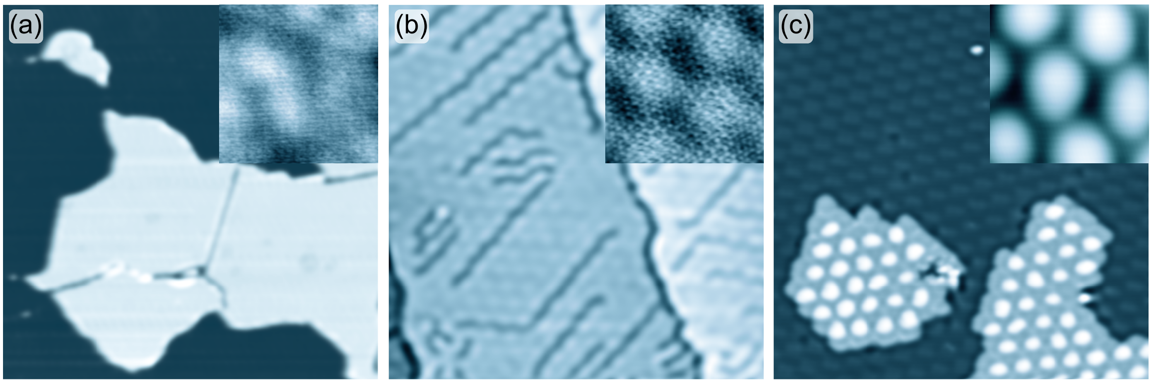

Figure 3.1: Constant-current STM images ($V = 120\,\text{mV}$, $I = 100\,\text{pA}$) of graphene-covered Ir(111) intercalated by (a) Cs ($100 \times 100\,\text{nm}^2$), (b) Li ($50 \times 50\,\text{nm}^2$), (c) Ni ($40 \times 40\,\text{nm}^2$). Insets to (a)–(c): Close-up views ($5.5 \times 5.5\,\text{nm}^2$). In (b), (c) graphene moiré patterns are visible. The apparent height scale of the insets ranges from 0 pm to (a) 10 pm, (b) 30 pm, (c) 150 pm.

to pristine MLG/Ir(111) areas, which display a corrugation of 19 ± 1 pm.[92] At the same tunneling parameters the corrugation of Cs-intercalated graphene is below the resolution limit of the STM, while Li and Ni intercalation yield a peak-to-peak corrugation of 9 ± 1 pm and 105 ± 3 pm, respectively. Since the buckling of graphene caused by the moiré pattern is as a qualitative measure of the graphene–substrate hybridization, [8, 20] graphene on Cs may be classified as well decoupled, shows a weak substrate coupling when intercalated with Li, and is strongly hybridized with the Ni film.

Impact of Different Intercalants

All three samples were characterized by IETS. The first clear observation is a gap-like feature, symmetrically positioned around zero bias, in the obtained $g := \mathrm{d}I/\mathrm{d}V$ spectra of Cs and Li intercalated graphene [Fig. 3.2(a) upper panel]. Here, abrupt increases of $g(V)$ occur at ±56 mV and ±75 mV. On the Cs-intercalated sample they give rise to an enhancement of g to roughly 200 % of the differential conductance at zero bias, $g(0)$. These changes are assigned to out-of-plane and transverse acoustic (±56 mV), and out-of-plane optical (±75 mV) graphene phonons from the proximity of the M point of the surface Brillouin zone [inset to Fig. 3.2(a)], where the respective dispersion branches are comparably flat (Fig. 2.5). This is in accordance with previous results reported for graphene wrinkles.[25] For Li-intercalated graphene, the same phonon spectroscopic signatures are visible, albeit to a smaller extent. Here, g is increased to $\approx 140\,\%$ of $g(0)$ at a Li coverage of $\Theta = 0.27\,\text{ML}$. Ni-intercalated

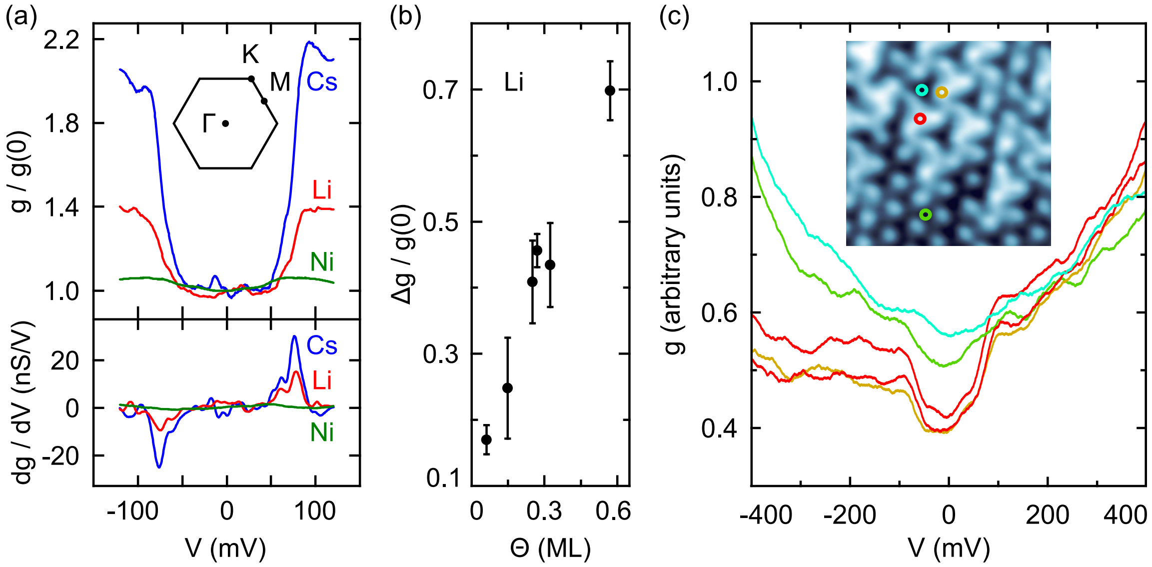

Figure 3.2: (a) Top panel: $g \coloneqq \mathrm{d}I/\mathrm{d}V$ spectra of the intercalated samples, normalized to the zero-bias differential conductance, $g(0)$. Cs and Li data exhibit step-like signatures that are ascribed to the excitation of graphene phonons, while Ni data are essentially featureless. Inset: Surface Brillouin zone of graphene with indicated high-symmetry points. Bottom panel: Numerical derivative ($\mathrm{d}g/\mathrm{d}V$) of the spectra in the top panel. (b) Phonon-induced change in $\mathrm{d}I/\mathrm{d}V$ (Δg) divided by the zero-bias differential conductance $g(0)$ as a function of the Li coverage Θ. (c) Spatially resolved $g(V)$ spectra for a Li coverage of 0.15 ML. Inset: STM image (180 mV, 100 pA, $20 \times 20\,\mathrm{nm}^2$) of Li-intercalated graphene with indicated spectroscopy probing positions. The phonon-induced gap is best seen above intercalated regions (red and dark yellow circles and lines), while it virtually disappears above regions without intercalant (green and blue circles and lines).

graphene, however, does not reveal any discernible variations in $g(V)$ caused by phonon excitations.

Second, the phonon-induced changes in $\mathrm{d}I/\mathrm{d}V$ may be controlled to some extent by the coverage of the intercalant. For Li we found that in the low submonolayer range relative changes, $\Delta g/g(0)$, are $\approx 17\,\%$ and increase up to $\approx 70\,\%$ for the densely packed Li film [Fig. 3.2(b)]. The formation of compact Cs islands even at low coverage hampered similar measurements for Cs-intercalated graphene.

Third, for all three samples a dependence of the spectra on the tip position over the intercalated graphene regions was not discernible. Figure 3.2(c) demonstrates at the example of the Li-intercalated sample that graphene phonon signals are absent on flat graphene on Ir(111) and exclusively appear above the nanostructures formed by the intercalant.[92] In these intercalated regions, $\mathrm{d}I/\mathrm{d}V$ spectra were virtually identical. Only at the very edges of the nanostructures the phonon signals vanished quite abruptly.

Transport Calculations

In order to thoroughly understand the experimental results, transport calculations based on DFT were performed.[a] They reveal the role of the different intercalants and the graphene–substrate as well as the graphene–tip coupling in the IETS signal strength for graphene phonons. In the following, tip and substrate will often be referred to as electrodes for simplicity. The setup for the calculations is illustrated in the inset of Fig. 3.3(a) at the example of Cs-intercalated graphene. The substrate consists of four Ir(111) layers and for graphene a (6×6) unit cell was used with a 2×2 k-point sampling. The Ir slab was kept fixed and strained by $\approx 2\,\%$ to match the graphene unit cell dimensions, while the intercalant (Cs or Li) and graphene were relaxed. Both alkali metals give rise to a considerable n-doping of graphene corresponding to a Fermi energy of $\varepsilon_{\mathrm{F}} \approx 1\,\mathrm{eV}$. The tip was modeled as a Au pyramid attached to a bulk Ir electrode. The relaxed structures served as an input to subsequent nonequilibrum Green function (NEGF) calculations.

Remarkably, the standard approach with Γ-point approximation, two terminals – tip and substrate – and periodic boundary conditions in the transverse directions does not reproduce the experimental data well. It yields vanishingly small inelastic signatures in the current, even for Cs [Fig. 3.3(a), bottom data set]. However, introducing graphene self-energies, which is equivalent to attaching a third terminal that collects electrons propagating in graphene alone, allows for an improved modeling of the electron transport in graphene.[93] The added graphene terminal circumvents the limited resolution of a discrete k-point sampling and results in a substantial enhancement of the phonon signatures. In addition, with this setup the current branching into metal substrate and into graphene can be determined. The calculated $g(V)$ spectra in Fig. 3.3(a) demonstrate that the three-terminal model can qualitatively reproduce the experimental findings for MLG/Ir(111) intercalated by (2×2) Cs and $(\sqrt{3} \times \sqrt{3})$ R30° Li. Quantitatively, the same order of magnitude for the phonon-induced changes in $g/g(0)$ is calculated, although they exceed the experimental values.

An analysis of relevant graphene phonon modes in the calculations is shown in Fig. 3.3(b,c). The main contributions stem indeed from the flat dispersing out-of-plane bands between M and K, but the symmetry breaking by the substrate also

---

[a] Details of the calculation can be found in the appendix section A.

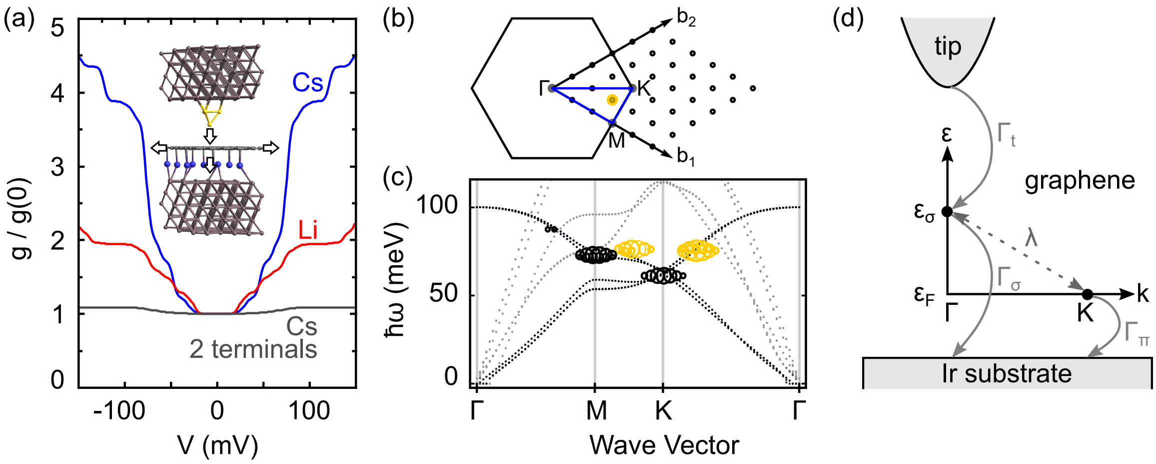

Figure 3.3: (a) Calculated $g/g(0)$ for graphene on Ir(111) intercalated by $(2{\times}2)-$Cs and $(\sqrt{3}\times\sqrt{3})$ R30° − Li superlattices in the three-terminal setup. In the conventional two-terminal approach (calculated for Cs, bottom curve) IET signals are virtually absent. Inset: Setup for the calculations indicating (arrows) the presence of three terminals that collect propagating electrons in the tip, substrate, and graphene. (b) The graphene Brillouin zone with high-symmetry points Γ, M, K is spanned by reciprocal lattice vectors $\mathbf{b}_1$ and $\mathbf{b}_2$. Dots mark the k-points of the (6×6) supercell. The k-point marked with a yellow circle is contributing to the inelastic signals besides M and K. (c) Contributing phonon modes of graphene. Black (gray) bands depict the effective dispersion of out-of-plane (in-plane) phonons. Circles are placed at the phonon energy $\hbar\omega$ with a radius indicating the IETS signal strength. The contributions in yellow stem from the k-point marked in (b). Only phonon modes with strongest contributions are shown. (d) Simplified model of the electron transport in the three-terminal setup. The tip couples to graphene σ-states with energy ε_σ at Γ with a coupling constant Γ_t. The hybridization of graphene to the substrate is mediated by σ-states with strength Γ_σ and by π-states with strength Γ_π. π-states occur at K with energy ε_F (Fermi energy). σ and π-states are coupled by the electron-phonon interaction λ.

yields few contributions shifted away from these. Overall this is in good agreement with a recent theoretical model put forward to describe phonon-mediated tunneling into pristine graphene.[25, 30] For the analysis, the phonon modes of the (6×6) graphene supercell used in the calculations have been projected onto the effective phonon dispersion of the pristine graphene unit cell. The approximate effective phonon band dispersion was formed by averaging the supercell dynamical matrix over unit cells separated by linear combinations of the primitive real space unit vectors. This approach was inspired by previous work on the effective band structures of alloys.[94]

Two-Level Model

The findings based on density functional and transport calculations can be illustrated in a simple two-level model [Fig. 3.3(d)]. This model explains the inelastic electron transport from the STM tip via the intercalated graphene into the substrate. It involves the first unoccupied σ-band of graphene with energy ε_σ at Γ and a graphene π-state with energy ε_F (Fermi energy) at K, similar to a previous approach.[30] The coupling of these states to the metal substrate is modeled by inverse lifetimes, Γ_σ and Γ_π, where $\Gamma_\sigma > \Gamma_\pi$ due to the long range of σ.[95] Additionally, the σ-state is coupled to the tip with Γ_t. Electrons injected from the tip into σ can either directly continue to the substrate, which constitutes the elastic transport channel, or take the detour via π through electron–phonon coupling with strength λ. In this purely inelastic transport channel a phonon with energy $\hbar$ is excited. For $\hbar \quad \Gamma_\pi$ the relative conductance increase due to the phonon excitation can be expressed as

$$\frac{\Delta g}{g(0)} = \frac{4\lambda^2}{\Gamma_\pi} \quad \frac{1}{\Gamma_\mathrm{t}} + \frac{1}{\Gamma_\sigma} \quad . \tag{3.1}$$

in the lowest-order expansion of the electron–phonon coupling and in the wide-band approximation.[96, 97] In the tunneling range ($\Gamma_\sigma \quad \Gamma_\mathrm{t}$) this expression may be further simplified to

$$\frac{\Delta g}{g(0)} = \frac{4\lambda^2}{\Gamma_\pi \Gamma_\mathrm{t}}. \tag{3.2}$$

Thus, for similar Γ_t and comparable λ, the IETS signal is controlled by Γ_π. Equations 3.1 and 3.2 offer an intuitive explanation of the intercalant-dependent phonon signal intensity as well as the evolution of $\Delta g/g(0)$ with Li coverage. Moreover, the IETS signal strengths of graphene phonons on other surfaces [22, 24–29, 40] may be understood, too. These aspects are addressed in the following.

A reduction of the coupling Γ_π between graphene and substrate corresponds to a longer lifetime of the π-state, which evokes a stronger interaction of π-electrons with graphene phonons and, therefore, enhances the IET signals. Thus, based on the experimental data [Fig. 3.2(a)] it can be concluded that graphene on the Cs-intercalated samples is less hybridized with the metal than on Li-intercalated samples, which is also consistent with the essentially vanishing moiré corrugation of graphene atop the Cs layer [Fig. 3.1(a)]. In Ni-intercalated MLG/Ir(111) on the other hand the graphene π-states are strongly hybridized with Ni $3d$ bands, [20] which in the simple model is reflected by a very large Γ_π. As a consequence, the interaction of the π-electrons with graphene phonons is reduced and renders the inelastic channel inefficient. Here, the current flows mainly through the elastic channel, i.e., directly into the bulk of the metal substrate and the phonon signatures vanish from the spectra.

The increase in $\Delta g/g(0)$ with Li coverage Θ [Fig. 3.2(b)] is likely due to a similar mechanism. A higher coverage of the Li intercalant progressively reduces the graphene-substrate coupling, Γ_π, and concomitantly yields larger graphene phonon signals. Here, an additional effect is the charge transfer from Li to graphene, which leads to n-doping and may promote the phonon signal intensity by enhancing the density of states at the Fermi energy.[24, 26–28] The experimental data shows that even on the densely packed Li film (global coverage, $\approx 0.6\,\mathrm{ML}$), the IETS intensity is still well below that of the Cs-intercalated sample [Fig. 3.2(a,b)]. Since Li and Cs provide similar doping at equal coverage [98] this observation cannot be explained by the charge carrier density alone, contrary to previous results, [24, 26–28] and demonstrates the necessity of a comprehensive description.

The model presented here can likewise explain the extraordinarily strong phonon signals observed from graphene on insulating and semiconducting surfaces, [22, 24, 26–28] graphene blisters on Pt(111) [29] and Ir(111),[25] and from graphene bilayers on Ir(111).[40] The common characteristic in all these systems is the low substrate LDOS at the Fermi energy at the location of the (topmost) graphene layer. The resulting weak hybridization of graphene with substrate states at the Fermi energy yields not only a small Γ_π, but a reduced Γ_σ, too. This scenario corresponds to $\Gamma_\sigma \approx \Gamma_\mathrm{t} \approx \Gamma_\pi$ (Eq. 3.1). With all lifetimes of the relevant electronic states being comparably large, the interaction with phonons is now vastly enhanced. In the picture of tunneling channels, an efficient inelastic transport is combined with a small elastic current and leads to exceptionally large IETS signal intensities. Applied to the experimental data presented here and in previous reports, the presented model demonstrates how Γ_π and Γ_σ act as control parameters that tune the efficiency of the elastic and inelastic tunneling pathways. Thus, they regulate the intensity of graphene phonon signals in IETS.

The occasional absence of phonon spectroscopic signatures in $\mathrm{d}I/\mathrm{d}V$ spectra obtained for exfoliated graphene on $\mathrm{SiO_2}$ [90, 91] may be caused by a substantial disorder potential that is caused by charged impurities and single-electron charging effects at the graphene–$\mathrm{SiO_2}$ interface.[91] The breaking of the graphene lattice symmetry in such weak-disorder systems enables elastic tunneling directly into graphene.[99] As a secondary effect, upon symmetry breaking the momentum conservation is lifted and phonon modes from different regions of the surface Brillouin zone may contribute to the phonon-mediated channel, which lowers the resolution of distinct phonon signatures in the IETS.

Contact Experiments

Furthermore, there is a third relevant coupling constant, Γ_t, that contributes to the magnitude of the phonon signatures. Experimentally, this parameter is accessible by, e.g., varying the tip-sample distance. Figure 3.4(a) shows $g(V)$ spectra obtained in such a measurement on MLG/Ir(111) intercalated with Li. The respective data for Cs intercalation is depicted in Fig. 3.5(a). With increasing junction conductance, $G \coloneqq I/V$, from tunneling to contact ranges, the relative change in $g(V)$ upon phonon excitation is lowered. At contact [topmost data sets in Figs. 3.4(a) and 3.5(a)] the IET signatures of graphene phonons have essentially disappeared, which is in agreement with previous findings for graphene wrinkles on Ir(111).[25]

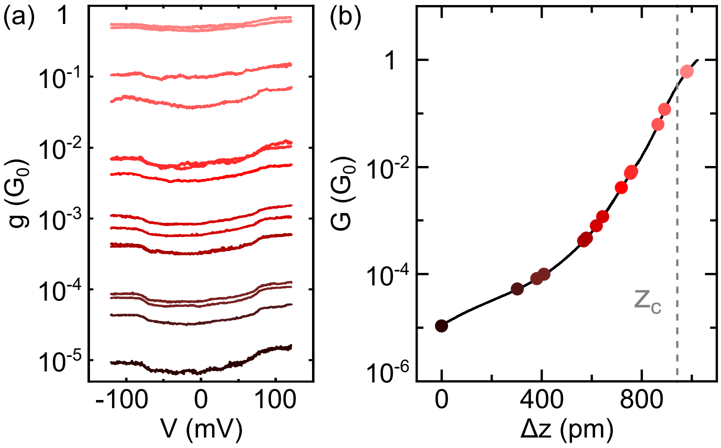

Figure 3.4: (a) Experimental dI/dV (g) spectra of Li-intercalated graphene for increasing (bottom to top) junction conductance showing the progressive quenching of the graphene phonon gap. Closely spaced spectra reflect data acquired at tip approach and retraction. (b) Junction conductance G as a function of the tip displacement Δz with z_c the contact point (dashed line). $\Delta z = 0\,\mathrm{pm}$ is defined by 120 mV, 100 pA. Each dot marks the junction conductance at which spectra in (a) were acquired.

The three different transport ranges are best visualized in the evolution of G with the tip displacement Δz [Figs. 3.4(b) and 3.5(c)]. With decreasing tip-sample separation the tunneling range, the transition range as indicated by the arrow in Fig. 3.5(c), and the contact range are reached successively. The displacement for contact formation, z_c, is defined by the intersection of exponential fits to conductance variations in the transition and contact ranges.[100, 101] Similar evolutions of the conductance were reported for graphene on Ru(0001).[102] Dots in Figs. 3.4(b) and 3.5(c) mark the setpoints, at which the feedback loop was deactivated during the acquisition of spectra. The experimentally observed quenching of phonon signatures is well captured by the three-terminal transport calculations as depicted in Fig. 3.5(b) for Cs-intercalated MLG/Ir(111).

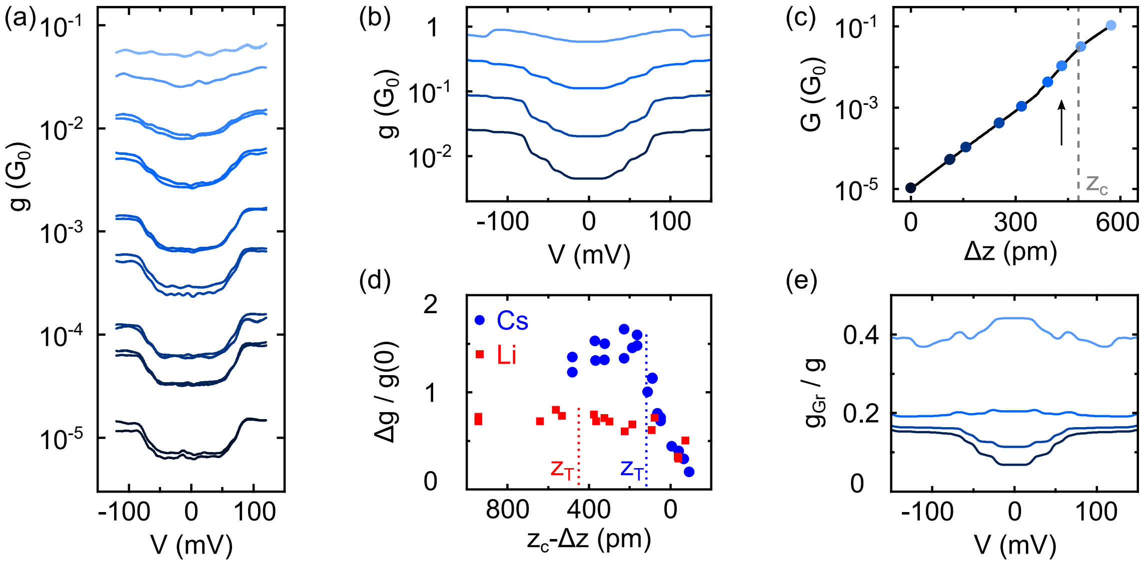

Figure 3.5: (a) Experimental $g(V)$ spectra of Cs-intercalated graphene for increasing (bottom to top) junction conductance showing the progressive quenching of the graphene phonon gap. Closely spaced spectra reflect data acquired at tip approach and retraction. (b) Simulated $g(V)$ spectra of Cs-intercalated graphene in the three-terminal model for junction conductances of 0.004 G_0, 0.02 G_0, 0.1 G_0, 0.6 G_0 (bottom to top). (c) Junction conductance G as a function of the tip displacement Δz with z_c the contact point (dashed line). $\Delta z = 0\,\mathrm{pm}$ is defined by 120 mV, 100 pA. The arrow indicates the transition from tunneling ($\Delta z < 365\,\mathrm{pm}$) to contact ($\Delta z > 486\,\mathrm{pm}$). Each dot marks the junction conductance at which spectra in (a) were acquired. (d) Phonon-induced relative changes, $\Delta g/g(0)$, for Cs (dots) and Li (squares) as a function of $z_c - \Delta z$ covering the range from tunneling to contact for both samples. The respective onsets $\mathrm{z_T}$ of the transition from tunneling to contact are indicated by dotted lines. (e) Relative contribution (g_Gr/g) of the graphene terminal to the total calculated differential conductance g for junction conductances as in (b).

A comparison of the evolution of $\Delta g/g(0)$ with junction conductance for graphene intercalated with Cs and Li[b] is shown in Fig. 3.5(d). Throughout all conduction ranges, the Cs-intercalated sample exhibits larger IETS signals than the Li-intercalated one. Since this difference cannot be rationalized in terms of a variation in the tip-

---

[b] The Li coverage is 0.27 ML as in Fig. 3.2(a)

sample distance alone, the stronger (weaker) phonon signal intensity of graphene intercalated with Cs (Li) is indeed caused by a smaller (larger) graphene–substrate coupling, respectively.

A close inspection of Fig. 3.5(d) reveals that the quenching of $\Delta g/g(0)$ in contact compared to the tunneling range is approximately twice as strong for Cs as for Li. Based on Eq. 3.1, such different evolutions of $\Delta g/g(0)$ with the tip-sample separation can be traced to varying distance dependencies of the three coupling constants Γ_σ, Γ_π, and Γ_t. During the tip approach, Γ_σ and Γ_π may be slightly reduced if graphene is locally detached from the surface due to the proximity of the tip. In previous contact experiments reported for graphene on Ru(0001) [102] and on Ir(111) [103] the elastic lifting of graphene was inferred from the gradual transition from tunneling to contact ranges in conductance-versus-distance data. Such concomitant changes of Γ_σ and Γ_π with tip-sample separation are expected to vary depending on the intercalant but would enhance the IETS signals as described above. Instead, the quenching of $\Delta g/g(0)$ seen in the experimental data indicates a dominating role of Γ_t when the tip-sample distance is lowered as rationalized in the following.

Upon tip approach the growing van der Waals interaction between tip and graphene [103, 104] increases Γ_t, which enhances both tunneling channels. However, since $\Gamma_\sigma > \Gamma_\pi \quad \hbar$ the elastic channel is dominant and the ratio of inelastic to elastic currents decreases, and so does $\Delta g/g(0)$. The diminishing phonon signal intensity with tip-sample distance is, thus, included in Eqs. 3.1, 3.2 of the simple two-level model. As an additional effect, starting from the transition range the elastic deformation of graphene upon tip approach gradually induces a local symmetry breaking. As described above, the consequences are an enhanced elastic current into graphene and the contribution of many more phonon modes due to the lifted momentum conservation.[25, 105] The analysis of the current branching corroborates this aspect. Figure 3.5(e) depicts the contribution of the graphene terminal to the total conductance for increasing junction conductances. It shows, that the current flowing into the graphene terminal is indeed rapidly increasing at closer tip-sample separation.

3.1.4 Conclusions

In conclusion, strong graphene phonon signals induced by the intercalation of graphene on Ir(111) with Cs and Li were observed in IETS with an STM. The intensity of those signatures was tuned by the intercalant coverage as well as by the tip–surface separation ranging from tunneling to contact. Our experimental data laid the basis for developing a general picture of inelastic electron transport across graphene on surfaces. Model calculations based on a three-terminal setup show how the electronic (covalent) coupling of graphene σ and π-states with adjacent electrodes – tip and sample – regulates the current branching across the tunneling junction into elastic and inelastic transport channels. We anticipate the general applicability of the proposed model description to akin two-dimensional materials, which are in the focus of current research.

3.2 Local Phonon Probes and Alkali Metal Intercalation of Monolayer and Bilayer Graphene on Ru(0001)

Reproduced in part with permission from
Langmuir, 35(7): 2554–2560, 2019.
Copyright 2019 American Chemical Society.

Monolayer graphene (MLG) and bilayer graphene (BLG) on Ru(0001) have been studied by STM and spatially resolved IETS. The topographic data corroborate that the observed moiré patterns in BLG areas are induced by the interface of the strongly bound bottom graphene sheet and the metal surface. Signatures of graphene phonons are probed at different high-symmetry locations of the moiré unit cells of MLG and BLG. Spatial variations of the graphene–substrate and the graphene–graphene coupling manifest in the phonon signal intensity.

3.2.1 Introduction

The stacking of graphene layers has attracted considerable interest, primarily due to the strong dependence of the electronic structure on the twist angle between adjacent layers, which determines the interlayer coupling.[106] While chiral massive Dirac fermions occur in Bernal-stacked bilayer graphene, [107, 108] a finite twist between the graphene sheets gives rise to coexisting massive and massless Dirac fermions.[109] Moreover, the interlayer coupling yields unique characteristics in the BLG band structure like angle-dependent van Hove singularities [110, 111] and moiré bands [112, 113] that cause the Dirac velocity to oscillate with the twist angle and vanish at certain magic angles.[112]

Compared to the vastly investigated electronic structure of bilayer graphene, its lattice dynamics have been examined only in few theoretical [32, 33] and experimental works, mostly using Raman spectroscopy.[34–37] Recent IETS experiments on BLG/Ir(111) have reported phonon excitations in BLG but not MLG areas.[40] Site-specific BLG phonon excitations have remained virtually unexplored to date. There are, however, two reports on graphene phonon excitation at different moiré regions of a monolayer of graphene on Ru(0001) probed with IETS [38] and inelastic atom scattering.[39] The signal intensity variation of a different phonon with the moiré sites reported in reference [38] agrees well with our measurements on MLG. The observations on BLG can in part be explained by the simplified two-level model presented in the previous section.

3.2.2 Experimental Details

Sample preparation, STM and IETS measurements were performed as described in chapter 2. Tips were cut from high-purity Au wire.

3.2.3 Results and Discussion

Topography

Figure 3.6(a) shows an STM image of the prepared graphene on Ru(0001). BLG flakes typically extend over few 100 nm, often covering multiple terraces without discontinuity. They are usually attached to steps of the Ru(0001) surface, which act as nucleation sites for the segregation-based growth of graphene.[114–116] The top graphene sheet is continuous from MLG to BLG regions. Both domains exhibit well-ordered moiré superstructures with similar spatial periods of 3.02 ± 0.05 nm and 2.95 ± 0.06 nm, respectively [Fig. 3.6(b)]. This is in good agreement with previous reports.[86, 102, 117–120]

The pronounced buckling of 112 ± 4 pm in MLG regions reflects mainly the actual topography [10, 120, 121] and is caused by the strong hybridization of graphene π-states with Ru d-bands.[10, 118] High-symmetry stacking regions (on-top, hcp, fcc) of the moiré pattern are assigned based on their apparent height [10] and depicted in Fig. 3.6(c). The angle enclosed by the moiré and the atomic MLG lattice is $4.1^\circ \pm 1.0^\circ$. Consequently, the moiré analysis (section 2.4.1) yields a calculated twist angle of $0.37^\circ \pm 0.09^\circ$ between the MLG and Ru(0001) lattice, and a graphene lattice constant of 0.248 nm, which corresponds to 0.6 % tensile stress. Similar conclusions

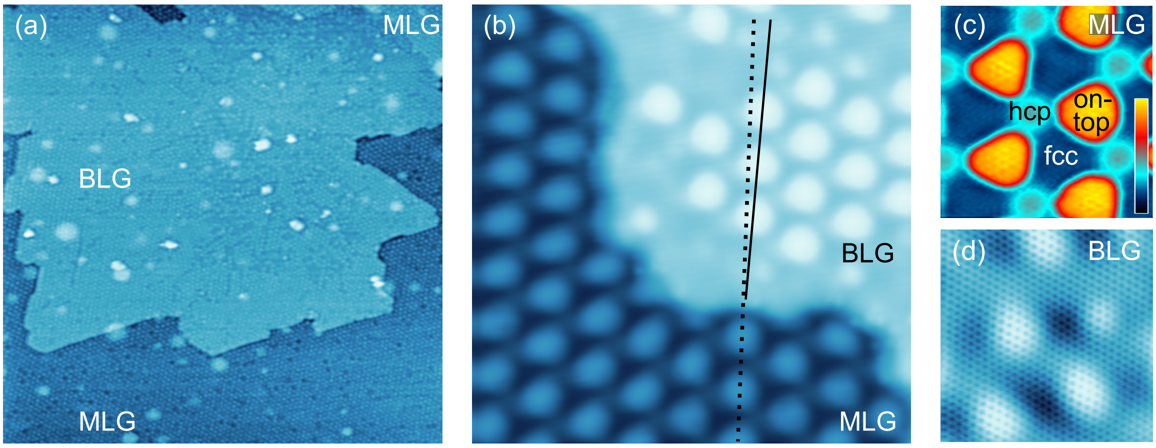

Figure 3.6: Atomic and moiré lattices of monolayer and bilayer graphene on Ru(0001). (a) STM image (300 mV, 100 pA, 233 × 233 nm^2) of Ru(0001) covered with MLG and BLG. (b) Close-up view (150 mV, 100 pA, 23 × 23 nm^2) of a BLG flake on MLG. The dashed (solid) line indicates the orientation of the MLG (BLG) moiré lattice, respectively. (c) Detailed view of the MLG moiré pattern (200 mV, 100 pA, 6.5 × 6.5 nm^2). High-symmetry sites (on-top, hcp, fcc) of the moiré pattern are labeled according to the position of the carbon hexagons regarding the Ru(0001) substrate. (d) Atomically resolved BLG (200 mV, 100 pA, 6.5 × 6.5 nm^2).

were drawn from earlier experiments and density functional calculations.[10, 86, 117, 119, 120, 122] On BLG flakes the moiré buckling is 119 ± 1 pm, which is similar to the corrugation of MLG and in accordance with previous work.[118, 119, 121, 122] The angle enclosed by the top graphene lattice [Fig. 3.6(d)] with the moiré pattern is $1.0° \pm 0.6°$, which corresponds to a lattice constant of 0.248 nm and a rotation angle of $0.33° \pm 0.08°$ with respect to Ru(0001) for the lower graphene layer (section 2.4.2, GSI). These values are very close to those obtained for MLG. This corroborates that the moiré pattern visible on the BLG flakes is most likely due to the strong hybridization at the graphene–Ru(0001) interface.[85, 86, 121] Furthermore, the structure of the segregated bottom graphene sheet in BLG is nearly identical with that of the MLG lattice. Minor rotational misalignments between these two appear enlarged in the resulting moiré patterns [83] as indicated in Fig. 3.6(b).

On BLG flakes some rather flat regions that do not exhibit a regular moiré superstructure occur [Fig. 3.6(b)].[118] The origin of these missing moiré domains has not been unveiled to date. However, since the top graphene layer is free of defects [Fig. 3.6(d)], the graphene–Ru(0001) interface is the obvious starting point for an explanation. Atomic defects in Ru(0001) or the bottom graphene lattice are sufficient to change the registry of layers and, thus, to suppress the characteristic moiré contrast. For instance, the frequently missing bright contrast in on-top regions of the MLG moiré pattern [dark spots in Fig. 3.6(a)] has been attributed to Ru(0001) surface vacancies with possible O incorporation.[123] Alternatively, the missing moiré domains in BLG may likewise be caused by carbidic surface structures [124] or imperfect carbon patches in the course of segregation leading to locally different stacking of the graphene layers.[119]

Previous studies indeed reported the formation of additional extended BLG domains characterized by a much lower moiré corrugation ($5 \pm 2\,\mathrm{pm}$ in [119]) and honeycomb contrast when elevated ethylene pressures were used in the preparation. These domains were attributed to AA-stacked graphene bilayers.[119, 120] On our sample other extended flat BLG flakes besides the comparably small missing moiré domains did not occur – probably due to the used ethylene partial pressure being two orders of magnitude lower. However, as characteristic for the reported AA-stacked BLG the top graphene sheets on the corrugated BLG flakes produced here exhibit a clear honeycomb lattice, too, indicating sublattice symmetry [Fig. 3.6(d)]. It appears, therefore, that a large/small corrugation alone is not sufficient to differentiate between Bernal (AB) and AA stacking, respectively. Furthermore, slightly different graphene orientations or minor strain always lead to BLG regions resembling AB or AA stacking locally. For instance, a continuous alternation of such stacking sites has been reported on strongly corrugated BLG/Ru(0001).[86]

Inelastic Electron Tunneling Spectroscopy

Figure 3.7(a) shows spatially resolved $\mathrm{d}^2I/\mathrm{d}V^2$ spectra from different high-symmetry sites of the MLG/Ru(0001) moiré lattice. The probing locations – on-top (red), hcp (yellow), and fcc (green) sites – are marked in Fig. 3.7(b). Signals of inelastic excitations occur as dip-peak pair in the hcp and fcc tunneling spectra and are absent at the on-top site. The inelastic features at $(\pm 47.2 \pm 1.5)\,\mathrm{mV}$ and $(\pm 68.3 \pm 1.0)\,\mathrm{mV}$ are assigned to, respectively, acoustic (ZA) and optical (ZO) out-of-plane phonon modes from the branches between M and K points of the Brillouin zone. In comparison to the data obtained on intercalated MLG/Ir(111) (ZA: $\pm 56\,\mathrm{mV}$, ZO: $\pm 75\,\mathrm{mV}$, section 3.1), both phonon energies are lowered by few meV. Such a downshift is characteristic for strongly bound graphene as was demonstrated for epitaxial MLG/Ni(111).[70] Especially the out-of-plane modes were shown to be affected by the formation of graphene-substrate bonds, which are present in MLG/Ru(0001) at the hcp and fcc sites.[10] As another consequence of the bonding to the substrate, the graphene sublattice symmetry is broken and the degeneracy of ZO and ZA branches at the K point is lifted.[70] The MLG topographic data [Fig. 3.6(c)] corroborates this aspect since the honeycomb contrast, which signals sublattice symmetry, is only resolved at the on-top sites of the moiré. Figure 3.7(c) shows a qualitative sketch based on the experimental observations, which depicts a plausible ZO and ZA band dispersion for the MLG/Ru(0001) hcp and fcc regions in comparison to the band dispersion of pristine graphene, which is assumed for the top graphene sheet of BLG as reasoned below.

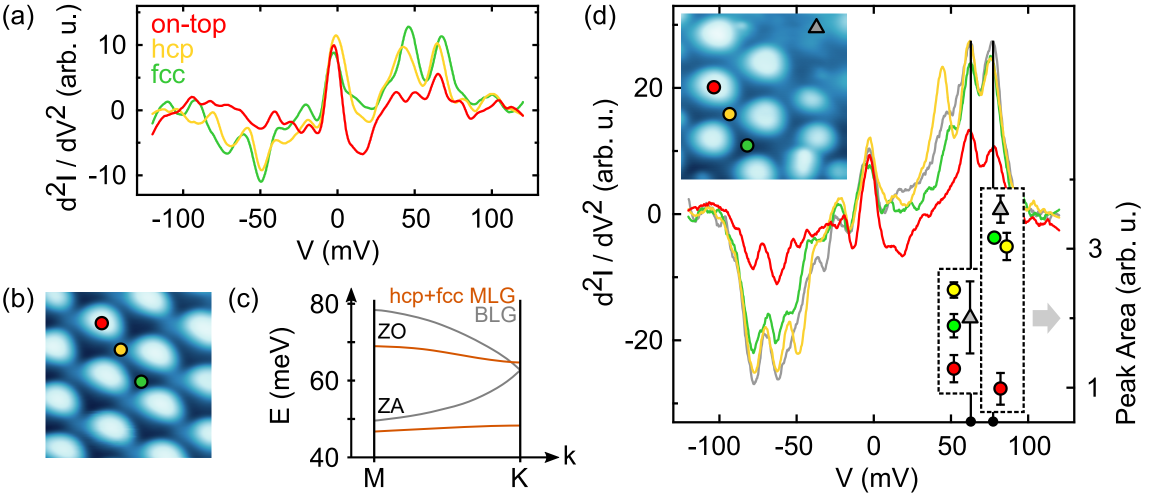

Figure 3.7: Spatially resolved IETS of monolayer and bilayer graphene on Ru(0001). (a) Spectra of $\mathrm{d}^2I/\mathrm{d}V^2$ recorded at the three moiré sites of MLG/Ru(0001). (b) STM image (120 mV, 100 pA, $9.3 \times 9.3\,\mathrm{nm}^2$) of MLG/Ru(0001) with marked IETS probing locations. (c) Sketch of the assumed optical (ZO) and acoustic (ZA) out-of-plane phonon dispersion of BLG (gray lines) and MLG/Ru(0001) at hcp and fcc sites (brown lines). The ZO and ZA dispersion branches at the hcp/fcc sites of MLG are subject to a lifting of the degeneracy at the K point of the Brillouin zone and an overall downshift, based on calculations of MLG/Ni(111).[70] (d) Spectra of $\mathrm{d}^2I/\mathrm{d}V^2$ recorded above the three moiré sites (color code as in (a)) and the missing moiré domain (gray) of BLG/Ru(0001). Peak areas for phonon modes at 62.1 mV and 77.5 mV are shown for comparison of the spatially varying signal strength. Inset: STM image (120 mV, 100 pA, $9.3 \times 9.3\,\mathrm{nm}^2$) with marked IETS probing locations.

Considering the two-level model developed in the previous section 3.1, the observation of phonon signatures in IETS on MLG/Ru(0001) is puzzling. Especially their occurrence only on the strongly bound fcc and hcp sites, but not on the comparably well decoupled on-top sites, [10] is unexpected. As pointed out above a hybridization of electronic states of graphene and substrate typically leads to the suppression of inelastic signals in IETS. While $\mathrm{d}^2I/\mathrm{d}V^2$ spectra are more sensitive to detect even faint inelastic signals, the latter have also been observed in the $\mathrm{d}I/\mathrm{d}V$. When averaged over fcc and hcp sites, the change in the differential conductance due to the phonon excitations amounts to $10\,\%$ for MLG on Ru(0001).[c]

A tentative explanation of the observation of these phonons in the framework of the previously introduced simplified two-level model may be an enhanced electron-phonon coupling (λ) at hcp and fcc sites of the moiré pattern, which could be reasoned as follows. Since the phonon bands are likely to exhibit a comparably flat dispersion between M and K compared to pristine graphene [70] as depicted in Fig. 3.7(c), a larger local phonon DOS at hcp and fcc sites is expected compared to the well decoupled on-top sites. In addition, the electronic π and π -bands at hcp and fcc sites are also downshifted and a band gap is opened.[11] This results in a shift of the π -band minimum just below the Fermi energy, which may provide an elevated electronic DOS at the Fermi level compared to the on-top sites, where the Dirac cone is intact and its center lies at $\approx 0.3\,\mathrm{eV}$.[11] With the vibrational DOS of the identified phonons and the electronic DOS at the Fermi level probably being higher at hcp and fcc sites compared to on-top sites, an enhanced electron-phonon coupling appears plausible.[25] Analogously, one contribution to the absence of phonon signatures on pristine MLG/Ir(111) (section 3.1 and [40]), where the electronic bands are only weakly perturbed, [79] may be a lower electron-phonon coupling.

Similar experimental observations have been made in a previous IETS study of graphene on Ru(0001), which reported an inelastic excitation at $360\,\mathrm{meV}$ due to an overtone excitation of a radial breathing mode.[38] The signal intensity of this vibration was largest in hcp sites of the moiré and lowest in on-top sites. While this was attributed to the spatial variation of the electron-phonon coupling, too, the explanation was based on the local symmetry in on-top sites hampering the excitation of the specific mode. Nevertheless, many other aspects may be relevant in the exact inelastic tunneling process due to the significantly altered electronic and vibrational bands of MLG/Ru(0001). For instance, the large curvature of graphene in the on-top sites could broaden potential phonon signatures and hinder their observation in IETS. Further experiments and transport calculations are still necessary to reach a conclusive explanation of the inelastic tunneling through strongly hybridized MLG and are currently in preparation.

Tunneling spectra recorded on BLG flakes exhibit three signatures of inelastic excitations [Fig. 3.7(d)]. The two features at $(\pm 77.5 \pm 0.2)\,\mathrm{mV}$ and $(\pm 62.1 \pm 0.2)\,\mathrm{mV}$ are compatible with phonon excitations from the ZO branch close to the M point of the Brillouin zone, and from the nearly degenerate ZO/ZA modes at K, respectively [Fig. 3.7(c)].[64] The ZO excitation occurs at higher energy compared to correspon-

---

[c] In comparison, the lowest Li coverage in MLG/Ir(111) yielded an increase of $17\,\%$ [Fig. 3.2].

ding MLG feature (68 meV) and is closer to the value expected for pristine graphene. This agrees with a previous experiment on BLG/Ir(111), where IETS features at (±77) mV and (±57) mV were attributed to the ZO and ZA branches close to the M point, respectively.[40] According to this interpretation, the top graphene sheet is well decoupled from the substrate, which leaves the phonon dispersion of largely unaltered and is in line with the intersection of ZO and ZA bands at ≈ 62 meV at K as for pristine graphene.[24, 64]

Both these inelastic signals are more pronounced on hcp (yellow) and fcc (green) stacking sites of the moiré pattern than in the on-top (red) regions as evident from the peak area[d] of the respective signatures [Fig. 3.7(d)]. Spectra recorded on missing moiré domains (gray) resemble those obtained from fcc sites indicating similar bonding. The difference in IETS signal strengths between on-top, hcp and fcc sites may be related to a spatial variation of the graphene–graphene coupling. The application of the previously introduced two-level model (section 3.1) to the IETS spectra of BLG/Ru(0001) suggests that the interlayer coupling depends on the moiré site. Lower signals in the on-top sites indicate a higher graphene–graphene coupling compared to the other regions of the moiré. The same conclusion has been reached from DFT calculations of BLG/Ru(0001).[121] At the on-top sites the bottom graphene is farthest from the metal substrate and closer to the upper graphene sheet, which is accompanied by an enhanced interlayer interaction. In hcp and fcc regions on the other hand the bottom graphene sheet hybridizes strongly with Ru(0001) and couples less with the upper graphene layer.[121]

The third dip-peak pair in the spectra occurs at $(\pm 50.9 \pm 0.8)$ mV on fcc sites and missing moiré domains, and at $(\pm 46.4 \pm 1.0)$ mV on hcp sites with slightly higher intensity. The energy of this inelastic excitation is similar to that of the ZA phonon branch of well decoupled graphene close to the M point [Fig. 3.7(c)].[64] Remarkably, this feature is absent at on-top sites, which could again be related to the locally enhanced interlayer coupling of the two graphene sheets. An alternative explanation could be the excitation of a graphene π-band plasmon similar to the graphite out-of-plane plasmon found in IETS [125] and high-resolution electron-energy-loss measurements.[126, 127] Its excitation energy depends on temperature and is ≈ 40 meV at 6 K for graphite.[125, 127] Although at the current stage a clear assignment of this spectral signature is not yet available, the obtained data provide a basis for the continuing experiments and calculations.

---

[d] Peak fits have been performed using Gaussian functions with a straight baseline.

3.2.4 Conclusions

Monolayer and bilayer graphene on Ru(0001) have been characterized by STM and IETS. Inelastic excitations of graphene out-of-plane phonons have been spatially resolved on different moiré sites. The varying signal intensity on the well decoupled upper graphene layer in BLG regions can be explained reasonably well within the earlier presented model (section 3.1) by local variations of the interlayer coupling. The observation of similar phonon features on the strongly hybridized MLG/Ru(0001) is remarkable as it contrasts the previous occurrence of such inelastic signatures mostly in quasi-free-standing graphene. A plausible origin is the significant alteration of electronic and vibrational bands at hcp and fcc moiré sites, which may give rise to a considerably elevated electron-phonon coupling.

4 Preparation of Bilayer Graphene on Pt(111) by Sequential Chemical Vapor Deposition

Reproduced in part with permission from
Phys. Chem. Chem. Phys., 21: 3140-3144, 2019.
Copyright 2019 Royal Society of Chemistry.

An inexpensive and flexible method is introduced that enables the epitaxial growth of bilayer graphene on Pt(111) by sequential chemical vapor deposition. First, a closed graphene monolayer is prepared by thermal decomposition of ethylene in a chemical vapor deposition (CVD) process. Next, the catalytically inactive graphene-covered sample surface is reactivated for a second CVD growth cycle through the deposition of several atomic layers of Pt. A final annealing process then leads to the diffusion of the buried first graphene sheet to the surface until bilayer stacking with the second sheet is accomplished. Scanning tunneling microscopy corroborates the successful growth of bilayer graphene (BLG) and elucidates the origin of moiré patterns depending on twist angles of the graphene sheets.

4.1 Introduction

The continuous interest in graphene and its derivatives is accompanied by a demand for reliable and scalable preparation methods to enable applications in industry and devices. Besides monolayer graphene, stacked systems such as bilayer graphene, whose properties depend strongly on stacking and interlayer twist angles, [109, 128] are in the focus of current research. High-quality graphene sheets are typically achieved by epitaxial growth on the desired substrate. SiC substrates [129–131] and transition metal surfaces [6, 132] have widely been used for the preparation of MLG as well as multilayer stacks.

Especially the thermal decomposition of hydrocarbons assisted by catalytically active transition metal surfaces is a reliable method for the fabrication of single layer graphene. It is typically performed as a chemical vapor deposition on the hot sample [133] and yields high-quality sheets with only few rotational domains depending on substrate and growth temperature.[6, 134, 135] Due to its simplicity, this preparation method may readily be applied in industrial production.[7] As the growth relies on the catalytic effect of the metal surface, it is self-limiting to one monolayer. On the one hand, this enables precise thickness control for monolayer growth. On the other hand, the growth of graphene bilayers and multilayers is prevented. For the latter, an alternative approach, namely the segregation of C at elevated temperatures, is applied frequently. To this end, the bulk metal is artificially enriched with C, either via doping from the gas phase of hydrocarbons [6, 78, 85, 114, 132, 136] or solid-state diffusion.[137–140] After the preparation of graphene on Pt(111) using this technique, occasional domains of few-layer graphene have been observed previously.[78] However, the multilayer growth occurred only at grain boundaries and the number of prepared layers was largely uncontrollable. Alternatively, high-quality multilayer graphene on metals may also be achieved by intercalation of C under MLG but requires sources of atomic carbon.[40, 141, 142] Ideally, a CVD-based layer-by-layer preparation would be desirable, as it could combine the synthesis of large-scale graphene sheets with high structural quality and precise thickness control owing to the self-limitation to one monolayer per growth cycle.

Here, an approach based on sequential CVD cycles is presented that achieves the preparation of extended BLG regions on Pt(111). All prepared graphene layers are thoroughly characterized by atomically resolved scanning tunneling microscopy. A method similar to one step of the proposed procedure has recently been applied to prepare MLG flakes on Au(111).[143] Since Au does not offer the convenient CVD synthesis, MLG flakes grown by CVD on Ir(111) were subsequently intercalated by several monolayers of Au yielding graphene flakes on top of a Au(111) surface.

4.2 Experimental Details

The preparation of the Pt(111) surface and Au tips was performed as described in section 2.2. After MLG growth via thermal decomposition of C_2H_4 at 1200 K, additional Pt was evaporated from a hot filament at a rate of $\approx 1\,\mathrm{ML/min}$ (ML: dense-packed monolayer), which was calibrated from STM images of several independent depositions on Au(100) and MLG/Pt(111). The preparation of the second graphene layer was performed by annealing the sample at 1000 K for 3 min, directly followed by exposure to C_2H_4 for 4 min. The sample was kept at 1000 K for another 5 min before cooling to room temperature. Subsequent annealing cycles were performed at 1200 K.

The Ir(111) surface in the preliminary experiments was prepared as described in section 2.2. Flake growth was achieved by reducing exposure time and partial pressure of ethylene ($6 \quad 10^{-6}$ Pa for 2 min) in the CVD. Ir was evaporated from an Ir rod mounted in an electron beam evaporator.

4.3 Results and Discussion

Preliminary Experiments

The concept of reactivating the sample surface for graphene CVD by depositing additional substrate material on top of the first layer may seem an intuitive approach. However, all steps after the MLG growth are accompanied by challenges of experimental or physical nature. The proposed preparation protocol was developed based on preliminary experiments with Ir(111) (Fig. 4.1) and Pt(111) (Fig. 4.2), which are briefly described in the following to emphasize critical points in the process.

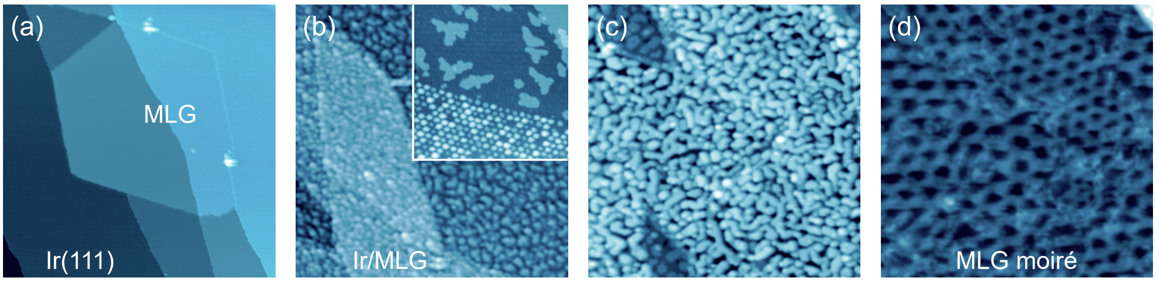

Figure 4.1: Preliminary BLG growth experiments on Ir(111). (a) STM image of MLG flakes on Ir(111) (160 mV, 100 pA, $250\times250\,\mathrm{nm}^2$). (b) STM image of the sample in (a) after deposition of 4 ML Ir over 120 min (150 mV, 100 pA, $200\times200\,\mathrm{nm}^2$). Inset: Lower Ir coverage (0.25 ML) yields a regular Ir cluster array on graphene-covered areas (lower half) and flat Ir islands on pristine Ir(111) (upper half).[73] (c) STM image of slightly smoothed Ir layer after annealing at 1000 K. (130 mV, 100 pA, $200 \times 200\,\mathrm{nm}^2$). (d) Moiré patterns of the inhomogeneous graphene monolayer after the second layer growth attempt with TPG. (80 mV, 120 pA, $30 \times 30\,\mathrm{nm}^2$).

On Ir(111) MLG flakes were prepared [Fig. 4.1(a)] aiming for BLG flakes in the final stage. The subsequent deposition of Ir at a rate of approximately 0.03 ML/min yielded a regular array of Ir clusters adsorbed to the hcp sites of the moiré pattern at lower coverage [73] and flat Ir islands on the pristine Ir(111) surface [inset to Fig. 4.1(b)]. In order to provide a suitably flat template for the growth of homogeneous graphene the deposited Ir was then smoothed by annealing. Figure 4.1(c) shows the slightly flattened Ir after a short annealing to 1000 K. However, during any additional annealing – either intended as separate step for further smoothing or during the temperature ramp-up for the second layer CVD – the adsorbed Ir quickly intercalated beneath the graphene sheet or simply diffused to the uncovered Ir substrate. Thus, all attempts at a second layer CVD failed, leaving behind only MLG flakes on Ir(111). This is a general issue, which also occurred in the Pt experiments as shown in (Fig. 4.2) although a closed monolayer of graphene was used instead of flakes. Since heating the sample is a necessity for the second layer CVD, two possible solutions were tested to prevent the concomitant completion of metal intercalation.

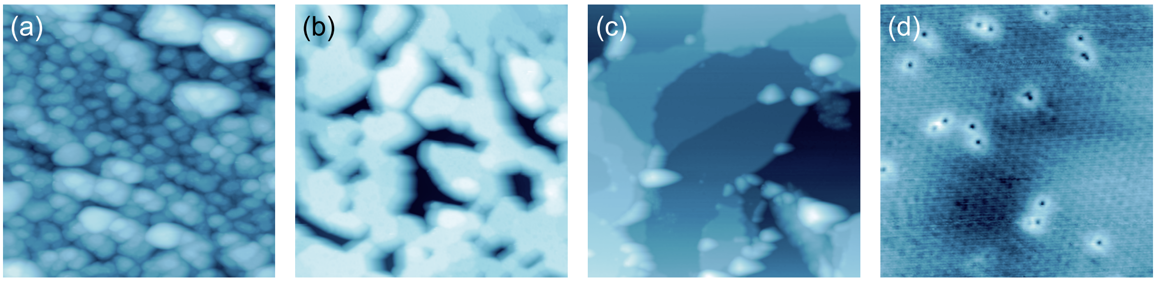

Figure 4.2: Pt intercalation of MLG-covered Pt(111). (a) STM image of Pt film deposited on MLG/Pt(111) (1 V, 80 pA, 120 × 120 nm^2). (b) STM image of the deposited Pt smoothed by annealing at 720 K (1.5 V, 80 pA, 150 × 150 nm^2). (c) STM image of MLG/Pt(111) after complete intercalation of the deposited Pt through further annealing at 1200 K (1.5 V, 80 pA, 100 × 100 nm^2). (d) MLG moiré pattern observed on the sample shown in (c) (0.1 V, 100 pA, 20 × 20 nm^2).

The first approach was to avoid the initial heating in CVD by performing the second layer preparation as temperature programmed growth (TPG) instead.[133] Here, ethylene was adsorbed first on the slightly smoothed metal layer. Subsequent annealing then initiated the graphene growth. As Fig. 4.1(d) shows, this resulted, however, in a very inhomogeneous graphene monolayer consisting of many small graphene domains of different orientations as seen in the variety of moiré patterns. No BLG domains were observed on that sample. Since activation temperatures for intercalation (typically several 100 K) are lower than the temperature required for the graphene synthesis, the most likely explanation is that even this method cannot prevent the complete metal intercalation during the temperature ramp-up. Furthermore, these first insights lead to the conclusion that sufficient smoothing of the adsorbed metal layer is required in any case. This is facilitated by the second solution as described in the following.

The second approach was to simply deposit a larger amount of metal in order to delay its intercalation. Due the low yield of Ir [120 min deposition time for a coverage of 4 ML in Fig. 4.1(b)] with the evaporation from a rod, Pt was chosen as alternative material and evaporated from a hot filament onto MLG/Pt(111).[144] While in principle the presented preparation protocol should be applicable to many other transition metals like Ru, Ni, etc.,[6, 132] Pt(111) has the benefit that the segregation after a standard CVD process is typically insufficient to already produce BLG, avoiding misinterpretations. Moreover, graphene on Pt(111) has the appealing property of the lowest graphene–metal coupling.[8] Preferably, evaporation from a melt in the EBE should be used and is currently prepared at the vacuum chamber. Figure 4.2(b) demonstrates that a thick layer of Pt can indeed be smoothed well without complete intercalation.

Based on these preliminary experiments, the successful growth of BLG was achieved by depositing ≈ 50 atomic layers of Pt on a closed monolayer of graphene, utilizing a slightly prolonged temperature ramp for the second layer CVD directly as smoothing stage, and performing the CVD at comparably low temperature (1000 K). The full preparation protocol is described in the next paragraph.

Preparation Protocol

Figure 4.3 illustrates the BLG preparation process by STM images [Figs. 4.3(a-d)] and sketches [Figs. 4.3(e-h)]. First, MLG is grown epitaxially by CVD of C_2H_4 at the Pt(111) surface Figure [Figs. 4.3(a,e)]. In most regions of the sample, moiré patterns due to the lattice mismatch between graphene and Pt(111) were absent in STM images, which hints at large rotation angles of graphene with respect to Pt(111).[75, 144] The occasionally observed moiré superstructures usually indicated smaller rotation angles ($< 20°$).[9] Second, approximately 50 atomic layers of Pt were deposited on MLG-covered Pt(111). STM images show resulting Pt clusters [Figs. 4.3(b,f)]. The third step included a few minutes long temperature ramp for smoothing of the deposited Pt layer and the second CVD cycle at 1000 K. The elevated temperature of the sample led to the intercalation of Pt accompanied by the diffusion of most of the metal-covered graphene to the surface giving rise to large MLG and many small BLG regions [Figs. 4.3(c,g)]. During this process, the buried MLG is likely broken apart into patches. Indeed, graphene domain boundaries represent typical entry points for intercalation [14, 15] and may likewise facilitate the rupture of MLG.[145] Individual patches can then diffuse separately to the surface as observed during the

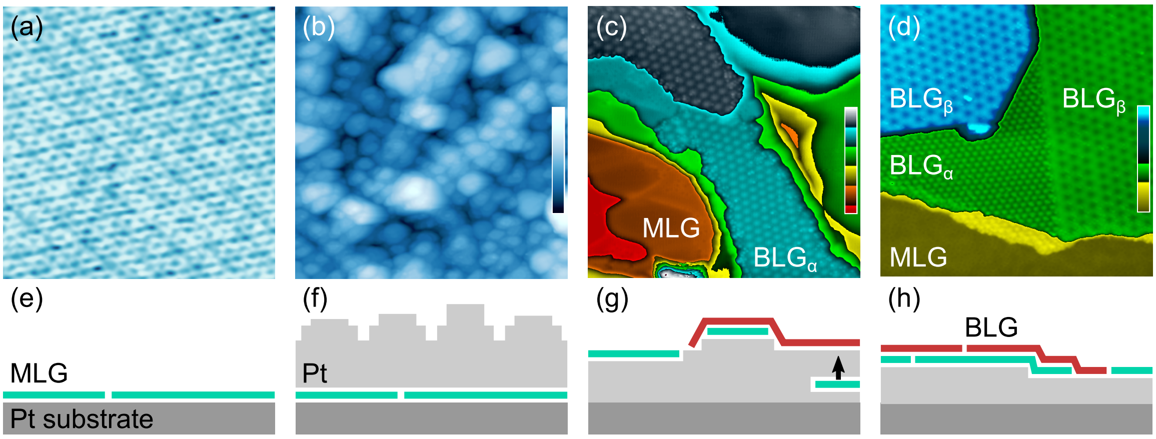

Figure 4.3: Steps of the BLG preparation protocol. (a) Atomically resolved STM image of MLG on Pt(111) (bias voltage: $V = 74\,\text{mV}$, tunneling current: $I = 100\,\text{pA}$, size: $5 \times 5\,\text{nm}^2$). (b) STM image of Pt film deposited on MLG/Pt(111) (1 V, 80 pA, $120 \times 120\,\text{nm}^2$). (c) STM image of MLG and BLG regions after the second CVD step (1 V, 80 pA, $40 \times 40\,\text{nm}^2$). (d) STM image of MLG and BLG after annealing the sample of (c) (1 V, 90 pA, $60 \times 60\,\text{nm}^2$). The color bars indicate the apparent heights ranging from 0 nm (bottom) to (b) 7.1 nm, (c) 1.6 nm, (d) 1.3 nm (top). (e)–(h) Illustrations (cross-section) of the preparation steps. Graphene layers grown in the first (second) CVD cycle are drawn as green (red) lines, respectively.

preparation of graphene nanoflakes on Au(111)/Ir(111).[143] Additionally, due to the higher carbon solubility of Pt, [146] single C atoms may detach from the boundary of buried graphene layers, segregate and contribute to the graphene growth at open edges.[137–140] However, the nucleation of additional graphene layers at the regular MLG–Pt(111) interface by individually segregating C atoms alone is reportedly suppressed, [78] which corroborates the suggested growth mechanism based on the diffusion of graphene patches. Final annealing of the sample yielded flat and extended MLG and BLG regions [Figs. 4.3(d,h)]. At elevated temperature, second-layer graphene flakes hybridize to form extended BLG regions, while buried graphene patches continue their diffusion to the surface and may either be incorporated in the bottom graphene layer or create additional BLG or even trilayer graphene (TLG) regions.

Moiré Patterns

The proposed growth is corroborated by the analysis[a] of spatial moiré periods (a_m) plus the orientations of the moiré pattern (σ) and of the observed graphene lattice (θ) with respect to Pt(111). Various moiré patterns observed after the first layer growth

---

[a] Details of the analysis are summarized in section 2.4.

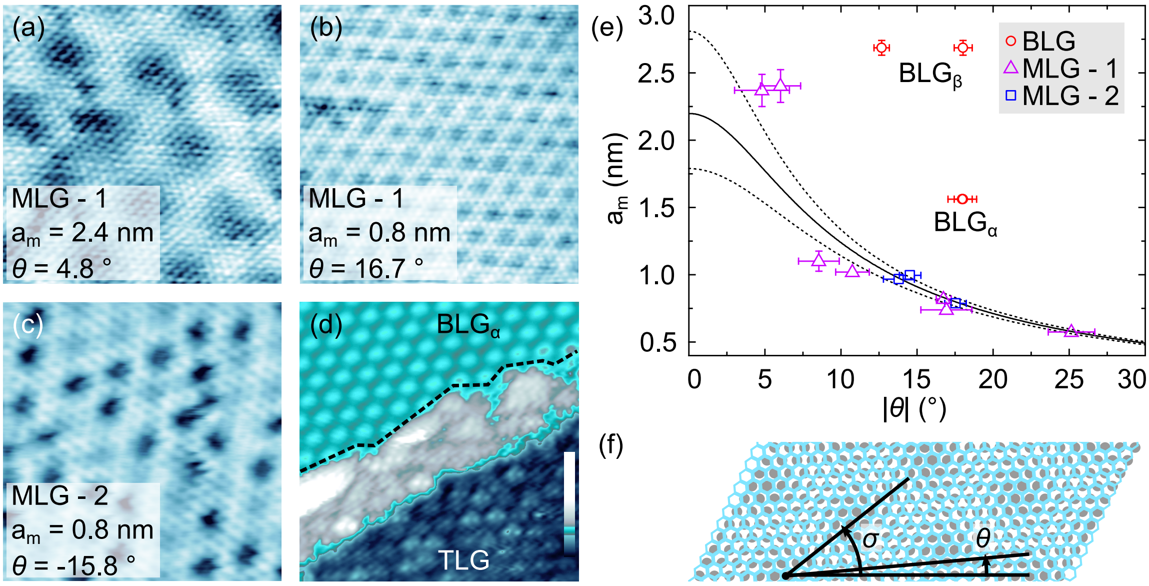

Figure 4.4: Overview and analysis of observed graphene domains on Pt(111) with indicated moiré spatial period (a_m) and graphene orientation (θ). STM images of MLG domains with (a) $a_\mathrm{m} = 2.4\,\mathrm{nm}$, $\theta = 4.8°$ ($100\,\mathrm{mV}$, $100\,\mathrm{pA}$, $8 \times 8\,\mathrm{nm}^2$) and (b) $a_\mathrm{m} = 0.8\,\mathrm{nm}$, $\theta = 16.7°$ ($39\,\mathrm{mV}$, $9\,\mathrm{nA}$, $8 \times 8\,\mathrm{nm}^2$). (c) MLG domain after the final annealing step with $a_\mathrm{m} = 0.8\,\mathrm{nm}$, $\theta = -15.8°$ ($50\,\mathrm{mV}$, $100\,\mathrm{nA}$, $5 \times 5\,\mathrm{nm}^2$). The dark depressions are attributed to C atoms or vacancies in the Pt surface. (d) Adjacent BLG and TLG domains ($400\,\mathrm{mV}$, $100\,\mathrm{pA}$, $20 \times 20\,\mathrm{nm}^2$). The TLG crosses a substrate step edge and ends approximately at the boundary marked by the dashed line. (e) Summary of a_m, θ for all observed moiré structures in MLG and BLG. The solid line depicts the expected variation of a_m with θ for unstrained MLG. The upper (lower) dashed curve depicts a_m as a function of θ for MLG with lattice constant increased (decreased) by 2 %. Open triangles (squares) are data for MLG after the first (second) CVD process, denoted as MLG-1 (MLG-2). Circles represent data for two BLG domains, BLG$_\alpha$ and BLG$_\beta$ (see text). (f) Sketch of MLG/Pt(111). Solid lines mark crystallographic directions of Pt(111) (dots), graphene (circles) and the resulting moiré superlattice. The orientations of graphene (θ) and moiré lattice (σ) with respect to Pt(111) are indicated.

and after completed preparation are taken into account (Fig. 4.4). The measured characteristics are compared to the expected trends of MLG on Pt(111) [Fig. 4.4(e)]. Graphene prepared in the first layer growth occasionally exhibits moiré patterns with, e.g., $a_\mathrm{m} = 2.37\,\mathrm{nm}$, $\theta = 4.8°$ [Fig. 4.4(a)] or $a_\mathrm{m} = 0.82\,\mathrm{nm}$, $\theta = 16.7°$ [Fig. 4.4(b)]. The domain with $a_\mathrm{m} = 0.79\,\mathrm{nm}$ and $\theta = -15.8°$ shown in [Fig. 4.4(c)] occurred after completed preparation. The dark depressions may be due to C atoms in the Pt surface [140] or vacancies.[147] These and several other domains are reasonably well described by the MLG/Pt(111) model [Fig. 4.4(e)]. Dashed lines depict a_m as a function of θ for a stretched (upper curve) and compressed (lower curve) C lattice, where the lattice constant deviates by 2 % from the unstrained case. Deviations up to 7 % were reported for stable configurations of MLG on Pt(111).[9]

Some data, however, deviate significantly from the predicted trend. That is, in a MLG model the measured moiré spatial period is not compatible with the observed graphene orientation θ. The corresponding domains are only found after the second CVD process and are, therefore, assigned to BLG. They exhibit two different types of moiré patterns. The BLG$_\alpha$ moiré pattern has a spatial period of $a_\mathrm{m} = 1.6\,\mathrm{nm}$ and the angle between moiré pattern and Pt(111) orientation is $\sigma = -28.8°$. BLG$_\beta$ is characterized by $a_\mathrm{m} = 2.7\,\mathrm{nm}$ and $\sigma = 0.8°$. Figure 4.4(d) shows a region, where BLG$_\alpha$ and TLG are present as adjacent regions. The dashed line marks the boundary between the different domains. Further evidence for this assignment is provided in the gallery of STM images in Fig. 4.5.

Figure 4.5(a) depicts an overview of an extended BLG region that contains both moiré patterns, BLG$_\alpha$ and BLG$_\beta$. Unexpectedly, each of them exhibits two subdomains, i.e., BLG areas of identical moiré pattern (identical a_m and σ) but different top graphene orientation θ_t regarding the Pt substrate. This is demonstrated exemplarily in Figs. 4.5(b,c) for the BLG$_\alpha$ domain with atomic resolution. Fourier transforms [insets to Figs. 4.5(b,c)] reveal that the graphene lattices of the subdomains are rotated by 36° with respect to each other, while the BLG$_\alpha$ moiré pattern is unaffected. These observations demonstrate the presence of two stacked graphene sheets in BLG$_\alpha$ and BLG$_\beta$ domains.[b]

Remarkably, when the subdomains of BLG$_\alpha$ and BLG$_\beta$ with $\theta_\mathrm{t} = 18°$ connect, there can be a continuous top graphene lattice covering both moiré patterns. This is shown in the close-up view of the domain boundary between BLG$_\alpha$ and BLG$_\beta$ in Fig. 4.5(d). In conclusion, the different moiré patterns must be due to rotational domains of the bottom graphene sheet. Additional information is gained from the inspection of line defects in the top graphene sheet [Fig. 4.5(e)]. The STM image reveals that the BLG$_\alpha$ moiré pattern remains unaffected across the defect as evidenced by the superimposed lattice. Therefore, the observed moiré superstructure is due to the graphene–Pt(111) interface and, intriguingly, the upper graphene layer does not contribute to the moiré pattern.

So far, the experimental data have led to the conclusions that the moiré domains deviating from the MLG characteristics are indeed caused by BLG. However, the

---

[b] If the observed domains were just MLG/Pt(111), the moiré pattern would be altered when the graphene sheet is rotated. (section 2.4.1)

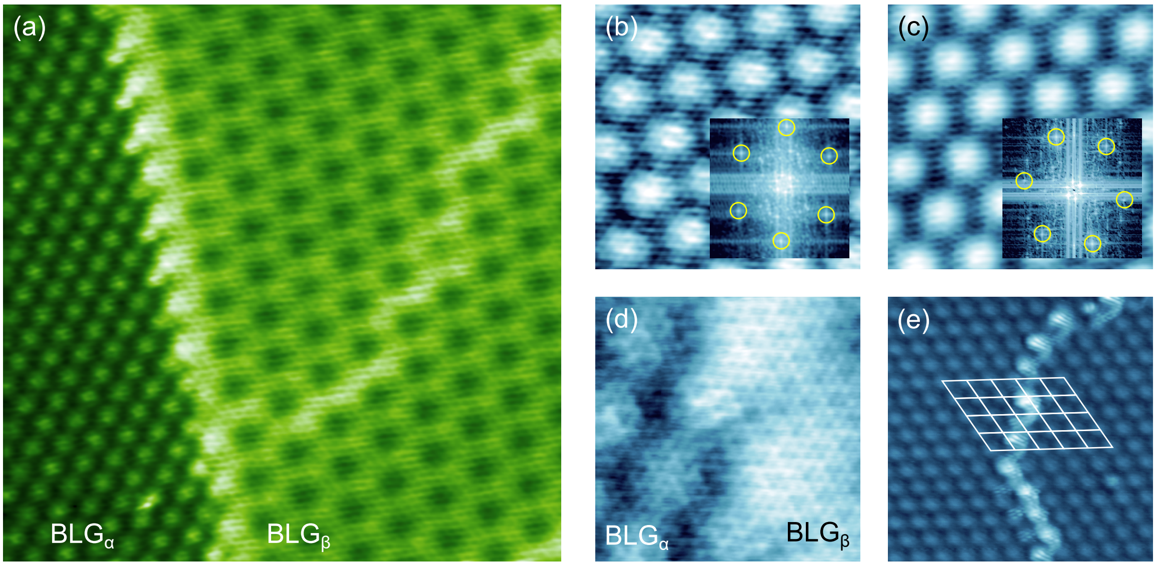

Figure 4.5: Graphene bilayer domains. (a) Overview STM image showing adjacent BLG$_\alpha$ and BLG$_\beta$ domains (70 mV, 100 pA, $30 \times 30\,\text{nm}^2$). (b), (c) STM images (50 mV, $7 \times 7\,\text{nm}^2$) of BLG$_\alpha$ subdomains with identical moiré characteristics ($a_\text{m} = 1.6\,\text{nm}$, $\sigma = -28.8°$) and different graphene orientations, (b) $\theta = 18.0°$ and (c) $\theta = -18.0°$. Tunneling currents are 100 nA (b) and 10 nA (c). Insets: Fourier transforms of STM images with circles indicating the graphene lattice orientation. (d) Atomically resolved STM image of the transition from the BLG$_\alpha$ ($a_\text{m} = 1.6\,\text{nm}$, $\theta = 18.0°$, left) to the BLG$_\beta$ moiré superlattice ($a_\text{m} = 2.7\,\text{nm}$, $\theta = 18.0°$, right) (70 mV, 100 pA, $5 \times 5\,\text{nm}^2$). (e) STM image of BLG$_\alpha$ with a line defect in the top graphene layer (1 V, 80 pA, $20 \times 20\,\text{nm}^2$). The superimposed lattice shows that the moiré pattern is continuous across the line defect.

corresponding moiré patterns are apparently due to differently oriented lower graphene sheets interacting with the Pt(111) surface, while the top graphene layers do not cause any obvious moiré patterns. In contrast, moiré lattices of BLG/Ir(111) were previously attributed to the graphene–graphene interface.[40] The apparent contradiction with findings reported here is resolved when twist angles at *both* the graphene–substrate *and* graphene–graphene interfaces are considered. For both interfaces, low twist angles ($< 10°$) result in an elevated interaction, while large twist angles ($> 10°$) decouple the adjacent layers.[40, 106, 148, 149] Consequently, the twist angles at both interfaces and the resulting interlayer coupling determine which moiré superstructure is visible in STM images.

Figure 4.6 shows a comparison between BLG domains reported here and from BLG/Ir(111) [40] with the expected moiré characteristics of twisted BLG (section 2.4.2). The moiré spatial period is plotted over the experimentally accessible angle between the top graphene sheet and the moiré lattice. For BLG/Ir(111), the second

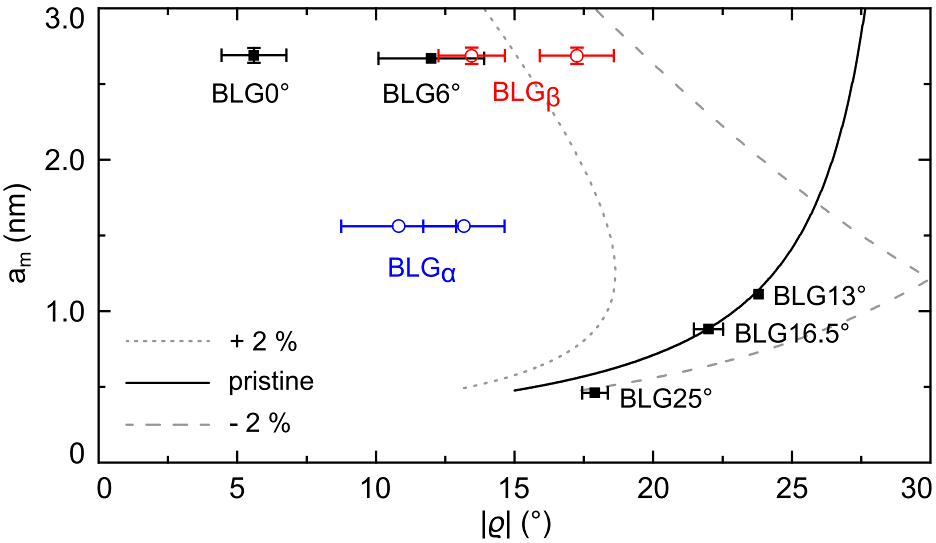

Figure 4.6: Twisted bilayer graphene (BLG) model. Lines depict the calculated moiré spatial period a_m as a function of the angle enclosed by crystallographic directions of the upper graphene lattice and the moiré superstructure. The solid line shows the variation of a_m with | | for an unstrained lower graphene sheet, whereas short-dashed and long-dashed lines represent the situation for a graphene lattice constant that is increased and decreased by 2 %, respectively. Experimental data appear as circles (this work) and squares (BLG/Ir(111) [40]). The angles 0° . . . 25° denote the twist angles between the bottom and upper graphene sheets.

layer flakes were produced by intercalation of C under MLG that is aligned with the Ir(111) substrate.[40] The twist angles at both interfaces can, thus, be considered roughly equivalent. Remarkably, only the data for larger twist angles (> 13°) follow the calculated trend reasonably well, but there is a notable deviation at smaller rotation angles. Indeed, the characteristics of the BLG0° and the aligned-MLG moiré superstructures on Ir(111) were found to be virtually identical.[40] Thus, the alignment of the lower graphene lattice in the BLG0° domain with the Ir substrate and the resulting enhanced hybridization seem to enable the observation of the graphene–substrate moiré pattern. Instead, the graphene–graphene moiré lattice is observed at larger twist angles, where the bottom graphene is well decoupled from the Ir substrate.

In the BLG$_\alpha$ and BLG$_\beta$ domains reported here the bottom graphene layers are rotated by only 4.6° and 0.1° with respect to the Pt(111) surface, respectively. Concomitantly, all graphene–graphene twist angles exceed 10°. This constellation yields a comparably low (elevated) coupling between the two graphene sheets (substrate and bottom graphene sheet), respectively. Consequently, the observation of the moiré pattern generated by the graphene–substrate interface is clearly favored.

It is worth mentioning that, in principle, all BLG moiré patterns observed here can be interpreted in the framework of twisted BLG, too (section 2.4.2). While the BLG$_\alpha$ subdomains [Figs. 4.5(b,c)] would then require comparably large strains of 3.5 % and 4.2 % in the lower graphene sheet to match the observed characteristics of the moiré pattern, the BLG$_\beta$ subdomains would exhibit merely 1.6 % and 2.3 % strain. However, for each pair of subdomains the resulting moiré patterns would have to align to reproduce the experimental observations. That is because only a single moiré orientation occurred for the BLG$_\alpha$ and BLG$_\beta$ patterns, respectively. Therefore, the twisted-BLG explanation is unlikely and not appropriate to describe the observed moiré structures.

4.4 Conclusions

A preparation protocol for the preparation of extended BLG on Pt(111) has been developed. It is based on CVD growth cycles with intermediate reactivation of the sample surface by Pt deposition. Due to its simple concept and the precise control over the number of prepared graphene layers, its applicability to other transition metal substrates and homogeneous as well as heterogeneous multistackings of graphene and other two-dimensional materials may be anticipated. The presented topographic data unveil that the moiré superlattices observed in BLG regions result from the graphene–Pt(111) interface. The top graphene layer on the other hand is well decoupled due to larger twist angles.

5 Intercalant Assemblies at the Graphene Metal Interface

Reproduced in part with permission from
Langmuir, 35(7): 2554–2560, 2019.

The impact of graphene on the structure of metal intercalants is studied from STM topographic data. In the first section of this chapter, a surface reconstruction induced by the intercalation of Pt under monolayer graphene (MLG) on Pt(111) is presented. The observed pattern is qualitatively different from the reconstructions induced by the deposition of metals on Pt(111) and, specifically, the homoepitaxy of Pt. Moreover, graphene on Ru(0001) has been successfully cointercalated with Cs and Li. The intercalants form separate phases. Their respective atomic superstructures are determined based on atomically resolved STM characterization. Cs arranges in (2×2) and Li in (1×1) superstructure with respect to graphene.

5.1 Introduction

The formation of superstructures at surfaces is an omnipresent phenomenon.[42, 43] Ordered assemblies of adsorbates, moiré patterns of layered systems, and surface reconstructions are only few prominent examples of patterns that are observed regularly. In the case of adsorbates, superlattices form as the result of the adsorbate–adsorbate and adsorbate–substrate interactions. Analogously, intralayer and interlayer interactions determine the appearance of superstructures of layered materials. Depending on the dominating interaction different specific patterns occur. For instance, a strong adsorbate–adsorbate coupling between adsorbed molecules manifests in characteristic overlayer structures, [150–152] while a strong adsorbate–substrate interaction often mediates template effects of the substrate as in the guided adsorption on molecular platforms [153] or on moiré lattices.[73, 154–175]

The addition of a graphene cover layer introduces another contribution to the balance of relevant interactions, which may affect existing patterns depending on the specific system. In this chapter the impact of graphene on superstructures of different intercalants is explored at the examples of Pt intercalation under graphene on Pt(111), and the intercalation of Cs and Li under graphene on Ru(0001).

5.2 Experimental Details

Preparation of clean Ru(0001) and Pt(111) surfaces was performed as described in section 2.2.2. Tips were cut from high-purity Au wire. The growth of BLG and MLG on Pt(111) has been described in chapter 4. The cointercalation of graphene on Ru(0001) with Cs and Li was achieved by the deposition of Li onto Cs-intercalated graphene followed by post-annealing.

5.3 Results and Discussion

Pt Surface Reconstruction

Besides the moiré patterns of graphene described in the previous chapter 4, parts of the Pt(111) sample surface were covered by a wide-meshed honeycomb superstructure that extended over a few hundred nanometers [Fig. 5.1(a)]. Based on the description of similar patterns on Pt(111) in previous reports [176–179] this superstructure is assigned to a reconstruction of the Pt(111) surface, which is related to the soliton reconstruction of Au(111).[180–183]

It was shown in 1992 that annealing pristine Pt(111) at temperatures exceeding 1330 K gives rise to a hexagonal reconstruction of the surface.[176, 177] Shortly thereafter a similar superstructure was stabilized already at 400 K by exposure of the heated Pt(111) surface to Pt vapor.[178, 179] Similar reconstructions have been induced by deposition of Co, [184] Cr, [185] or Cu [186] on Pt(111). Recent calculations [187] based on a Frenkel-Kontorova model [188] have demonstrated that those reconstructions of Pt(111) are indeed all different manifestations of one type of reconstruction, which may be triggered already by small environmental changes. In contrast to the rather irregular network of double lines observed after homoepitaxial growth of Pt on clean Pt(111) at 400 K, [178, 179] the presence of graphene induces an extended long-range order of the reconstruction as well as a qualitative change in the underlying dislocation network. Common characteristic features of all these su-

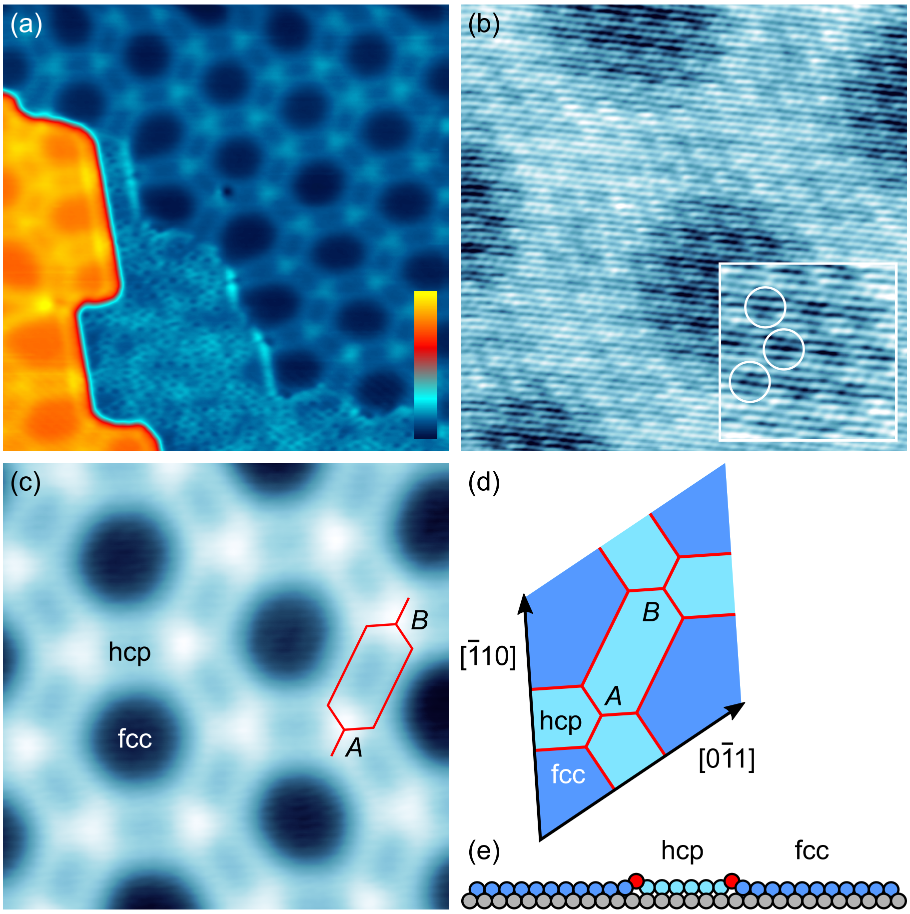

Figure 5.1: Reconstruction of graphene-covered Pt(111) after Pt intercalation. (a) STM image of Pt-intercalated graphene on Pt(111) (1 V, 100 pA, $40 \times 40\,\mathrm{nm}^2$). Two adjacent Pt(111) terraces are visible. The honeycomb network is due to a reconstruction of the Pt(111) surface. The apparent height ranges from 0 pm (dark blue) to 265 pm (yellow). (b) Atomically resolved close-up view of (a) showing the graphene lattice on top of the reconstruction (50 mV, 100 pA, $12 \times 12\,\mathrm{nm}^2$). Inset: Close-up view of (b) with circles indicating a MLG moiré pattern ($3.5 \times 3.5\,\mathrm{nm}^2$). (c) STM image of the Pt(111) reconstruction network showing the characteristic fcc and hcp stacking domains. (1 V, 100 pA, $19 \times 19\,\mathrm{nm}^2$). The triangle-shaped bright protrusions are the connectors of the network (see text). (d) Illustration of structural elements of the reconstruction network. Regions with hcp stacking are separated from fcc domains by Shockley partial dislocations (bright lines) that are oriented along [112], [121], [211] directions. The double lines meet at inequivalent junctions *A* and *B*. (e) Side view of first and second Pt(111) atomic layer along 110 . 30 surface Pt atoms reside atop 29 second-layer Pt atoms.

perstructures are neighboring domains of face-centered cubic (fcc) stacking retained from the Pt bulk and hexagonal close-packed (hcp) stacking regions. In the following, conventional phrasing is used to describe certain structural features of the pattern. In particular, the protruding parallel ridges separating the differently stacked domains will be referred to as double lines.[178, 179]

Before analyzing the reconstruction, some remarks regarding the observed graphene moiré patterns are noteworthy. First, atomically resolved STM imaging [Fig. 5.1(b)] evidences the presence of graphene on top of the reconstructed surface. The inset to Fig. 5.1(b) reveals a moiré pattern with a spatial period of $a_\mathrm{m} = 1.00 \pm 0.02\,\mathrm{nm}$, a graphene orientation of $\theta = 14.5^\circ \pm 0.7^\circ$ with respect to the Pt substrate, and an angle of $= 1.2^\circ \pm 1.1^\circ$ between moiré and graphene lattice. This pattern is well-described by a single layer of graphene on Pt(111) [Fig. 4.4(e)].[9, 75] Second, a very similar moiré pattern ($a_\mathrm{m} = 0.97 \pm 0.01\,\mathrm{nm}, \theta = 13.8^\circ \pm 1.0^\circ, \quad = 5.8^\circ \pm 0.8^\circ$) occurred on unreconstructed areas, which corroborates the expectation that there are continuous MLG sheets covering unreconstructed and reconstructed areas of the sample.

The topographic image in Fig. 5.1(c) presents the reconstruction pattern in detail. It is characterized by a large spatial period of $7.99 \pm 0.08\,\mathrm{nm}$ and parallel ridges separated by $1.98 \pm 0.10\,\mathrm{nm}$. Its structural elements are illustrated in Fig. 5.1(d) together with the crystallographic directions. Bright double lines are formed by a pair of Shockley partial dislocations that separate hexagonal fcc-stacked from smaller elongated hcp-stacked regions.[178, 179] Across each double line one additional Pt atom is incorporated into the surface. As illustrated in Fig. 5.1(e) along the 110 directions 30 surface Pt atoms reside on top of 29 substrate Pt atoms. Thus, the arrangement of double lines in the honeycomb reconstruction leads to the compression of the Pt(111) surface increasing the average atom density by $\approx 7\,\%$. In comparison, an increase of $\approx 5\,\%$ in the average surface atom density has been reported for well-ordered reconstructed areas of pristine Pt(111).[176–179]

Previously, two types of connectors were found at junctions of three double lines.[178, 179] So-called bright stars are protruding intersections of three double lines, where central Pt atoms reside at on-top sites of the Pt(111) substrate. The energy costs for the stacking faults is outweighed by the annihilation of three point dislocations.[179] Dark stars on the other hand represent junctions, where the adjacent Shockley partials of neighboring double lines connect and form an enclosed hcp-stacked region at the center. All previously reported reconstructions of the Pt(111) surface can be assigned to one fundamental honeycomb-reconstruction.[187] That is because they follow a common topological law, which is established by the energy difference between hcp and fcc stacking and forces the two types of connectors – bright and dark stars – to alternate from one junction of double lines to the next.[179, 187] Remarkably, the honeycomb-like reconstruction observed here does not adhere to this law and exhibits protrusions at all junctions of the dislocation network [Fig. 5.1(c)]. A plausible origin of this observation based on the presence of graphene is discussed in the next paragraphs.

As a first remark, graphene has two obvious effects on the stability of a reconstructed phase. While it acts as a cap layer that reduces the under-coordination of the Pt surface atoms, it also effectively captures Pt atoms close to the substrate after intercalation. An excess of Pt adatoms was previously demonstrated to promote the reconstruction of the Pt(111) surface.[178, 179] Second, the additional van der Waaals attraction between graphene and Pt surface atoms counteracts their coupling to the substrate, which facilitates a reconstruction, too. Similarly, the high-temperature reconstruction of Pt(111) was attributed to weaker bonding of the first Pt layer to the substrate due to thermally excited vibrations.[176, 177, 187] Moreover, on graphene-covered Ru(0001) another related reconstruction has been observed, which does not occur on pristine Ru(0001), demonstrating the influence of graphene.[189]

Another important consequence of the weakened substrate bonding is a diminished impact of energy differences between varying stacking geometries. The remarkably large ratio of hcp-stacked to fcc-stacked areas observed here corroborates this aspect. In the presence of graphene, we find a hcp to fcc area ratio of ≈ 0.78, while the purely temperature-induced reconstruction of Pt(111) at 1330 K yielded a ratio of only 0.43.[176, 177] In part this ratio may also be enhanced by the deposition of Pt, which was demonstrated in the homoepitaxial growth of Pt on Pt(111) yielding a hcp to fcc ratio of ≈ 0.54 at 400 K.[178, 179]

Since energy differences between the high-symmetry stacking sites are lowered in the presence of graphene, they can be outweighed by intralayer interactions in the Pt surface layer. In that case the dominating occurrence of one type of connector with a lower intralayer formation energy is enabled, invalidating the topological law described earlier. Indeed, the graphene-covered Pt(111) reconstruction observed here exhibits bright protrusions at all six double line junctions around a fcc-stacked domain. This hints at a preference of bright stars over dark stars due to a reduced formation energy in the presence of a graphene cap layer.

Cointercalation of Graphene on Ru(0001)

The adsorption of alkali metals on surfaces has a longstanding tradition in surface science.[190–192] Over the last decades, many aspects of alkali metal adsorption like the geometric structure of superlattices, [193–199] vibrational quanta, [200–203] and lifetimes of electronic excitations [204–210] have been studied. On graphene, adsorption of alkali metals was shown to, *e. g.*, tune the band gap opening between the graphene Dirac cones [211, 212] and modify the electronic transport.[213, 214] The alkali atoms preferably occupy the center of the carbon hexagons of graphite or graphene, [215, 216] which agrees well with the observations presented in this section.

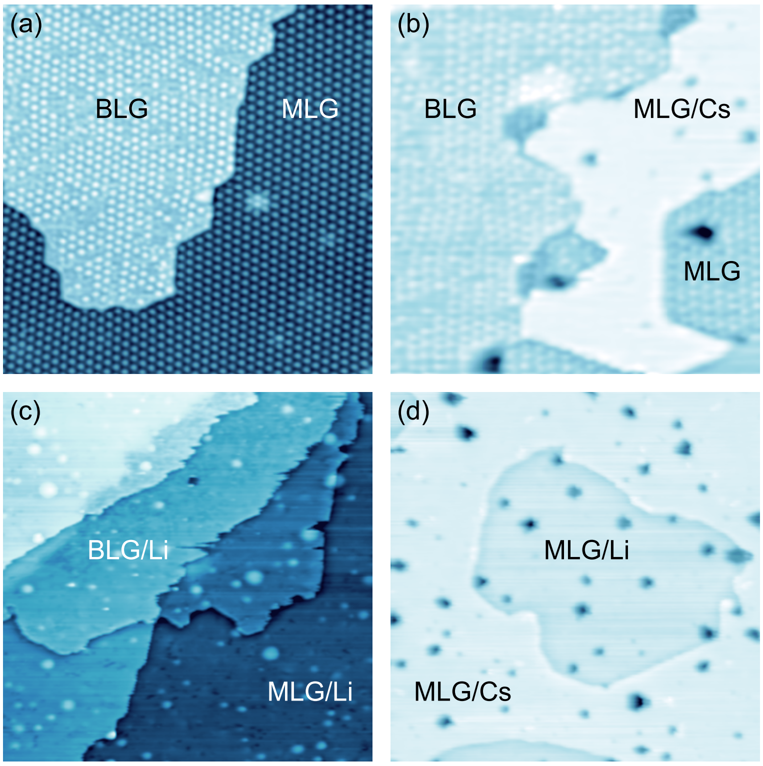

Figure 5.2: Overview of Cs and Li intercalation phases on graphene-covered Ru(0001). (a) Monolayer (MLG) and bilayer graphene (BLG) on clean Ru(0001) exhibiting their respective moiré patterns (200 mV, 100 pA, $120 \times 120\,\mathrm{nm}^2$). (b) Pristine and Cs-intercalated MLG domains adjacent to a BLG flake (200 mV, 80 pA, $90 \times 90\,\mathrm{nm}^2$). (c) Li-intercalated graphene at saturation coverage (300 mV, 100 pA, $300 \times 300\,\mathrm{nm}^2$). Both MLG and BLG are intercalated and labeled as MLG/Li and BLG/Li, respectively. (d) Cointercalation of Cs and Li (200 mV, 90 pA, $180 \times 180\,\mathrm{nm}^2$). The intercalants form separate phases due to the lower delamination energy of Li. Both alkali metals decouple graphene from the Ru(0001) substrate, resulting in essentially vanishing moiré patterns in (b-d).

In preparation of a comprehensive study of decoupled graphene layers on Ru(0001), the prepared graphene/Ru(0001) samples (section 3.2) have been intercalated by Cs and Li. Figure 5.2 gives an overview of the achieved configurations. Starting from pristine MLG and BLG [Fig. 5.2(a)] intercalation proceeds in the MLG areas first, which is demonstrated in Fig. 5.2(b) at the example of Cs. The successful intercalation is evident from the strongly reduced buckling of graphene due to the presence of alkali metal layers that decouple it from the Ru substrate. At saturation coverage intercalated BLG regions have also been observed [Fig. 5.2(c)].

To compare the intercalated structures side by side, graphene on Ru(0001) was cointercalated with Cs and Li [Fig. 5.2(d)] by depositing Li onto the Cs-intercalated sample, followed by post-annealing. The intercalants form separate phases underneath MLG as seen from the difference of $(130 \pm 4)\,\mathrm{pm}$ in apparent height between MLG/Cs and MLG/Li [Fig. 5.3(a)]. Most likely the formation of mixed phases is prevented at low temperatures by the lower delamination energy of Li compared to Cs.[15] Compared to separate phases, such two-component islands would entail a larger average graphene–Ru distance due to the larger size of Cs. The distribution of Li as numerous assemblies in the Cs matrix may hint at a demixing of Cs and Li upon cooling the sample after post-annealing. According to the established intercalation pathway through nanoscale cracks , e.g., at graphene wrinkles [15] or multi-atom vacancies [13, 14] one would expect fewer but larger Li-intercalated regions. Alternatively, reactive intercalation [14, 217, 218] may cause many Li islands to start growing separately and can yield a similar appearance.

The atomic arrangement of the intercalated alkali metals can be inferred from the close-up views in Figs. 5.3(b,c). On Cs-intercalated regions the honeycomb lattice of graphene is superimposed with a regular hexagonal pattern of depressions. The 2D Fourier transform [inset to Fig. 5.3(b)] reveals a (2×2) superlattice of Cs with respect to graphene. Thus, the inserted Cs atoms apparently interact stronger with graphene than with the Ru substrate. On clean Ru(0001) the on-top sites were identified as favored adsorption positions for a (2×2)-Cs superstructure [195] but are not anymore occupied consistently in MLG/Cs/Ru(0001). Similar conclusions have been drawn for a (2×2)-Cs lattice with respect to graphene observed from Cs-intercalated MLG on Ir(111).[15]

Li-intercalated MLG/Ru(0001) displays only the honeycomb lattice in atomic resolution imaging [Fig. 5.3(c)]. Disordered phases of Li have been reported from room temperature photoemission experiments on intercalated MLG/Ir(111) and would cause such an appearance.[219] On pristine Ru(0001), commensurate (2×2)-Li, $(\sqrt{3} \times \sqrt{3})\mathrm{R}30°$-Li superstructures have been reported.[194, 197] Preferred adsorption in substrate fcc and hcp sites was determined, respectively.[197, 220] At larger submonolayer coverage incommensurate superstructures occur, where Li atoms adopt different adsorption sites.[220] However, a more plausible explanation of our observations considering the much lower temperature of 5 K in this experiment compared

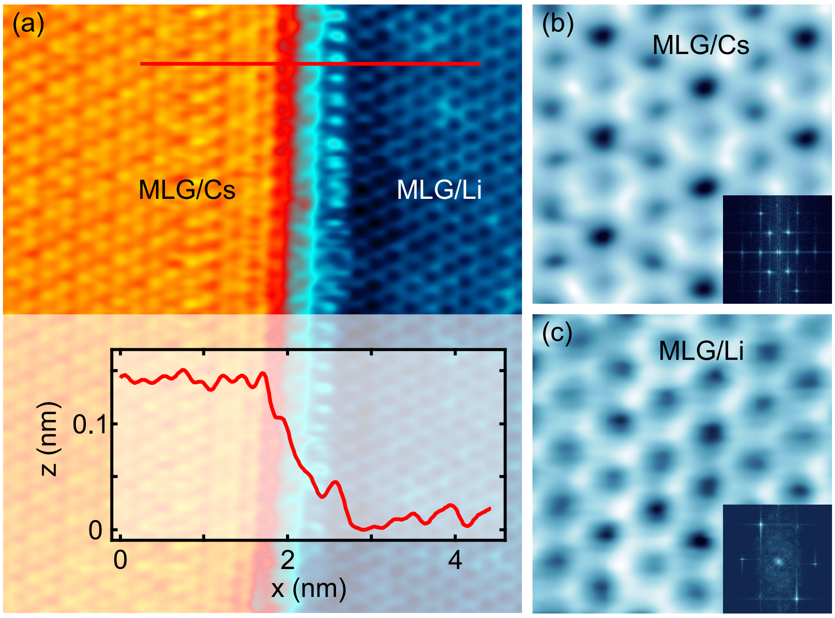

Figure 5.3: Atomic structure of Cs and Li intercalation phases under MLG on Ru(0001). (a) STM image of adjacent Cs and Li intercalation phases (200 mV, 90 pA, $5.5 \times 8\,\mathrm{nm}^2$). Inset: Cross-sectional apparent height profile acquired along the indicated line. (b) Close-up view of Cs-intercalated domain with atomic resolution (200 mV, 90 pA, $1.5 \times 1.5\,\mathrm{nm}^2$). Inset: Fourier transform of (b) ($11.9 \times 11.9\,\mathrm{nm}^{-2}$) with outer spots reflecting the C lattice of MLG. The inner spots indicate the (2×2)-Cs superlattice. (c) Like (b) for a Li-intercalated region. Inset: Like the inset to (b) with coinciding spots of the MLG C lattice and a (1×1)-Li superstructure.

to these previous reports is a (1×1)-Li superstructure, where the centers of the carbon hexagons are occupied with one Li atom each.[215, 216] The observation of a $(\sqrt{3} \times \sqrt{3})$R30°-Li superlattice at a coverage of 0.33 ML – also with respect to graphene and at a similarly low temperature of 6 K – was previously determined from MLG/Ir(111) and corroborates this interpretation.[92]

Both alkali superstructures are formed with respect to graphene irrespective of their preferred adsorption sites on pristine Ru(0001). This indicates that the energy landscape for the alkali metals at the substrate surface is altered significantly by the graphene cover layer. The additional interaction with graphene mediates a template effect for the alkali superlattices.

5.4 Conclusions

The presence of graphene modifies the interplay of interlayer and intralayer interactions that determines the arrangement of intercalant assemblies. A reconstruction of the graphene-covered Pt(111) surface with increased regularity and extension compared to reconstructions of pristine Pt(111) has been observed. The invalidation of a previously established topological law in the underlying dislocation network demonstrates the influence of graphene. Its interaction with the Pt surface atoms weakens their binding to the substrate and concomitantly reduces stacking-dependent energy costs. Consequently, the impact of intralayer interactions is enhanced.

Moreover, the cointercalation of graphene on Ru(0001) with Cs and Li revealed an even stronger effect of the graphene cover layer. The prepared sample exhibited separate phases of Cs and Li, which both formed superstructures that are oriented at the lattice of graphene rather than the Ru substrate. In turn, the intercalants decouple the graphene from the Ru surface.

6 Conclusions and Prospects

The first part of the thesis was devoted to a contribution to the general understanding of phonon-mediated tunneling into graphene on surfaces. Inelastic electron tunneling spectroscopy (IETS) investigations of graphene on Ir(111) intercalated with Cs and Li demonstrated the observation of graphene phonon signatures from all-metal samples. The signal strength of these phonon features was tuned by the chemical nature and the coverage of the intercalant as well as by the tip–graphene separation. In combination with transport calculations based on a three-terminal setup the experimental data laid the foundation for a comprehensive model, which describes the connections of the graphene–substrate and graphene–tip coupling with the phonon signal strength in IETS. A follow-up study of monolayer (MLG) and bilayer graphene (BLG) on Ru(0001) was presented next. Spatially resolved IETS revealed a variation of the observed phonon intensity between the different high-symmetry sites of the moiré patterns of MLG and BLG. In the latter case, this behavior was attributed to the local changes in the interlayer coupling between the two graphene sheets, in agreement with the previously developed model. The unexpected observation of similar phonon signatures on MLG/Ru(0001) gave first insights into the strong-hybridization case and may hint at a spatial modulation of the electron–phonon coupling caused by the moiré pattern.

The model description based on the obtained IETS data is certainly a progress in the development of a general understanding of phonon-mediated tunneling into graphene on surfaces. It includes the coupling of graphene to the surface and the STM tip and is, therefore, likely to find application in the interpretation of future IETS experiments on graphene and possibly other two-dimensional materials. Moreover, the observed spatial variation of the phonon signal strength with the moiré patterns of MLG and BLG on Ru(0001) represents a foundation for further experimental and theoretical investigations, especially of the strong-hybridization case.

The second chapter of this work presented the successful implementation of the self-limiting CVD growth of graphene for the preparation of bilayer graphene on Pt(111). After the first layer growth, additional Pt was deposited on the graphene-covered surface to reactivate it for the subsequent second layer CVD. Intercalation of the added Pt beneath the lower graphene sheet then yielded bilayer graphene on the substrate. STM imaging and analysis of the observed moiré patterns corroborated the presence of BLG and revealed the graphene–Pt interface at the origin of the moiré patterns in BLG domains.

The developed sequential CVD protocol for the growth of bilayer graphene on Pt(111) is anticipated to become useful for future experiments but may also motivate similar strategies for the preparation of layered heterostructures of graphene with other two-dimensional materials. Due to its simple concept, further combinations of CVD precursors and metals are conceivable.

The third part of this thesis addressed the impact of graphene on intercalant superstructures. A reconstruction of the graphene-covered Pt(111) surface induced by the intercalation with Pt was identified. From the qualitative differences in the underlying dislocation network compared to a class of similar reconstructions of Pt(111) the influence of graphene on the balance of interlayer and intralayer interactions was inferred. Furthermore, graphene on Ru(0001) was successfully cointercalated with Cs and Li. STM imaging on the separate phases formed by the intercalants revealed atomic superlattices, which are (2 × 2)-Cs and (1 × 1)-Li. Both superstructures are formed with respect to graphene and irrespective of the preferred alkali adsorption sites on the Ru(0001) substrate, which indicates a strong interaction of the intercalants with graphene.

Superstructures offer various possibilities for the modification of graphene s properties. The established impact of graphene on the observed Pt(111) reconstruction may inspire the modification of other existing surface reconstructions through the presence of graphene. This could be an interesting concept to create novel surface patterns. The intercalation of graphene on Ru(0001) with Cs and Li represents one experimental pathway to tailor the graphene–Ru(0001) interaction for upcoming experiments, *e. g.*, further IETS investigations similar to the presented study on Ir(111). Additionally, potential demixing processes during the cooldown of the cointercalated graphene may provide opportunities to design multi-component patterns at the nanoscale.

Appendix

A Transport Calculations of Intercalated Graphene on Ir(111)

Reproduced in part with permission from
Nano Lett., 18(9): 5697–5701, 2018.
Copyright 2018 American Chemical Society.
Transport calculations provided by Mads Brandbyge from the Technical University of Denmark, Department of Micro- and Nanotechnology.

Details of the Density Functional Theory (DFT) Modeling

Following Andersen et al.,[98] the optB88-vdW functional [221] and plane-wave calculations [222] were used to relax the sample structures. A slab of four Ir(111) layers entered into the simulations. For graphene a (6×6) unit cell was used together with a 2×2 k-point sampling. The Ir slab was kept fixed and strained by $\approx 2\,\%$ to match the graphene unit cell dimensions, while the intercalant (Cs or Li) and graphene were relaxed. For Cs the distance between Ir and graphene is $630 \pm 7\,\mathrm{pm}$, while it is $430 \pm 8\,\mathrm{pm}$ in the case of Li (the ranges indicate the rippling), in reasonable agreement with previous findings.[98] In both cases we find a considerable n-doping corresponding to a Fermi energy of $\varepsilon_\mathrm{F} \approx 1\,\mathrm{eV}$.

The relaxed structures served as an input to the subsequent nonequilibrum Green function (NEGF) calculations. The SIESTA code [223] combined with the TRANSIESTA method, [93, 224] and the INELASTICA package [225] to obtain the electron-phonon couplings via finite displacements of the atoms were applied. To this end, Ir electrodes were attached to the relaxed structures and a small Au tip was mounted [Fig. A.1(a,b)]. The Perdew-Burke-Ernzerhof (PBE) functional [226] with the standard single-zeta polarized (SZP) linear combination of atomic orbitals (LCAO) basis [223] was used for the Ir, the double-zeta polarized (DZP) basis for the outermost

Ir layer and for the intercalants, and for graphene a double-zeta double-polarized (DZDP) basis set with range up to 0.45 nm, which includes the lowest unoccupied bands of graphene.[30, 95]

Multi-electrode Setup

We emphasize that the boundary conditions for the electron transport are crucial for describing the experiments. In a standard inelastic DFT-NEGF calculation one typically considers two terminals, tip and substrate, and uses periodic boundary

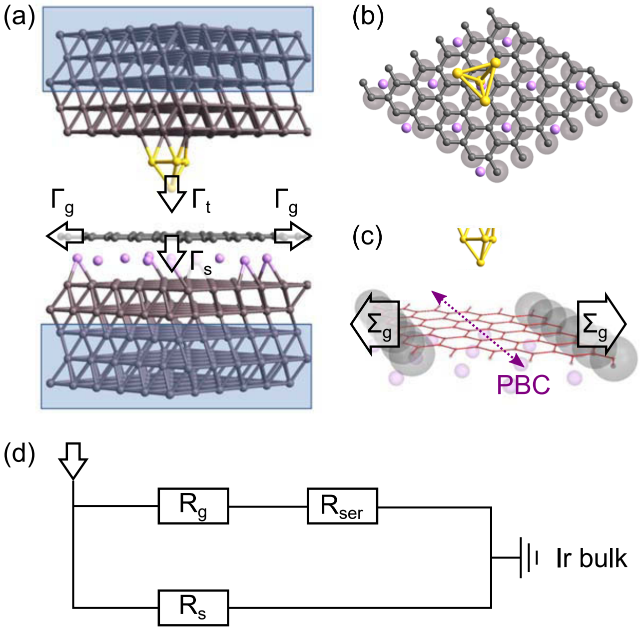

Figure A.1: (a) Setup of the transport calculation for the example of Li. The Au tip atom is 440 pm above the graphene plane. Electrodes are attached at the slab regions indicated by the shaded areas. Schematically, electron escape rates to the tip, Γ_t, to graphene, Γ_g, and to the substrate, Γ_s, are considered. (b) Tip and sample unit cell seen from above. (c) The three-terminal setup where electrons can terminate in the tip, graphene or the Ir substrate electrode. The graphene terminal is introduced in the calculations by using a pristine-graphene self-energy ($\boldsymbol{\Sigma}_g$, marked by gray spheres) in the indicated directions in the graphene plane instead of periodic boundary conditions (PBC). PBC are used in the remaining direction in the graphene plane (dashed arrow). (d) Simple resistor picture for the electron transport from the tip to the bulk Ir electrode. The current injected into the graphene plane (represented by the resistance R_g) outside the unit cell will eventually end up in the Ir bulk electrode (R_s) via a series resistance (R_{ser}).

conditions (PBC) in the transverse direction on the total structure. For large unit cells as in the present case one will typically use only a few transverse k-points. However, this setup results in vanishing vibrational signatures in the current and does not reproduce the experimental results.

In order to model the experimental data, where the inelastic conductance steps are of the same order of magnitude as the zero-bias conductance, it is important to resolve the states at the Fermi level in graphene. Instead of using a prohibitively fine transverse k-point sampling an alternative approach is proposed here by attaching a third terminal that collects freely propagating electrons in the strongly n-doped graphene layer. This amounts to replacing the PBC by open boundary conditions in one graphene direction with graphene self-energies [$\mathbf{\Sigma}_\mathrm{g}$ in Fig. A.1(c)] as done in DFT-NEGF transport calculations.[93, 224]

We calculate $\mathbf{\Sigma}_\mathrm{g}$ for a pristine graphene cell with the same parameters as in the full cell and fix the energy of $\mathbf{\Sigma}_\mathrm{g}$ to that of the Fermi energy of intercalated graphene. The PBC are kept in the remaining transverse direction for computational simplicity, and the Γ-point approximation is used like for the Ir electrodes in both transverse directions. Thus, the electrons in graphene can couple with effective rates Γ_t, Γ_g, and Γ_s to, respectively, the tip, graphene outside the central cell, and the substrate as shown in Fig. A.1a, although these rates are not directly available or defined in the full calculation. A benefit of this approach is the possibility of evaluating the current that branches into the graphene under the tip, escapes into graphene, and only at some later stage enters the bulk metal electrode away from the tip region [Fig. A.1(a)]. We find that to a good approximation the total conductance equals the sum of the conductances of the graphene and the Ir substrate terminal. In a simple picture our setup can, therefore, be visualized as two resistors in parallel as depicted in Fig. A.1(d), with an additional serial resistance R_ser for electrons that enter the substrate only outside the unit cell.

Calculation of Inelastic Electron Transport

The inelastic contribution to the current is obtained from the lowest-order expansion (LOE) method.[96] The expressions can easily be split into contributions from each of the terminals, e. g., from graphene and Ir, assuming the same chemical potential in graphene and Ir. Following a previous report, [96] the contribution of each terminal for a given mode   is calculated as

$$
\begin{aligned}
{}^{2}_{V}I^{\alpha}(V) = (\;\;_{i,}\; + \mathrm{Im}B^{\alpha})\;\; {}^{2}_{V}\mathcal{I}^{\mathrm{sym}}(V, \hbar\omega\;\;, T, N\;\;) \\
+ (2\mathrm{Re}B^{\alpha})\;\; {}^{2}_{V}\mathcal{I}^{\mathrm{asym}}(V, \hbar\omega\;\;, T),
\end{aligned}
\tag{A.1}
$$

where the constants are given in terms of Green functions (**G**), spectral functions (**A**), and electron-phonon couplings ( )

$$
\begin{aligned}
B^{\alpha} \quad \mathrm{Tr}[\;\;_{\alpha}(\;\;_{L})\,\mathbf{G}(\;\;_{L})\mathbf{M}\;\;\mathbf{A}_{R}(\;\;_{R})\mathbf{M}\;\;\mathbf{A}_{R}(\;\;_{L}) \\
-\;\;_{\alpha}(\;\;_{R})\,\mathbf{A}_{R}(\;\;_{R})\mathbf{M}\;\;\mathbf{A}_{L}(\;\;_{L})\mathbf{M}\;\;\mathbf{G}\;(\;\;_{R})],
\end{aligned}
\tag{A.2}
$$

and

$$
{}^{\alpha}_{i,} = \mathrm{Tr}\;\;\;_{\alpha}(\;\;_{L})\,\mathbf{G}(\;\;_{L})\mathbf{M}\;\;\mathbf{A}_{R}(\;\;_{R})\mathbf{M}\;\;\mathbf{G}\;(\;\;_{L})
\tag{A.3}
$$

with the chemical potentials $_{L}$, $_{R}$ for, respectively, left and right electrode. We use an energy constant   in graphene (due to the artificial PBC in one direction) and consider only the voltage-symmetric part of the conductance. Furthermore, contributions from Ir phonons ($<$ 20 meV) are neglected, and only vibrations of the C atoms are included. The central inelastic scattering region in the calculation setting the size of the σ–π coupling matrix **M** includes two layers of Ir on both sides (Fig. A.1).

Simple Model

The findings obtained by the DFT-NEGF calculation can be expressed in a simplified two-level model involving a π-state at K/K with energy ($\varepsilon_{\pi} = \varepsilon_{\mathrm{F}} \approx 0\,\mathrm{eV}$) and a σ-state representing the first unoccupied band at Γ with energy ε_{σ}. This model is inspired by a previous work, [30] although the σ-state in principle could also represent a tip s-state.

The wide-band approximation is used and the coupling of the graphene π-state to the substrate is modeled by an imaginary self-energy (inverse lifetime) Γ_{π}. The σ-state is also coupled to the substrate *via* Γ_{σ} as well as to the tip *via* Γ_{t}. The σ-state has a long range [95] and, thus, $\Gamma_{\sigma} > \Gamma_{\pi}$. Considering now that the current can flow directly between the tip, σ-state and the substrate, or from the tip, σ-state *via* phonon excitation (electron-phonon coupling λ) to the graphene π-state and subsequently to the substrate, the corresponding unperturbed (no phonon) Green function reads

$$\mathbf{G} = \begin{matrix} \varepsilon - \mathrm{i}\frac{\ _{\pi}}{2} & 0 \\ 0 & \varepsilon - \varepsilon_\sigma - \mathrm{i}\frac{\ _{\mathrm{t}}+\ _{\sigma}}{2} \end{matrix}^{-1} . \tag{A.4}$$

The phonon couples the σ and π-state by the matrix

$$\mathbf{M} = \lambda \begin{matrix} 0 & 1 \\ 1 & 0 \end{matrix} . \tag{A.5}$$

For the inelastic process the lowest-order (symmetric) inelastic conductance step height is [96, 97]

$$= \mathrm{Tr}[\mathbf{M}\tilde{\mathbf{A}}_L\mathbf{M}\mathbf{A}_R] \tag{A.6}$$

with $\mathbf{A}_R = \mathbf{G}\quad_R\mathbf{G}$ ($\tilde{\mathbf{A}}_L = \mathbf{G}\quad_L\mathbf{G}$), $\mathbf{A}_R$ ($\tilde{\mathbf{A}}_L$) being the right (left time-reversed) spectral function. The right electrode R may represent the tip,

$$_R = \begin{matrix} 0 & 0 \\ 0 & \Gamma_\mathrm{t} \end{matrix} \tag{A.7}$$

while the left electrode L represents the substrate,

$$_L = \begin{matrix} \Gamma_\pi & 0 \\ 0 & \Gamma_\sigma \end{matrix} . \tag{A.8}$$

The inelastic step height reads

$$= \lambda^2 A_\pi(\varepsilon_\mathrm{F} + \hbar\quad)A_\sigma(\varepsilon_\mathrm{F}) \tag{A.9}$$

where ($\varepsilon_\mathrm{F}\quad 0\,\mathrm{eV}$),

$$A_\sigma(\varepsilon_\mathrm{F}) = \frac{\Gamma_\mathrm{t} + \Gamma_\sigma}{\varepsilon_\sigma^2 + \quad\frac{\ _\mathrm{t}}{2} + \frac{\ _\sigma}{2}\quad^{2}}, \tag{A.10}$$

and

$$A_\pi(\varepsilon_\mathrm{F}) = \frac{\Gamma_\pi}{(\hbar\quad)^2 + \quad\frac{\ _\pi}{2}\quad^{2}}. \tag{A.11}$$

Likewise, the zero-bias conductance is obtained as

$$g(0) = \mathrm{Tr}[\quad_L\mathbf{A}_R] = \frac{\Gamma_\mathrm{t}\,\Gamma_\sigma}{\varepsilon_\sigma^2 + \quad\frac{\ _\mathrm{t}}{2} + \frac{\ _\sigma}{2}\quad^{2}}. \tag{A.12}$$

If we assume $\hbar \quad \Gamma_\pi$ and neglect the vibrational energy we can now calculate the relative conductance increase (inelastic step height divided by the zero-bias conductance),

$$\frac{\Delta g}{g(0)} = \frac{}{g(0)} = \frac{4\lambda^2}{\Gamma_\pi} \quad \frac{1}{\Gamma_\mathrm{t}} + \frac{1}{\Gamma_\sigma} \quad . \tag{A.13}$$

For small tip coupling $\Gamma_\mathrm{t} \quad \Gamma_\sigma$ we obtain

$$\frac{}{g(0)} = \frac{4\lambda^2}{\Gamma_\mathrm{t}\Gamma_\pi}. \tag{A.14}$$

This explains why for increased hybridization of graphene with the substrate or increased tip–graphene coupling, the inelastic signals become quenched in the experiments.

In the limit of very small substrate coupling ($\Gamma_\pi, \Gamma_\sigma \quad \hbar \quad, \Gamma_\mathrm{t}$) the relative conductance increase is

$$\frac{}{g(0)} = \frac{\lambda^2}{(\hbar \quad)^2}\frac{\Gamma_\pi}{\Gamma_\sigma}, \tag{A.15}$$

where now the coupling Γ_π becomes a bottle-neck for the inelastic process.

When the tip is in direct contact with graphene we may expect $\Gamma_\mathrm{t} \quad \Gamma_\sigma$ and thus

$$\frac{}{g(0)} = \frac{4\lambda^2}{\Gamma_\sigma\Gamma_\pi}\,. \tag{A.16}$$

Assuming that Γ_σ and Γ_π scale in the same way as we change the distance to the substrate, we get a scaling with substrate Hamiltonian matrix element, w, $\Gamma_\pi \quad \Gamma_\sigma$ w^2,

$$\frac{}{g(0)} \quad \frac{1}{w^2} \quad 1 + \frac{a}{w^2} \quad , \tag{A.17}$$

where a is the ratio $\Gamma_\mathrm{t}/\Gamma_\sigma$ at $w = 1$. In Fig. A.2 we show the fit of this expression to the DFT results.

To obtain a simple measure of the coupling to the π orbitals directly from the DFT-NEGF calculation we calculate

$$\Gamma_\pi = \frac{\mathrm{Tr}[\mathbf{S}\,(\mathbf{P}_\pi\mathbf{A}(E_F)\mathbf{P}_\pi)\,\mathbf{P}_\pi \quad (E_F)\mathbf{P}_\pi]}{\mathrm{Tr}[\mathbf{S}\,(\mathbf{P}_\pi\mathbf{A}(E_F)\mathbf{P}_\pi)]} \tag{A.18}$$

where $\mathbf{P}_\pi$ is the projection matrix onto the π-electronic system of graphene. Here, the broadening of the π-states is estimated by projecting the broadening matrix, , obtained from the self-energy of the entire intercalated sample, weighted by graphene p_z-states via the projection of the spectral density ($\mathbf{A}$) at the Fermi level, to the π system (and including the non-orthogonality via the overlap matrix, $\mathbf{S}$). This

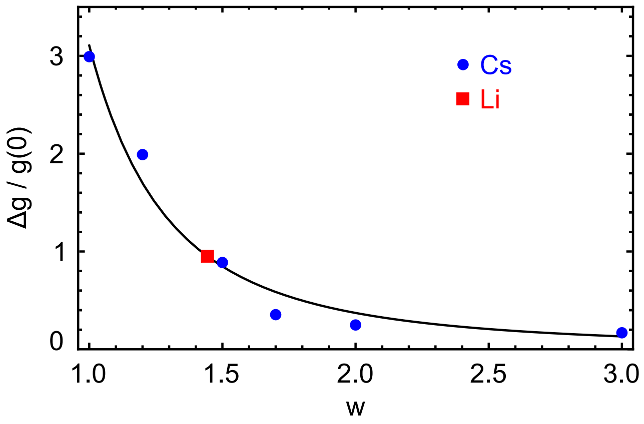

Figure A.2: Fit (solid line) of Eq. A.17 to the DFT results for Cs (dots), where the Hamiltonian matrix element, w, between C and Ir atoms was scaled by hand. The unscaled Li data point (squares) is shown for comparison.

procedure yields a lifetime broadening of $\Gamma_\pi = 0.67\,\mathrm{eV}$ for Li and $\Gamma_\pi = 0.18\,\mathrm{eV}$ for Cs, which is in good agreement with the ratio of $\Delta g(\mathrm{Cs})/\Delta g(\mathrm{Li}) \approx 3 \approx \Gamma_\pi(\mathrm{Li})/\Gamma_\pi(\mathrm{Cs})$ for similar Γ_t (tip distances). From the simple fit procedure (Fig. A.2) λ and Γ_σ can be estimated. The fit yields $\Gamma_t/\Gamma_\sigma = a \approx 2.3$. Using $g_0 = 0.02\,G_0$ in Eq. A.12 and $\Delta g/g_0 \approx 3$ in Eq. A.13 leads to $\Gamma_\sigma = 0.35\,\mathrm{eV}$ for Cs and $\lambda = 0.18\,\mathrm{eV}$ for both intercalants. Consequently, for Li the coupling is scaled to $\Gamma_\sigma = 3\ \ 0.35\,\mathrm{eV} = 1.05\,\mathrm{eV}$. These results are summarized in Table A.1 below.

Table A.1: Coupling constants for the calculated Cs and Li systems obtained from the fitting procedure described in the text.

	Γ_σ (eV)	Γ_π (eV)	λ (eV)
Cs	0.35	0.18	0.18
Li	1.05	0.67	0.18

List of Figures

List of Tables

List of Scientific Contributions

Peer-Reviewed Journal Publications

1. Johannes Halle, Nicolas Néel, Jörg Kröger:

   Tailoring Intercalant Assemblies at the Graphene–Metal Interface,

   Langmuir, 35(7): 2554–2560, 2019.

2. Johannes Halle, Alexander Mehler, Nicolas Néel, Jörg Kröger:

   Preparation of graphene bilayers on platinum by sequential chemical vapour deposition,

   Phys. Chem. Chem. Phys., 21: 3140-3144, 2019.

3. Johannes Halle, Nicolas Néel, Mikhail Fonin, Mads Brandbyge, Jörg Kröger:

   Understanding and Engineering Phonon-Mediated Tunneling into Graphene on Metal Surfaces,

   Nano Lett., 18(9): 5697–5701, 2018.

4. Johannes Halle, Nicolas Néel, Jörg Kröger:

   Filling the Gap: Li-Intercalated Graphene on Ir(111),

   J. Phys. Chem. C, 120(9): 5067–5073, 2016.

Conference Talks

1. Johannes Halle, Nicolas Néel, Mads Brandbyge, Tim O. Wehling, Jörg Kröger:

   Graphene phonons in Inelastic Electron Tunneling Spectroscopy,

   DPG-Frühjahrstagung,

   Dresden, Germany, 2017.

2. Johannes Halle, Nicolas Néel, Jörg Kröger:

   Graphene phonons in Inelastic Electron Tunneling Spectroscopy,

   3rd International Conference & 5th International MacroNano-Colloquium on the Challenges and Perspectives of Functional Nanostructures,

   Ilmenau, Germany, 2016.

Poster Presentations

1. Johannes Halle, Nicolas Néel, Jörg Kröger:

   Inelastic Excitations in Bilayer Graphene on Ru(0001),

   4th European Workshop on Epitaxial Graphene and 2D Materials,

   Salamanca, Spain, 2018.

2. Johannes Halle, Nicolas Néel, Mads Brandbyge, Jörg Kröger:

   Graphene phonons in Inelastic Electron Tunneling Spectroscopy,

   21. Deutsche Physikerinnentagung,

   Ilmenau, Germany, 2017.

3. Johannes Halle, Nicolas Néel, Mads Brandbyge, Jörg Kröger:

   Graphene phonons in Inelastic Electron Tunneling Spectroscopy,

   8th International Workshop on Surface Physics,

   Trzebnica, Poland, 2017.

4. Johannes Halle, Nicolas Néel, Jörg Kröger:

   Superstructures and Phonons of Graphene on Ir(111) Induced by Li Intercalation,

   80. Jahrestagung der DPG und DPG-Frühjahrstagung,

   Regensburg, Germany, 2016.

5. Johannes Halle, Nicolas Néel, Jörg Kröger:

   Superstructures and Phonons of Graphene on Ir(111) Induced by Li Intercalation,

   598th WEH Seminar Frontiers in Scanning Probe Microscopy,

   Bad Honnef, Germany, 2015.

Bibliography

[1] K. S. Novoselov, V. I. Fal ko, L. Colombo, P. R. Gellert, M. G. Schwab, and K. Kim. A roadmap for graphene. *Nature*, 490: 192, 2012.

[2] A. C. Ferrari, F. Bonaccorso, V. Fal ko, K. S. Novoselov, S. Roche, P. Bøggild, S. Borini, F. H. L. Koppens, V. Palermo, N. Pugno, J. A. Garrido, R. Sordan, A. Bianco, L. Ballerini, M. Prato, E. Lidorikis, J. Kivioja, C. Marinelli, T. Ryhänen, A. Morpurgo, J. N. Coleman, V. Nicolosi, L. Colombo, A. Fert, M. Garcia-Hernandez, A. Bachtold, G. F. Schneider, F. Guinea, C. Dekker, M. Barbone, Z. Sun, C. Galiotis, A. N. Grigorenko, G. Konstantatos, A. Kis, M. Katsnelson, L. Vandersypen, A. Loiseau, V. Morandi, D. Neumaier, E. Treossi, V. Pellegrini, M. Polini, A. Tredicucci, G. M. Williams, B. Hee Hong, J.-H. Ahn, J. Min Kim, H. Zirath, B. J. van Wees, H. van der Zant, L. Occhipinti, A. Di Matteo, I. A. Kinloch, T. Seyller, E. Quesnel, X. Feng, K. Teo, N. Rupesinghe, P. Hakonen, S. R. T. Neil, Q. Tannock, T. Löfwander, and J. Kinaret. Science and technology roadmap for graphene, related two-dimensional crystals, and hybrid systems. *Nanoscale*, 7: 4598–4810, 2015.

[3] K. S. Novoselov, A. K. Geim, S. V. Morozov, D. Jiang, M. I. Katsnelson, I. V. Grigorieva, S. V. Dubonos, and A. A. Firsov. Two-dimensional gas of massless Dirac fermions in graphene. *Nature*, 438: 197, 2005.

[4] Y. Zhang, Y.-W. Tan, H. L. Stormer, and P. Kim. Experimental observation of the quantum Hall effect and Berry s phase in graphene. *Nature*, 438: 201, 2005.

[5] S. Das Sarma, S. Adam, E. H. Hwang, and E. Rossi. Electronic transport in two-dimensional graphene. *Rev. Mod. Phys.*, 83: 407–470, 2011.

[6] J. Wintterlin and M.-L. Bocquet. Graphene on metal surfaces. *Surf. Sci.*, 603 (10): 1841–1852, 2009.

[7] B. Deng, Z. Liu, and H. Peng. Toward Mass Production of CVD Graphene Films. *Adv. Mater.*, 1800996, 2018.

[8] A. B. Preobrajenski, M. L. Ng, A. S. Vinogradov, and N. Mårtensson. Controlling graphene corrugation on lattice-mismatched substrates. *Phys. Rev. B*, 78: 073401, 2008.

[9] P. Merino, M. ’ vec, A. L. Pinardi, G. Otero, and J. A. Martín-Gago. Strain-driven moiré superstructures of epitaxial graphene on transition metal surfaces. *ACS Nano*, 5(7): 5627–5634, 2011.

[10] B. Wang, M.-L. Bocquet, S. Marchini, S. Günther, and J. Wintterlin. Chemical origin of a graphene moire overlayer on Ru(0001). *Phys. Chem. Chem. Phys.*, 10: 3530–3534, 2008.

[11] T. Brugger, S. Günther, B. Wang, J. H. Dil, M.-L. Bocquet, J. Osterwalder, J. Wintterlin, and T. Greber. Comparison of electronic structure and template function of single-layer graphene and a hexagonal boron nitride nanomesh on Ru(0001). *Phys. Rev. B*, 79: 045407, 2009.

[12] M. Dresselhaus and G. Dresselhaus. Intercalation compounds of graphite. *Adv. Phys.*, 30(2): 139–326, 1981.

[13] M. Büttner, P. Choudhury, J. Johnson, and J. Yates. Vacancy clusters as entry ports for cesium intercalation in graphite. *Carbon*, 49(12): 3937–3952, 2011.

[14] L. Jin, Q. Fu, Y. Yang, and X. Bao. A comparative study of intercalation mechanism at graphene/Ru(0001) interface. *Surf. Sci.*, 617: 81–86, 2013.

[15] M. Petrovi , I. ’ rut Raki , S. Runte, C. Busse, J. T. Sadowski, P. Lazi , I. Pletikosi , Z.-H. Pan, M. Milun, P. Pervan, N. Atodiresei, R. Brako, D. ’ ok evi , T. Valla, T. Michely, and M. Kralj. The mechanism of caesium intercalation of graphene. *Nat. Commun.*, 4: 2772, 2013.

[16] K. V. Emtsev, A. A. Zakharov, C. Coletti, S. Forti, and U. Starke. Ambipolar doping in quasifree epitaxial graphene on SiC(0001) controlled by Ge intercalation. *Phys. Rev. B*, 84: 125423, 2011.

[17] C. Enderlein, Y. S. Kim, A. Bostwick, E. Rotenberg, and K. Horn. The formation of an energy gap in graphene on ruthenium by controlling the interface. *New J. Phys.*, 12(3): 033014, 2010.

[18] A. Varykhalov, M. R. Scholz, T. K. Kim, and O. Rader. Effect of noble-metal contacts on doping and band gap of graphene. *Phys. Rev. B*, 82: 121101, 2010.

[19] C. Riedl, C. Coletti, T. Iwasaki, A. A. Zakharov, and U. Starke. Quasi-Free-Standing Epitaxial Graphene on SiC Obtained by Hydrogen Intercalation. *Phys. Rev. Lett.*, 103: 246804, 2009.

[20] D. Pacilé, P. Leicht, M. Papagno, P. M. Sheverdyaeva, P. Moras, C. Carbone, K. Krausert, L. Zielke, M. Fonin, Y. S. Dedkov, F. Mittendorfer, J. Doppler, A. Garhofer, and J. Redinger. Artificially lattice-mismatched graphene/metal interface: Graphene/Ni/Ir(111). *Phys. Rev. B*, 87: 035420, 2013.

[21] M. Papagno, P. Moras, P. M. Sheverdyaeva, J. Doppler, A. Garhofer, F. Mittendorfer, J. Redinger, and C. Carbone. Hybridization of graphene and a Ag monolayer supported on Re(0001). *Phys. Rev. B*, 88: 235430, 2013.

[22] V. W. Brar, Y. Zhang, Y. Yayon, T. Ohta, J. L. McChesney, A. Bostwick, E. Rotenberg, K. Horn, and M. F. Crommie. Scanning tunneling spectroscopy of inhomogeneous electronic structure in monolayer and bilayer graphene on SiC. *Appl. Phys. Lett.*, 91(12): 122102, 2007.

[23] B. C. Stipe, M. A. Rezaei, and W. Ho. Single-Molecule Vibrational Spectroscopy and Microscopy. *Science*, 280(5370): 1732–1735, 1998.

[24] Y. Zhang, V. W. Brar, F. Wang, C. Girit, Y. Yayon, M. Panlasigui, A. Zettl, and M. F. Crommie. Giant phonon-induced conductance in scanning tunnelling spectroscopy of gate-tunable graphene. *Nat. Phys.*, 4: 627–630, 2008.

[25] N. Néel, C. Steinke, T. O. Wehling, and J. Kröger. Inelastic electron tunneling into graphene nanostructures on a metal surface. *Phys. Rev. B*, 95: 161410, 2017.

[26] V. W. Brar, S. Wickenburg, M. Panlasigui, C.-H. Park, T. O. Wehling, Y. Zhang, R. Decker, Ç. Girit, A. V. Balatsky, S. G. Louie, A. Zettl, and M. F. Crommie. Observation of Carrier-Density-Dependent Many-Body Effects in Graphene via Tunneling Spectroscopy. *Phys. Rev. Lett.*, 104: 036805, 2010.

[27] R. Decker, Y. Wang, V. W. Brar, W. Regan, H.-Z. Tsai, Q. Wu, W. Gannett, A. Zettl, and M. F. Crommie. Local Electronic Properties of Graphene on a BN

Substrate via Scanning Tunneling Microscopy. *Nano Lett.*, 11(6): 2291–2295, 2011.

[28] F. D. Natterer, Y. Zhao, J. Wyrick, Y.-H. Chan, W.-Y. Ruan, M.-Y. Chou, K. Watanabe, T. Taniguchi, N. B. Zhitenev, and J. A. Stroscio. Strong Asymmetric Charge Carrier Dependence in Inelastic Electron Tunneling Spectroscopy of Graphene Phonons. *Phys. Rev. Lett.*, 114: 245502, 2015.

[29] H. W. Kim, W. Ko, J. Ku, I. Jeon, D. Kim, H. Kwon, Y. Oh, S. Ryu, Y. Kuk, S. W. Hwang, and H. Suh. Nanoscale control of phonon excitations in graphene. *Nat. Commun.*, 6: 7528, 2015.

[30] T. O. Wehling, I. Grigorenko, A. I. Lichtenstein, and A. V. Balatsky. Phonon-Mediated Tunneling into Graphene. *Phys. Rev. Lett.*, 101: 216803, 2008.

[31] G. R. Bhimanapati, Z. Lin, V. Meunier, Y. Jung, J. Cha, S. Das, D. Xiao, Y. Son, M. S. Strano, V. R. Cooper, L. Liang, S. G. Louie, E. Ringe, W. Zhou, S. S. Kim, R. R. Naik, B. G. Sumpter, H. Terrones, F. Xia, Y. Wang, J. Zhu, D. Akinwande, N. Alem, J. A. Schuller, R. E. Schaak, M. Terrones, and J. A. Robinson. Recent Advances in Two-Dimensional Materials beyond Graphene. *ACS Nano*, 9(12): 11509–11539, 2015.

[32] J.-W. Jiang, B.-S. Wang, and T. Rabczuk. Acoustic and breathing phonon modes in bilayer graphene with Moiré patterns. *Appl. Phys. Lett.*, 101(2): 023113, 2012.

[33] A. I. Cocemasov, D. L. Nika, and A. A. Balandin. Phonons in twisted bilayer graphene. *Phys. Rev. B*, 88: 035428, 2013.

[34] P. Tan, W. Han, W. Zhao, Z. Wu, K. Chang, H. Wang, Y. Wang, N. Bonini, N. Marzari, N. Pugno, G. Savini, A. Lombardo, and A. Ferrari. The shear mode of multilayer graphene. *Nat. Mater.*, 11(4): 294, 2012.

[35] C. Lui, L. Malard, S. Kim, G. Lantz, F. Laverge, R. Saito, and T. Heinz. Observation of Layer-Breathing Mode Vibrations in Few-Layer Graphene through Combination Raman Scattering. *Nano Lett.*, 12(11): 5539–5544, 2012.

[36] F. Herziger, P. May, and J. Maultzsch. Layer-number determination in graphene by out-of-plane phonons. *Phys. Rev. B*, 85: 235447, 2012.

[37] C. H. Lui and T. F. Heinz. Measurement of layer breathing mode vibrations in few-layer graphene. *Phys. Rev. B*, 87: 121404, 2013.

[38] A. Castellanos-Gomez, G. Rubio-Bollinger, S. Barja, M. Garnica, A. L. Vázquez de Parga, R. Miranda, and N. Agraït. Periodic spatial variation of the electron-phonon interaction in epitaxial graphene on Ru(0001). *Appl. Phys. Lett.*, 102(6): 063114, 2013.

[39] D. Maccariello, A. Al Taleb, F. Calleja, A. L. Vázquez de Parga, P. Perna, J. Camarero, E. Gnecco, D. Farías, and R. Miranda. Observation of Localized Vibrational Modes of Graphene Nanodomes by Inelastic Atom Scattering. *Nano Lett.*, 16(1): 2–7, 2016.

[40] S. Simon, E. Voloshina, J. Tesch, F. Förschner, V. Enenkel, C. Herbig, T. Knispel, A. Tries, J. Kröger, Y. Dedkov, and M. Fonin. Layer-by-Layer Decoupling of Twisted Graphene Sheets Epitaxially Grown on a Metal Substrate. *Small*, 14(13): 1703701, 2018.

[41] Y. Zhang, L. Zhang, and C. Zhou. Review of Chemical Vapor Deposition of Graphene and Related Applications. *Acc. Chem. Res.*, 46(10): 2329–2339, 2013.

[42] H. Ibach. *Physics of surfaces and interfaces.* Springer, 2006.

[43] H. Lüth. *Solid surfaces, interfaces and thin films.* Springer, 2015.

[44] Y. Dedkov, E. Voloshina, and M. Fonin. Scanning probe microscopy and spectroscopy of graphene on metals. *Phys. Status Solidi B*, 252(3): 451–468, 2015.

[45] J. Bardeen. Tunnelling from a Many-Particle Point of View. *Phys. Rev. Lett.*, 6: 57–59, 1961.

[46] R. Wiesendanger. *Scanning Probe Microscopy and Spectroscopy: Methods and Applications.* Cambridge University Press, 1994.

[47] N. D. Lang. Spectroscopy of single atoms in the scanning tunneling microscope. *Phys. Rev. B*, 34: 5947–5950, 1986.

[48] A. Messiah. *Quantenmechanik Bd. 1.* de Gruyter, 1991.

[49] N. Lorente and M. Persson. Theory of Single Molecule Vibrational Spectroscopy and Microscopy. *Phys. Rev. Lett.*, 85: 2997–3000, 2000.

[50] N. Lorente, M. Persson, L. J. Lauhon, and W. Ho. Symmetry Selection Rules for Vibrationally Inelastic Tunneling. *Phys. Rev. Lett.*, 86: 2593–2596, 2001.

[51] W. Ho. Single-molecule chemistry. *J. Chem. Phys.*, 117(24): 11033–11061, 2002.

[52] B. N. J. Persson. Inelastic vacuum tunneling. *Phys. Scr.*, 38(2): 282, 1988.

[53] J. Kirtley and P. Hansma. An experimental test of symmetry selection rules in inelastic electron tunneling spectroscopy (IETS). *Surf. Sci.*, 66(1): 125–130, 1977.

[54] M. Galperin, M. A. Ratner, A. Nitzan, and A. Troisi. Nuclear Coupling and Polarization in Molecular Transport Junctions: Beyond Tunneling to Function. *Science*, 319(5866): 1056–1060, 2008.

[55] A. Troisi and M. A. Ratner. Propensity rules for inelastic electron tunneling spectroscopy of single-molecule transport junctions. *J. Chem. Phys.*, 125(21): 214709, 2006.

[56] A. Troisi and M. A. Ratner. Molecular Transport Junctions: Propensity Rules for Inelastic Electron Tunneling Spectra. *Nano Lett.*, 6(8): 1784–1788, 2006.

[57] M. A. Reed. Inelastic electron tunneling spectroscopy. *Mater. Today*, 11(11): 46–50, 2008.

[58] K. Hipps and U. Mazur. Inelastic electron tunneling: an alternative molecular spectroscopy. *J. Phys. Chem.*, 97(30): 7803–7814, 1993.

[59] M. Kunz. Aufbau eines Rastertunnelmikroskops für Messungen bei tiefen Temperaturen. Master s thesis, TU Ilmenau, 2011.

[60] Y. Dedkov and E. Voloshina. Graphene growth and properties on metal substrates. *J. Phys.: Condens. Matter*, 27(30): 303002, 2015.

[61] O. Binnig, H. Rohrer, C. Gerber, and E. Stoll. Real-space observation of the reconstruction of Au(100). *Surf. Sci.*, 144(2): 321–335, 1984.

[62] O. Hernán, A. V. de Parga, J. Gallego, and R. Miranda. Self-surfactant effect on Fe/Au(100): place exchange plus Au self-diffusion. *Surf. Sci.*, 415(1): 106–121, 1998.

[63] I. Horcas, R. Fernández, J. Gomez-Rodriguez, J. Colchero, J. Gómez-Herrero, and A. Baro. WSXM: a software for scanning probe microscopy and a tool for nanotechnology. *Rev. Sci. Instrum.*, 78(1): 013705, 2007.

[64] M. Endlich, A. Molina-Sánchez, L. Wirtz, and J. Kröger. Screening of electron-phonon coupling in graphene on Ir(111). *Phys. Rev. B*, 88: 205403, 2013.

[65] C. Lee, X. Wei, J. W. Kysar, and J. Hone. Measurement of the Elastic Properties and Intrinsic Strength of Monolayer Graphene. *Science*, 321(5887): 385–388, 2008.

[66] E. Y. Andrei, G. Li, and X. Du. Electronic properties of graphene: a perspective from scanning tunneling microscopy and magnetotransport. *Rep. Prog. Phys.*, 75(5): 056501, 2012.

[67] A. H. Castro Neto, F. Guinea, N. M. R. Peres, K. S. Novoselov, and A. K. Geim. The electronic properties of graphene. *Rev. Mod. Phys.*, 81: 109–162, 2009.

[68] A. K. Geim and K. S. Novoselov. The rise of graphene. *Nat. Mater.*, 6(3): 183–191, 2007.

[69] A. Politano, F. de Juan, G. Chiarello, and H. A. Fertig. Emergence of an Out-of-Plane Optical Phonon (ZO) Kohn Anomaly in Quasifreestanding Epitaxial Graphene. *Phys. Rev. Lett.*, 115: 075504, 2015.

[70] A. Allard and L. Wirtz. Graphene on Metallic Substrates: Suppression of the Kohn Anomalies in the Phonon Dispersion. *Nano Lett.*, 10(11): 4335–4340, 2010.

[71] M. Endlich, H. P. C. Miranda, A. Molina-Sánchez, L. Wirtz, and J. Kröger. Moiré-induced replica of graphene phonons on Ir(111). *Ann. Phys.*, 526(9-10): 372–380, 2014.

[72] A. Politano. Spectroscopic Investigations of Phonons in Epitaxial Graphene. *Crit. Rev. Solid State Mater. Sci.*, 42(2): 99–128, 2017.

[73] A. T. N Diaye, S. Bleikamp, P. J. Feibelman, and T. Michely. Two-Dimensional Ir Cluster Lattice on a Graphene Moiré on Ir(111). *Phys. Rev. Lett.*, 97: 215501, 2006.

[74] E. Loginova, S. Nie, K. Thürmer, N. C. Bartelt, and K. F. McCarty. Defects of graphene on Ir(111): Rotational domains and ridges. *Phys. Rev. B*, 80: 085430, 2009.

[75] M. Gao, Y. Pan, L. Huang, H. Hu, L. Z. Zhang, H. M. Guo, S. X. Du, and H.-J. Gao. Epitaxial growth and structural property of graphene on Pt(111). *Appl. Phys. Lett.*, 98(3): 033101, 2011.

[76] D. Martoccia, M. Björck, C. M. Schlepütz, T. Brugger, S. A. Pauli, B. D. Patterson, T. Greber, and P. R. Willmott. Graphene on Ru(0001): a corrugated and chiral structure. *New J. Phys.*, 12(4): 043028, 2010.

[77] G. Giovannetti, P. A. Khomyakov, G. Brocks, V. M. Karpan, J. van den Brink, and P. J. Kelly. Doping Graphene with Metal Contacts. *Phys. Rev. Lett.*, 101: 026803, 2008.

[78] P. Sutter, J. T. Sadowski, and E. Sutter. Graphene on Pt(111): Growth and substrate interaction. *Phys. Rev. B*, 80: 245411, 2009.

[79] I. Pletikosi , M. Kralj, P. Pervan, R. Brako, J. Coraux, A. T. N Diaye, C. Busse, and T. Michely. Dirac Cones and Minigaps for Graphene on Ir(111). *Phys. Rev. Lett.*, 102: 056808, 2009.

[80] A. L. Vázquez de Parga, F. Calleja, B. Borca, M. C. G. Passeggi, J. J. Hinarejos, F. Guinea, and R. Miranda. Periodically Rippled Graphene: Growth and Spatially Resolved Electronic Structure. *Phys. Rev. Lett.*, 100: 056807, 2008.

[81] J. S. Alden, A. W. Tsen, P. Y. Huang, R. Hovden, L. Brown, J. Park, D. A. Muller, and P. L. McEuen. Strain solitons and topological defects in bilayer graphene. *Proc. Natl. Acad. Sci. U.S.A.*, 110(28): 11256–11260, 2013.

[82] P. Pochet, B. C. McGuigan, J. Coraux, and H. Johnson. Toward Moiré engineering in 2D materials via dislocation theory. *Applied Materials Today*, 9: 240–250, 2017.

[83] A. T. N Diaye, J. Coraux, T. N. Plasa, C. Busse, and T. Michely. Structure of epitaxial graphene on Ir(111). *New J. Phys.*, 10(4): 043033, 2008.

[84] A. Artaud, L. Magaud, T. Le Quang, V. Guisset, P. David, C. Chapelier, and J. Coraux. Universal classification of twisted, strained and sheared graphene moiré superlattices. *Sci. Rep.*, 6: 25670, 2016.

[85] Y. Cui, Q. Fu, and X. Bao. Dynamic observation of layer-by-layer growth and removal of graphene on Ru(0001). *Phys. Chem. Chem. Phys.*, 12: 5053–5057, 2010.

[86] Y. Que, W. Xiao, X. Fei, H. Chen, L. Huang, S. X. Du, and H.-J. Gao. Epitaxial growth of large-area bilayer graphene on Ru(0001). *Appl. Phys. Lett.*, 104(9): 093110, 2014.

[87] G. Binnig, H. Rohrer, C. Gerber, and E. Weibel. Tunneling through a controllable vacuum gap. *Appl. Phys. Lett.*, 40(2): 178–180, 1982.

[88] G. Binnig, H. Rohrer, C. Gerber, and E. Weibel. Surface Studies by Scanning Tunneling Microscopy. *Phys. Rev. Lett.*, 49: 57–61, 1982.

[89] R. C. Jaklevic and J. Lambe. Molecular Vibration Spectra by Electron Tunneling. *Phys. Rev. Lett.*, 17: 1139–1140, 1966.

[90] A. Deshpande, W. Bao, F. Miao, C. N. Lau, and B. J. LeRoy. Spatially resolved spectroscopy of monolayer graphene on SiO_2. *Phys. Rev. B*, 79: 205411, 2009.

[91] S. Jung, G. M. Rutter, N. N. Klimov, D. B. Newell, I. Calizo, A. R. Walker, N. B. Zhitenev, and J. A. Stroscio. Evolution of microscopic localization in graphene in a magnetic field from scattering resonances to quantum dots. *Nat. Phys.*, 7: 245–251, 2011.

[92] J. Halle, N. Néel, and J. Kröger. Filling the Gap: Li-Intercalated Graphene on Ir(111). *J. Phys. Chem. C*, 120(9): 5067–5073, 2016.

[93] N. Papior, N. Lorente, T. Frederiksen, A. García, and M. Brandbyge. Improvements on non-equilibrium and transport Green function techniques: The next-generation TRANSIESTA. *Comput. Phys. Commun.*, 212: 8–24, 2017.

[94] V. Popescu and A. Zunger. Effective band structure of random alloys. *Phys. Rev. Lett.*, 104(23): 236403, 2010.

[95] N. R. Papior, G. Calogero, and M. Brandbyge. Simple and efficient LCAO basis sets for the diffuse states in carbon nanostructures. *J. Phys.: Condens. Matter*, 30(25): 25LT01, 2018.

[96] J.-T. Lü, R. B. Christensen, G. Foti, T. Frederiksen, T. Gunst, and M. Brandbyge. Efficient calculation of inelastic vibration signals in electron transport: Beyond the wide-band approximation. *Phys. Rev. B*, 89: 081405, 2014.

[97] M. Paulsson, T. Frederiksen, and M. Brandbyge. Inelastic Transport through Molecules: Comparing First-Principles Calculations to Experiments. *Nano Lett.*, 6(2): 258–262, 2006.

[98] M. Andersen, L. Hornekær, and B. Hammer. Understanding intercalation structures formed under graphene on Ir(111). *Phys. Rev. B*, 90: 155428, 2014.

[99] M. L. N. Palsgaard, N. P. Andersen, and M. Brandbyge. Unravelling the role of inelastic tunneling into pristine and defected graphene. *Phys. Rev. B*, 91(12): 121403, 2015.

[100] J. Kröger, N. Néel, and L. Limot. Contact to single atoms and molecules with the tip of a scanning tunnelling microscope. *J. Phys.: Condens. Matter*, 20 (22): 223001, 2008.

[101] R. Berndt, J. Kröger, N. Néel, and G. Schull. Controlled single atom and single molecule contacts. *Phys. Chem. Chem. Phys.*, 12: 1022–1032, 2010.

[102] S. J. Altenburg, J. Kröger, B. Wang, M.-L. Bocquet, N. Lorente, and R. Berndt. Graphene on Ru(0001): Contact Formation and Chemical Reactivity on the Atomic Scale. *Phys. Rev. Lett.*, 105: 236101, 2010.

[103] S. J. Altenburg and R. Berndt. Local work function and STM tip-induced distortion of graphene on Ir(111). *New J. Phys.*, 16(5): 053036, 2014.

[104] S. Zhu, Y. Huang, N. N. Klimov, D. B. Newell, N. B. Zhitenev, J. A. Stroscio, S. D. Solares, and T. Li. Pseudomagnetic fields in a locally strained graphene drumhead. *Phys. Rev. B*, 90: 075426, 2014.

[105] J. Lagoute, F. Joucken, V. Repain, Y. Tison, C. Chacon, A. Bellec, Y. Girard, R. Sporken, E. H. Conrad, F. m. c. Ducastelle, M. Palsgaard, N. P. Andersen, M. Brandbyge, and S. Rousset. Giant tunnel-electron injection in nitrogen-doped graphene. *Phys. Rev. B*, 91: 125442, 2015.

[106] J. Hass, F. Varchon, J. E. Millán-Otoya, M. Sprinkle, N. Sharma, W. A. de Heer, C. Berger, P. N. First, L. Magaud, and E. H. Conrad. Why Multilayer Graphene on $4H-$SiC$(000\bar{1})$ Behaves Like a Single Sheet of Graphene. *Phys. Rev. Lett.*, 100: 125504, 2008.

[107] K. S. Novoselov, E. McCann, S. V. Morozov, V. I. Fal ko, M. I. Katsnelson, U. Zeitler, D. Jiang, F. Schedin, and A. K. Geim. Unconventional quantum

Hall effect and Berry s phase of 2π in bilayer graphene. *Nat. Phys.*, 2: 177–180, 2006.

[108] E. McCann and V. I. Fal ko. Landau-Level Degeneracy and Quantum Hall Effect in a Graphite Bilayer. *Phys. Rev. Lett.*, 96: 086805, 2006.

[109] K. S. Kim, A. L. Walter, L. Moreschini, T. Seyller, K. Horn, E. Rotenberg, and A. Bostwick. Coexisting massive and massless Dirac fermions in symmetry-broken bilayer graphene. *Nat. Mater.*, 12(10): 887, 2013.

[110] G. Li, A. Luican, J. L. Dos Santos, A. C. Neto, A. Reina, J. Kong, and E. Andrei. Observation of Van Hove singularities in twisted graphene layers. *Nat. Phys.*, 6(2): 109, 2010.

[111] I. Brihuega, P. Mallet, H. González-Herrero, G. Trambly de Laissardière, M. M. Ugeda, L. Magaud, J. M. Gómez-Rodríguez, F. Ynduráin, and J.-Y. Veuillen. Unraveling the Intrinsic and Robust Nature of van Hove Singularities in Twisted Bilayer Graphene by Scanning Tunneling Microscopy and Theoretical Analysis. *Phys. Rev. Lett.*, 109: 196802, 2012.

[112] R. Bistritzer and A. H. MacDonald. Moiré bands in twisted double-layer graphene. *Proc. Natl. Acad. Sci. U.S.A.*, 108(30): 12233–12237, 2011.

[113] D. Wong, Y. Wang, J. Jung, S. Pezzini, A. M. DaSilva, H.-Z. Tsai, H. S. Jung, R. Khajeh, Y. Kim, J. Lee, S. Kahn, S. Tollabimazraehno, H. Rasool, K. Watanabe, T. Taniguchi, A. Zettl, S. Adam, A. H. MacDonald, and M. F. Crommie. Local spectroscopy of moiré-induced electronic structure in gate-tunable twisted bilayer graphene. *Phys. Rev. B*, 92: 155409, 2015.

[114] P. W. Sutter, J.-I. Flege, and E. A. Sutter. Epitaxial graphene on ruthenium. *Nat. Mater.*, 7(5): 406, 2008.

[115] K. F. McCarty, P. J. Feibelman, E. Loginova, and N. C. Bartelt. Kinetics and thermodynamics of carbon segregation and graphene growth on Ru(0001). *Carbon*, 47(7): 1806–1813, 2009.

[116] N. Liu, L. Fu, B. Dai, K. Yan, X. Liu, R. Zhao, Y. Zhang, and Z. Liu. Universal segregation growth approach to wafer-size graphene from non-noble metals. *Nano Lett.*, 11(1): 297–303, 2010.

[117] S. Marchini, S. Günther, and J. Wintterlin. Scanning tunneling microscopy of graphene on Ru(0001). *Phys. Rev. B*, 76: 075429, 2007.

[118] E. Sutter, D. P. Acharya, J. T. Sadowski, and P. Sutter. Scanning tunneling microscopy on epitaxial bilayer graphene on ruthenium (0001). *Appl. Phys. Lett.*, 94(13): 133101, 2009.

[119] M. Papagno, D. Pacilé, D. Topwal, P. Moras, P. M. Sheverdyaeva, F. D. Natterer, A. Lehnert, S. Rusponi, Q. Dubout, F. Calleja, E. Frantzeskakis, S. Pons, J. Fujii, I. Vobornik, M. Grioni, C. Carbone, and H. Brune. Two Distinct Phases of Bilayer Graphene Films on Ru(0001). *ACS Nano*, 6(10): 9299–9304, 2012.

[120] Q. Dubout, F. Calleja, G. Sclauzero, M. Etzkorn, A. Lehnert, L. Claude, M. Papagno, F. D. Natterer, F. Patthey, S. Rusponi, A. Pasquarello, and H. Brune. Giant apparent lattice distortions in STM images of corrugated sp^2-hybridised monolayers. *New J. Phys.*, 18: 103027, 2016.

[121] B. Wang and M.-L. Bocquet. Interfacial coupling in rotational monolayer and bilayer graphene on Ru(0001) from first principles. *Nanoscale*, 4: 4687–4693, 2012.

[122] W. Moritz, B. Wang, M.-L. Bocquet, T. Brugger, T. Greber, J. Wintterlin, and S. Günther. Structure Determination of the Coincidence Phase of Graphene on Ru(0001). *Phys. Rev. Lett.*, 104: 136102, 2010.

[123] J. Lu, A. C. Neto, and K. P. Loh. Transforming moiré blisters into geometric graphene nano-bubbles. *Nat. Commun.*, 3: 823, 2012.

[124] F. Jiménez-Villacorta, L. Álvarez-Fraga, J. Bartolomé, E. Climent-Pascual, E. Salas-Colera, M. X. Aguilar-Pujol, R. Ramírez-Jiménez, A. Cremades, C. Prieto, and A. de Andrés. Nanocrystalline cubic ruthenium carbide formation in the synthesis of graphene on ruthenium ultrathin films. *J. Mater. Chem. C*, 5(39): 10260–10269, 2017.

[125] L. Vitali, M. A. Schneider, K. Kern, L. Wirtz, and A. Rubio. Phonon and plasmon excitation in inelastic electron tunneling spectroscopy of graphite. *Phys. Rev. B*, 69: 121414, 2004.

[126] J. Geiger, H. Katterwe, and B. Schröder. Elektronenenergieverlustspektren von Graphiteinkristallen und Kohlenstoffaufdampfschichten im Bereich 0,02-0,4 eV. *Z. Phys. A*, 241(1): 45–54, 1971.

[127] E. T. Jensen, R. E. Palmer, W. Allison, and J. Annett. Temperature-dependent plasmon frequency and linewidth in a semimetal. *Phys. Rev. Lett.*, 66: 492–495, 1991.

[128] E. McCann and M. Koshino. The electronic properties of bilayer graphene. *Rep. Prog. Phys.*, 76(5): 056503, 2013.

[129] D. V. Badami. X-Ray studies of graphite formed by decomposing silicon carbide. *Carbon*, 3(1): 53–57, 1965.

[130] A. Van Bommel, J. Crombeen, and A. Van Tooren. LEED and Auger electron observations of the SiC (0001) surface. *Surf. Sci.*, 48(2): 463–472, 1975.

[131] C. Riedl, C. Coletti, and U. Starke. Structural and electronic properties of epitaxial graphene on SiC (0 0 0 1): a review of growth, characterization, transfer doping and hydrogen intercalation. *J. Phys. D: Appl. Phys.*, 43(37): 374009, 2010.

[132] C. Oshima and A. Nagashima. Ultra-thin epitaxial films of graphite and hexagonal boron nitride on solid surfaces. *J. Phys.: Condens. Matter*, 9(1): 1, 1997.

[133] J. Coraux, A. T. N Diaye, M. Engler, C. Busse, D. Wall, N. Buckanie, F.-J. M. zu Heringdorf, R. van Gastel, B. Poelsema, and T. Michely. Growth of graphene on Ir(111). *New J. Phys.*, 11(2): 023006, 2009.

[134] J. Coraux, A. T. N Diaye, C. Busse, and T. Michely. Structural Coherency of Graphene on Ir(111). *Nano Lett.*, 8(2): 565–570, 2008.

[135] H. Hattab, A. T. N Diaye, D. Wall, G. Jnawali, J. Coraux, C. Busse, R. van Gastel, B. Poelsema, T. Michely, F.-J. M. zu Heringdorf, and M. H. von Hoegen. Growth temperature dependent graphene alignment on Ir(111). *Appl. Phys. Lett.*, 98(14): 141903, 2011.

[136] A. Reina, X. Jia, J. Ho, D. Nezich, H. Son, V. Bulovic, M. S. Dresselhaus, and J. Kong. Large Area, Few-Layer Graphene Films on Arbitrary Substrates by Chemical Vapor Deposition. *Nano Lett.*, 9(1): 30–35, 2009.

[137] J.-H. Gao, D. Fujita, M.-S. Xu, K. Onishi, and S. Miyamoto. Unique Synthesis of Few-Layer Graphene Films on Carbon-Doped Pt83Rh17 Surfaces. *ACS Nano*, 4(2): 1026–1032, 2010.

[138] M. Xu, D. Fujita, K. Sagisaka, E. Watanabe, and N. Hanagata. Production of Extended Single-Layer Graphene. *ACS Nano*, 5(2): 1522–1528, 2011.

[139] E. Zhizhin, D. Pudikov, A. Rybkin, A. Petukhov, Y. Zhukov, and A. Shikin. Growth of graphene monolayer by "internal solid-state carbon source": Electronic structure, morphology and Au intercalation. *Mater. Des.*, 104: 284–291, 2016.

[140] D. Pudikov, E. Zhizhin, A. Rybkin, and A. Shikin. Graphene fabrication via carbon segregation through transition metal films. *Thin Solid Films*, 648: 120–127, 2018.

[141] S. Nie, A. L. Walter, N. C. Bartelt, E. Starodub, A. Bostwick, E. Rotenberg, and K. F. McCarty. Growth from Below: Graphene Bilayers on Ir(111). *ACS Nano*, 5(3): 2298–2306, 2011.

[142] C. Herbig, T. Knispel, S. Simon, U. A. Schröder, A. J. Martínez-Galera, M. A. Arman, C. Teichert, J. Knudsen, A. V. Krasheninnikov, and T. Michely. From Permeation to Cluster Arrays: Graphene on Ir(111) Exposed to Carbon Vapor. *Nano Lett.*, 17(5): 3105–3112, 2017.

[143] P. Leicht, L. Zielke, S. Bouvron, R. Moroni, E. Voloshina, L. Hammerschmidt, Y. S. Dedkov, and M. Fonin. In Situ Fabrication Of Quasi-Free-Standing Epitaxial Graphene Nanoflakes On Gold. *ACS Nano*, 8(4): 3735–3742, 2014.

[144] Z. Liang, H. Khosravian, A. Uhl, R. J. Meyer, and M. Trenary. Graphene domain boundaries on Pt(111) as nucleation sites for Pt nanocluster formation. *Surf. Sci.*, 606(21): 1643–1648, 2012.

[145] X. Feng, S. Maier, and M. Salmeron. Water Splits Epitaxial Graphene and Intercalates. *J. Am. Chem. Soc.*, 134(12): 5662–5668, 2012.

[146] X. Hu, T. Björkman, H. Lipsanen, L. Sun, and A. V. Krasheninnikov. Solubility of Boron, Carbon, and Nitrogen in Transition Metals: Getting Insight into Trends from First-Principles Calculations. *J. Phys. Chem. Lett.*, 6(16): 3263–3268, 2015.

[147] G. Otero, C. González, A. L. Pinardi, P. Merino, S. Gardonio, S. Lizzit, M. Blanco-Rey, K. Van de Ruit, C. F. J. Flipse, J. Méndez, P. L. de Andrés, and J. A. Martín-Gago. Ordered Vacancy Network Induced by the Growth of Epitaxial Graphene on Pt(111). *Phys. Rev. Lett.*, 105: 216102, 2010.

[148] A. Luican, G. Li, A. Reina, J. Kong, R. R. Nair, K. S. Novoselov, A. K. Geim, and E. Y. Andrei. Single-Layer Behavior and Its Breakdown in Twisted Graphene Layers. *Phys. Rev. Lett.*, 106: 126802, 2011.

[149] E. Starodub, A. Bostwick, L. Moreschini, S. Nie, F. E. Gabaly, K. F. McCarty, and E. Rotenberg. In-plane orientation effects on the electronic structure, stability, and Raman scattering of monolayer graphene on Ir(111). *Phys. Rev. B*, 83: 125428, 2011.

[150] J. V. Barth, G. Costantini, and K. Kern. Engineering atomic and molecular nanostructures at surfaces. *Nature*, 437: 671–679, 2005.

[151] J. V. Barth. Molecular Architectonic on Metal Surfaces. *Annu. Rev. Phys. Chem.*, 58(1): 375–407, 2007.

[152] Y. Wang, K. Wu, J. Kröger, and R. Berndt. Review Article: Structures of phthalocyanine molecules on surfaces studied by STM. *AIP Adv.*, 2(4): 041402, 2012.

[153] J. A. Theobald, N. S. Oxtoby, M. A. Phillips, N. R. Champness, and P. H. Beton. Controlling molecular deposition and layer structure with supramolecular surface assemblies. *Nature*, 424: 1029–1031, 2003.

[154] M. Corso, W. Auwärter, M. Muntwiler, A. Tamai, T. Greber, and J. Osterwalder. Boron Nitride Nanomesh. *Science*, 303(5655): 217–220, 2004.

[155] H. Dil, J. Lobo-Checa, R. Laskowski, P. Blaha, S. Berner, J. Osterwalder, and T. Greber. Surface Trapping of Atoms and Molecules with Dipole Rings. *Science*, 319(5871): 1824–1826, 2008.

[156] S. Berner, M. Corso, R. Widmer, O. Groening, R. Laskowski, P. Blaha, K. Schwarz, A. Goriachko, H. Over, S. Gsell, M. Schreck, H. Sachdev, T. Greber, and J. Osterwalder. Boron Nitride Nanomesh: Functionality from a Corrugated Monolayer. *Angew. Chem. Int. Ed.*, 46(27): 5115–5119, 2007.

[157] A. Goriachko, He, M. Knapp, H. Over, M. Corso, T. Brugger, S. Berner, J. Osterwalder, and T. Greber. Self-Assembly of a Hexagonal Boron Nitride Nanomesh on Ru(0001). *Langmuir*, 23(6): 2928–2931, 2007.

[158] A. Goriachko, Y. B. He, and H. Over. Complex Growth of NanoAu on BN Nanomeshes Supported by Ru(0001). *J. Phys. Chem. C*, 112(22): 8147–8152, 2008.

[159] P. Järvinen, S. K. Hämäläinen, M. Ijäs, A. Harju, and P. Liljeroth. Self-Assembly and Orbital Imaging of Metal Phthalocyanines on a Graphene Model Surface. *J. Phys. Chem. C*, 118(24): 13320–13325, 2014.

[160] J. Mao, H. Zhang, Y. Jiang, Y. Pan, M. Gao, W. Xiao, and H.-J. Gao. Tunability of Supramolecular Kagome Lattices of Magnetic Phthalocyanines Using Graphene-Based Moiré Patterns as Templates. *J. Am. Chem. Soc.*, 131(40): 14136–14137, 2009.

[161] A. T. N Diaye, T. Gerber, C. Busse, J. Myslive ek, J. Coraux, and T. Michely. A versatile fabrication method for cluster superlattices. *New J. Phys.*, 11(10): 103045, 2009.

[162] Y. Pan, M. Gao, L. Huang, F. Liu, and H.-J. Gao. Directed self-assembly of monodispersed platinum nanoclusters on graphene Moiré template. *Appl. Phys. Lett.*, 95(9): 093106, 2009.

[163] K. Donner and P. Jakob. Structural properties and site specific interactions of Pt with the graphene/Ru(0001) moiré overlayer. *J. Chem. Phys.*, 131(16): 164701, 2009.

[164] A. Cavallin, M. Pozzo, C. Africh, A. Baraldi, E. Vesselli, C. Dri, G. Comelli, R. Larciprete, P. Lacovig, S. Lizzit, and D. Alfè. Local Electronic Structure and Density of Edge and Facet Atoms at Rh Nanoclusters Self-Assembled on a Graphene Template. *ACS Nano*, 6(4): 3034–3043, 2012.

[165] M. Sicot, S. Bouvron, O. Zander, U. Rüdiger, Y. S. Dedkov, and M. Fonin. Nucleation and growth of nickel nanoclusters on graphene Moiré on Rh(111). *Appl. Phys. Lett.*, 96(9): 093115, 2010.

[166] A. Pollard, E. Perkins, N. Smith, A. Saywell, G. Goretzki, A. Phillips, S. Argent, H. Sachdev, F. Müller, S. Hüfner, S. Gsell, M. Fischer, M. Schreck, J. Osterwalder, T. Greber, S. Berner, N. Champness, and P. Beton. Supramolecular

Assemblies Formed on an Epitaxial Graphene Superstructure. *Angew. Chem. Int. Ed.*, 49(10): 1794–1799, 2010.

[167] E. Sutter, P. Albrecht, B. Wang, M.-L. Bocquet, L. Wu, Y. Zhu, and P. Sutter. Arrays of Ru nanoclusters with narrow size distribution templated by monolayer graphene on Ru. *Surf. Sci.*, 605(17): 1676–1684, 2011.

[168] M. Roos, D. Künzel, B. Uhl, H.-H. Huang, O. Brandao Alves, H. E. Hoster, A. Gross, and R. J. Behm. Hierarchical Interactions and Their Influence upon the Adsorption of Organic Molecules on a Graphene Film. *J. Am. Chem. Soc.*, 133(24): 9208–9211, 2011.

[169] J. Lu, P. S. E. Yeo, Y. Zheng, Z. Yang, Q. Bao, C. K. Gan, and K. P. Loh. Using the Graphene Moiré Pattern for the Trapping of C60 and Homoepitaxy of Graphene. *ACS Nano*, 6(1): 944–950, 2012.

[170] M. Bazarnik, J. Brede, R. Decker, and R. Wiesendanger. Tailoring Molecular Self-Assembly of Magnetic Phthalocyanine Molecules on Fe- and Co-Intercalated Graphene. *ACS Nano*, 7(12): 11341–11349, 2013.

[171] F. Schulz, R. Drost, S. K. Hämäläinen, and P. Liljeroth. Templated Self-Assembly and Local Doping of Molecules on Epitaxial Hexagonal Boron Nitride. *ACS Nano*, 7(12): 11121–11128, 2013.

[172] P. Järvinen, S. K. Hämäläinen, K. Banerjee, P. Häkkinen, M. Ijäs, A. Harju, and P. Liljeroth. Molecular Self-Assembly on Graphene on SiO2 and h-BN Substrates. *Nano Lett.*, 13(7): 3199–3204, 2013.

[173] K. Banerjee, A. Kumar, F. F. Canova, S. Kezilebieke, A. S. Foster, and P. Liljeroth. Flexible Self-Assembled Molecular Templates on Graphene. *J. Phys. Chem. C*, 120(16): 8772–8780, 2016.

[174] R. Baltic, M. Pivetta, F. Donati, C. Wäckerlin, A. Singha, J. Dreiser, S. Rusponi, and H. Brune. Superlattice of Single Atom Magnets on Graphene. *Nano Lett.*, 16(12): 7610–7615, 2016.

[175] M. Pivetta, S. Rusponi, and H. Brune. Direct capture and electrostatic repulsion in the self-assembly of rare-earth atom superlattices on graphene. *Phys. Rev. B*, 98: 115417, 2018.

[176] A. R. Sandy, S. G. J. Mochrie, D. M. Zehner, G. Grübel, K. G. Huang, and D. Gibbs. Reconstruction of the Pt(111) surface. *Phys. Rev. Lett.*, 68: 2192–2195, 1992.

[177] G. Grübel, K. G. Huang, D. Gibbs, D. M. Zehner, A. R. Sandy, and S. G. J. Mochrie. Reconstruction of the Pt(111) surface: X-ray-scattering measurements. *Phys. Rev. B*, 48: 18119–18139, 1993.

[178] M. Bott, M. Hohage, T. Michely, and G. Comsa. Pt(111) reconstruction induced by enhanced Pt gas-phase chemical potential. *Phys. Rev. Lett.*, 70: 1489–1492, 1993.

[179] M. Hohage, T. Michely, and G. Comsa. Pt(111) network reconstruction: structure, growth and decay. *Surf. Sci.*, 337(3): 249–267, 1995.

[180] U. Harten, A. M. Lahee, J. P. Toennies, and C. Wöll. Observation of a Soliton Reconstruction of Au(111) by High-Resolution Helium-Atom Diffraction. *Phys. Rev. Lett.*, 54: 2619–2622, 1985.

[181] C. Wöll, S. Chiang, R. J. Wilson, and P. H. Lippel. Determination of atom positions at stacking-fault dislocations on Au(111) by scanning tunneling microscopy. *Phys. Rev. B*, 39: 7988–7991, 1989.

[182] J. V. Barth, H. Brune, G. Ertl, and R. J. Behm. Scanning tunneling microscopy observations on the reconstructed Au(111) surface: Atomic structure, long-range superstructure, rotational domains, and surface defects. *Phys. Rev. B*, 42: 9307–9318, 1990.

[183] S. Narasimhan and D. Vanderbilt. Elastic stress domains and the herringbone reconstruction on Au(111). *Phys. Rev. Lett.*, 69: 1564–1567, 1992.

[184] P. Grütter and U. Dürig. Quasidendritic growth of Co induced by localized reconstruction of Pt(111). *Surf. Sci.*, 337(1): 147–152, 1995.

[185] L. Zhang, J. van Ek, and U. Diebold. Highly ordered nanoscale surface alloy formed through Cr-induced Pt(111) reconstruction. *Phys. Rev. B*, 57: R4285–R4288, 1998.

[186] B. Holst, M. Nohlen, K. Wandelt, and W. Allison. Observation of an adlayer-driven substrate reconstruction in Cu-Pt(111). *Phys. Rev. B*, 58: R10195–R10198, 1998.

[187] R. Pushpa and S. Narasimhan. Reconstruction of Pt(111) and domain patterns on close-packed metal surfaces. *Phys. Rev. B*, 67: 205418, 2003.

[188] T. Kontorova and J. Frenkel. On the theory of plastic deformation and twinning. II. *Zh. Eksp. Teor. Fiz.*, 8: 1340–1348, 1938.

[189] E. Starodub, S. Maier, I. Stass, N. C. Bartelt, P. J. Feibelman, M. Salmeron, and K. F. McCarty. Graphene growth by metal etching on Ru(0001). *Phys. Rev. B*, 80: 235422, 2009.

[190] H. P. Bonzel, A. M. Bradshaw, and G. Ertl, editors. *Physics and chemistry of alkali metal adsorption.* Elsevier, 1989.

[191] R. D. Diehl and R. McGrath. Structural studies of alkali metal adsorption and coadsorption on metal surfaces. *Surf. Sci. Rep.*, 23(2): 43–171, 1996.

[192] R. D. Diehl and R. McGrath. Current progress in understanding alkali metal adsorption on metal surfaces. *J. Phys.: Condens. Matter*, 9(5): 951–968, 1997.

[193] S. A. Lindgren, L. Walldén, J. Rundgren, P. Westrin, and J. Neve. Structure of Cu(111)$p(2 \times 2)$Cs determined by low-energy electron diffraction. *Phys. Rev. B*, 28: 6707–6712, 1983.

[194] D. Doering and S. Semancik. Chemisorption and rotational epitaxy of lithium on Ru(001). *Surf. Sci. Lett.*, 175(2): L730–L736, 1986.

[195] H. Over, H. Bludau, M. Skottke-Klein, G. Ertl, W. Moritz, and C. T. Campbell. Coverage dependence of adsorption-site geometry in the Cs/Ru(0001) system: A low-energy electron-diffraction analysis. *Phys. Rev. B*, 45: 8638–8649, 1992.

[196] G. S. Leatherman and R. D. Diehl. Phase diagrams and rotated incommensurate phases of K, Rb, and Cs adsorbed on Ag(111). *Phys. Rev. B*, 53: 4939–4946, 1996.

[197] M. Gierer, H. Over, H. Bludau, and G. Ertl. Structural properties of ordered alkali metal overlayers: a LEED analysis of the Ru(0001)-$(\sqrt{3} \times \sqrt{3})$R30°-Li phase in comparison with related systems. *Surf. Sci.*, 337(3): 198–204, 1995.

[198] T. von Hofe, J. Kröger, and R. Berndt. Adsorption geometry of Cu(111)$-$Cs studied by scanning tunneling microscopy. *Phys. Rev. B*, 73: 245434, 2006.

[199] M. Ziegler, J. Kröger, R. Berndt, A. Filinov, and M. Bonitz. Scanning tunneling microscopy and kinetic Monte Carlo investigation of cesium superlattices on Ag(111). *Phys. Rev. B*, 78: 245427, 2008.

[200] P. He and K. Jacobi. Vibrational analysis of cesium on Ru(0001). *Phys. Rev. B*, 53: 3658–3661, 1996.

[201] G. G. Rusina, S. V. Eremeev, P. M. Echenique, G. Benedek, S. D. Borisova, and E. V. Chulkov. Vibrations of alkali metal overlayers on metal surfaces. *J. Phys.: Condens. Matter*, 20(22): 224007, 2008.

[202] J. Kröger, D. Bruchmann, S. Lehwald, and H. Ibach. Adsorption of lithium on Mo(110): an EELS study of the adsorbate vibrations and substrate phonons. *Surf. Sci.*, 449(1): 227–235, 2000.

[203] J. Kröger, S. Lehwald, and H. Ibach. Surface dynamics of Mo(110)-H and Mo(110)-Li. *Surf. Sci.*, 530(3): 170–174, 2003.

[204] M. Bauer, S. Pawlik, and M. Aeschlimann. Resonance lifetime and energy of an excited Cs state on Cu(111). *Phys. Rev. B*, 55: 10040–10043, 1997.

[205] S. Ogawa, H. Nagano, and H. Petek. Phase and Energy Relaxation in an Antibonding Surface State: Cs/Cu(111). *Phys. Rev. Lett.*, 82: 1931–1934, 1999.

[206] A. G. Borisov, J. P. Gauyacq, A. K. Kazansky, E. V. Chulkov, V. M. Silkin, and P. M. Echenique. Long-Lived Excited States at Surfaces: Cs/Cu(111) and Cs/Cu(100) Systems. *Phys. Rev. Lett.*, 86: 488–491, 2001.

[207] J. Gauyacq, A. Borisov, and A. Kazansky. Impurity-induced localisation of the 2D surface-state continuum on a metal surface. *Appl. Phys. A*, 78(2): 141–147, 2004.

[208] C. Corriol, V. M. Silkin, D. Sánchez-Portal, A. Arnau, E. V. Chulkov, P. M. Echenique, T. von Hofe, J. Kliewer, J. Kröger, and R. Berndt. Role of Elastic Scattering in Electron Dynamics at Ordered Alkali Overlayers on Cu(111). *Phys. Rev. Lett.*, 95: 176802, 2005.

[209] J. Kröger, M. Becker, H. Jensen, T. von Hofe, N. Néel, L. Limot, R. Berndt, S. Crampin, E. Pehlke, C. Corriol, V. Silkin, D. Sánchez-Portal, A. Arnau,

E. Chulkov, and P. Echenique. Dynamics of surface-localised electronic excitations studied with the scanning tunnelling microscope. *Prog. Surf. Sci.*, 82(4): 293–312, 2007.

[210] M. Ziegler, J. Kröger, R. Berndt, A. G. Borisov, and J. P. Gauyacq. Linewidth of a cesium adatom resonance on Ag(111). *Phys. Rev. B*, 79: 075401, 2009.

[211] M. Papagno, S. Rusponi, P. M. Sheverdyaeva, S. Vlaic, M. Etzkorn, D. Pacilé, P. Moras, C. Carbone, and H. Brune. Large Band Gap Opening between Graphene Dirac Cones Induced by Na Adsorption onto an Ir Superlattice. *ACS Nano*, 6: 199, 2012.

[212] P. Matyba, A. Carr, C. Chen, D. L. Miller, G. Peng, S. Mathias, M. Mavrikakis, D. S. Dessa, M. W. Keller, H. C. Kapteyn, and M. Murnane. Controlling the electronic structure of graphene using surface-adsorbate interactions. *Phys. Rev. B: Condens. Matter Mater. Phys.*, 92: 041407, 2015.

[213] J.-H. Chen, C. Jang, S. Adam, M. S. Fuhrer, E. D. Williams, and M. Ishigami. Charged-impurity scattering in graphene. *Nat. Phys.*, 4: 377, 2008.

[214] S. Woo, S. Hemmatiyan, T. D. Morrison, K. D. D. Rathnayaka, I. F. Lyuksyutov, and D. G. Naugle. Temperature-dependent transport properties of graphene decorated by alkali metal adatoms (Li, K). *Appl. Phys. Lett.*, 111: 263502, 2017.

[215] D. P. DiVincenzo and E. J. Mele. Cohesion and structure in stage-1 graphite intercalation compounds. *Phys. Rev. B*, 32: 2538–2553, 1985.

[216] C. Uthaisar and V. Barone. Edge Effects on the Characteristics of Li Diffusion in Graphene. *Nano Lett.*, 10(8): 2838–2842, 2010.

[217] C. Virojanadara, A. A. Zakharov, S. Watcharinyanon, R. Yakimova, and L. I. Johansson. A low-energy electron microscopy and x-ray photo-emission electron microscopy study of Li intercalated into graphene on SiC (0001). *New J. Phys.*, 12(12): 125015, 2010.

[218] G. Li, H. Zhou, L. Pan, Y. Zhang, L. Huang, W. Xu, S. Du, M. Ouyang, A. C. Ferrari, and H.-J. Gao. Role of Cooperative Interactions in the Intercalation of Heteroatoms between Graphene and a Metal Substrate. *J. Am. Chem. Soc.*, 137(22): 7099–7103, 2015.

[219] P. Pervan, P. Lazi , M. Petrovi , I. ' rut Raki , I. Pletikosi , M. Kralj, M. Milun, and T. Valla. Li adsorption versus graphene intercalation on Ir(111): From quenching to restoration of the Ir surface state. *Phys. Rev. B*, 92: 245415, 2015.

[220] M. Gierer, H. Over, H. Bludau, and G. Ertl. Incommensurate structures and epitaxial growth of Li on Ru(0001): A quantitative low-energy electron-diffraction study. *Phys. Rev. B*, 52: 2927–2934, 1995.

[221] J. Klime , D. R. Bowler, and A. Michaelides. Chemical accuracy for the van der Waals density functional. *J. Phys.: Condens. Matter*, 22(2): 022201, 2010.

[222] G. Kresse and J. Furthmüller. Efficiency of ab-initio total energy calculations for metals and semiconductors using a plane-wave basis set. *Comput. Mater. Sci.*, 6(1): 15–50, 1996.

[223] J. M. Soler, E. Artacho, J. D. Gale, A. García, J. Junquera, P. Ordejón, and D. Sánchez-Portal. The SIESTA method for ab initio order-N materials simulation. *J. Phys.: Condens. Matter*, 14(11): 2745–2779, 2002.

[224] M. Brandbyge, J.-L. Mozos, P. Ordejón, J. Taylor, and K. Stokbro. Density-functional method for nonequilibrium electron transport. *Phys. Rev. B*, 65: 165401, 2002.

[225] T. Frederiksen, M. Paulsson, M. Brandbyge, and A.-P. Jauho. Inelastic transport theory from first principles: Methodology and application to nanoscale devices. *Phys. Rev. B*, 75(20): 205413, 2007.

[226] J. P. Perdew, K. Burke, and M. Ernzerhof. Generalized Gradient Approximation Made Simple. *Phys. Rev. Lett.*, 77: 3865–3868, 1996.

Danksagung

Abschließend möchte ich mich gern bei allen bedanken, die mich während der Arbeit an dieser Dissertation unterstützt und begleitet haben. Besonderer Dank gilt meinem Betreuer Prof. Dr. Jörg Kröger für das Angebot der Promotionsstelle und das damit verbundene Vertrauen in mich. Sein Rat und seine Anleitung waren fundamentale Stützen meiner Arbeit und Weiterentwicklung.

Prof. Dr. Mads Brandbyge danke ich für die Bereitstellung der Transportrechnungen zu interkaliertem Graphen, die der Interpretation der experimentellen Daten zusätzliches Gewicht verliehen. Daneben danke ich auch Prof. Dr. Stefan Krischok für seine Bereitschaft, als weiterer Gutachter diese Dissertation zu beurteilen.

Überdies möchte ich mich bei der gesamten Arbeitsgruppe Experimentalphysik I für die angenehme Arbeitsatmosphäre bedanken. Besonderers hervorzuheben ist Dr. Nicolas Néel, der mir stets in allen das STM betreffenden Fragen mit Rat und Tat zur Seite stand. Die ehemaligen und aktuellen Mitdoktoranden der Arbeitsgruppe, Stefan Meierott, Martin Müller, Jonathan Brand und Alexander Mehler, sowie alle weiteren nicht namentlich erwähnten Mitglieder trugen mit gegenseitigen Tipps, konstruktiver Kritik, fachlichen Diskussionen und auch dem Zusammenhalt abseits der Arbeit wesentlich zum Gelingen dieser Dissertation bei.

Nicht unerwähnt lassen möchte ich unsere Sekretärin Jana Spindler, die stets einen reibungslosen Ablauf der Tagesgeschäfte gewährleistete und uns allen so manche bürokratische Last abnahm. Danke auch der Fakultätswerkstatt, insbesondere Werkstattleiter Herrn Mämpel, für die schnelle und zuverlässige Umsetzung und Anpassung aller angefragten Konstruktionen.

Meinen Eltern, Geschwistern, Freunden und meiner Lebensgefährtin Nadine danke ich für den bedingungslosen Rückhalt und die Unterstüzung weit über diese Promotion hinaus.

Vielen herzlichen Dank!